PAPR Reduction in Multicarrier Modulation Techniques Based Visible Light Communication Systems

Hussien Theeb Alrakah

Dedication

This thesis is dedicated to the memory of my father "Theeb ibin Daham Alrakah".

Lay Summary

The high demand for wireless data access is growing exponentially which is partially due to the increasing number of internet users, and newly emerging technologies and services such as internet of things (IoT), machine to machine (M2M) connectivity, augmented and virtual reality (AR/VR), smart televisions and cloud services. In addition, the radio frequency (RF) based communication has a limited resources and cannot accommodate the endless bandwidth demand. Therefore, visible light spectrum offers alternative free and large spectrum that is can be used. Visible light commutation (VLC) uses low-cost commercially available off-the-shelf front-end devices, such as light emitting diodes (LEDs) and photodiodes (PDs) which eases its adaptation and enables significant energy and cost saving by reusing the existing lighting infrastructures for communication purposes. The data is transmitted on radiated optical intensity of the optical domain. Energy and spectrum efficient digital modulation techniques have been adopted for data transmission over VLC link. However, these techniques are affected by high-power peaks that induce signal distortion that is introduced by limited operating region of the light source. In this thesis, solutions to reduce the high power peaks challenge are implemented and their performance is investigated through simulation, analytical, and experimental studies.

Abstract

Visible light communication (VLC) is an optical wireless communication (OWC) technology that has the potential to provide high data rate transmission for indoor applications. VLC is a promising alternative technology with a large and unlicensed spectrum to complement the congested radio frequency (RF) based communication to meet the exponential growth and popularity of smart devices, and data-intensive services and applications. The use of low-cost commercially available front-end devices, further highlights the attraction of VLC system. However, nonlinear dynamic range of front-end devices and optical channel impairments limit full exploitation of VLC available modulation bandwidth. To fully benefit from the inherent resources and mitigate these limitations, multicarrier modulation (MCM) techniques are adopted. However, these techniques are affected by high peak-to-average power ratio (PAPR) which imposes constraints on the limited dynamic range of the front-end devices and the average radiated optical power. The main focus throughout this thesis is to reduce the high PAPR of MCM modulation techniques based VLC system by implementing pilot-assisted (PA) technique. Additionally, performance of PAPR reduced modulation techniques is investigated through analytical, simulation, and experimentally.

This thesis first presents background of VLC system principles including the front-end devices, VLC channel, system impairments and challenges, and employed solutions. The principles, limitations, and performance of MCM modulation variants that are implemented in this work are presented. Moreover, principles of PAPR challenge in MCM based VLC, PAPR evaluation, impact on the transmitted signal as well as the existing PAPR reduction techniques are discussed. Looking at the gap, a PA is implemented as PAPR reduction technique which is presented in this work including its implementation and performance.

Following that, analytical investigation of clipping noise that leads to distortion in a VLC system due to front-end devices limitations is presented. To minimise the clipping noise, PAPR of the system is reduced by the PA technique. The analytical BER performance of the system with PAPR reduction is verified through simulation and then compared to that of the conventional system without PAPR reduction at similar clipping levels. The PA proposed system shows better BER performance at all clipping levels.

Finally, multiple experimental studies on PAPR reduction of PA technique are presented. Two experimental demonstrations on the efficacy of PA PAPR reduction for pulse-amplitude modulated discrete multitone modulation (PAM-DMT) and direct current optical orthogonal frequency division multiplexing (DCO-OFDM) based VLC using a single blue LED are presented. These studies are comparing the bit-error-rate (BER) performance of the proposed systems with conventional counterparts over a range of sampling rate. This shows that, the proposed systems perform better than conventional systems without PAPR reduction. The results are validated through simulation. Other two experimental studies on the previous systems with parameters optimisation and available modulation bandwidth utilisation are presented, which show that the proposed systems outperform the conventional systems in terms of BER. This is followed by investigating the PA PAPR reduction effect on the achievable data rate of a wavelength division multiplexing (WDM) based VLC system using three different LEDs for PAPR reduced DCO-

OFDM and PAM-DMT systems. The proposed systems have achieved more than 8% data rate higher than that of conventional systems without BER performance degradation.

Declaration of originality

I declare that this thesis was composed by myself, the work contained herein is my own except where explicitly stated otherwise in the text, and this work has not been submitted for any other degree or professional qualification except as specified.

Hussien Theeb Alrakah

Edinburgh, Scotland, The United Kingdom

November 2022

Acknowledgements

I sincerely acknowledge the special favour bestowed upon me by almighty Allah that helps me to write this thesis.

My appreciation goes to Jazan University, Kingdom of Saudi Arabia for funding my PhD program in full.

Special thanks to my supervisor, Dr Wasiu O. Popoola, for his constant support, guidance and invaluable comments throughout my research time with his research group. I also thank him for welcoming me and granting me the opportunity to carry out my research under his supervision and as a result, benefit from his knowledge and experience.

I also would like to express my gratitude to the research group with whom I worked during my research.

I wish to extend my gratitude to my mother, for her prayers and care, as well as to my dear wife, for her sacrifice especially during the difficult times, and to my kids, Rahaf and Yaccob, for the love and joy they always bring to our lives.

Contents

List of figures

List of tables

Acronyms and abbreviations

ACE	active constellation extension
ACO-OFDM	asymmetrically clipped optical orthogonal frequency division multiplexing
ACO-SCFDM	asymmetrically clipped optical single-carrier frequency division multiplexing
ADC	analogue-to-digital converter
ADO-OFDM	asymmetrically DC-biased optical orthogonal frequency division multiplexing
APD	avalanche photodiode
ASE-DMT	augmented spectral efficiency discrete multitone
AWG	arbitrary waveform generator
AWGN	additive white Gaussian noise
BER	bit-error-rate
CCDF	complementary cumulative distribution function
CIR	channel impulse response
CLT	central limit theorem
CM	cubic metric
CNC	clipping-noise-cancellation
CP	cyclic prefix
DAC	digital-to-analogue converter
DC	direct current
DCO-OFDM	direct current optical orthogonal frequency division multiplexing
DD	direct detection
DFE	decision feedback equalizer
DMT	discrete multi-tone

DSP	digital signal processing
eACO-OFDM	enhanced asymmetrically clipped optical orthogonal frequency division multiplexing
E-ACO-SCFDM	enhanced asymmetrically clipped optical single-carrier frequency division multiplexing
EM	electromagnetic spectrum
ePAM-DMT	enhanced pulse-amplitude modulated discrete multitone modulation
eU-OFDM	enhanced unipolar orthogonal frequency division multiplexing
EVM	error vector magnitude
FDE	frequency-domain equaliser
FEC	forward error correction
FFE	feedforward equaliser
FFT	fast Fourier transform
FOV	field of view
FPGA	field programmable gate arrays
FSO	free space optical
HACO-OFDM	hybrid asymmetrical clipped orthogonal frequency division multiplexing
IAPR	instantaneous-to-average power ratio
ICI	inter-carrier interference
IEEE	Institute of Electrical and Electronic Engineers
IEEE	Institute of Electrical and Electronics Engineers
IFFT	inverse fast Fourier transform
IGA	iterative gradient algorithm
IM/DD	intensity modulation and direct detection
IM	intensity modulation
IoT	internet of things
IP	internet protocol
ISI	inter-symbol interference

L/E-ACO-SCFDM	layered/enhanced asymmetrically clipped optical single-carrier frequency division multiplexing
LACO-OFDM	layered asymmetrically clipped optical orthogonal frequency division multiplexing
LD	laser diode
LED	light emitting diode
LMS	least mean squares
LOS	line of sight
LSB	lower side band
LTE	long term evolution
M2M	machine to machine
MCM	multi-carrier modulation
MIMO	multiple-input and multiple-output
ML	maximum likelihood
mm-Wave	millimetre waves
MMSE	minimum mean squared error
M-PAM	M-ary pulse-amplitude modulation
NLOS	non-line of sight
NRZ	non-return-to-zero
OFDM	orthogonal frequency division multiplexing
OFDMA	orthogonal frequency division multiple access
O-OFDM	optical orthogonal frequency division multiplexing
OOK	on-off keying
OWC	optical wireless communications
PA DCO-OFDM	pilot-assisted DCO-OFDM
PA PAM-DMT	pilot-assisted PAM-DMT
PA	pilot-assisted
PAM	pulse amplitude modulation

PAM-DMT	pulse-amplitude modulated discrete multitone modulation
PAPR	peak-to-average power ratio
PC-LED	phosphor-converted LED
PD	photodetector
PIN	P-type intrinsic N-type photodiode
PIN-PD	P-type intrinsic N-type photodiode
PMEPR	peak-to-mean envelope power ratio
PPM	pulse position modulation
PRT	peak reduction tones
PSD	power spectral density
PTS	partial transmit sequence
PWM	pulse-width modulation
QAM	quadrature amplitude modulation
RF	radio frequency
RLS	recursive lease squares
RONJA	Reasonable Optical Near Joint Access
SCFDM	single-carrier frequency division multiplexing
SEE-OFDM	spectral and energy efficient optical orthogonal frequency division multiplexing
SLM	selective mapping
SNR	signal-to-noise-ratio
SPAD	single photon avalanche diode
SSL	solid-state lighting
TI	tone injection
TIA	trans-impedance amplifier
TR	tone reservation
U-OFDM	unipolar orthogonal frequency division multiplexing
USB	upper side band

VLC   visible light communications

VLCC   visible light communication consortium

VPPM   variable pulse position modulation

WDM   wavelength division multiplexing

ZFE   zero forcing equaliser

Nomenclatures

P_{opt}	Average optical power
A_{r}	Active area
$w(t)$	Additive white Gaussian noise
$\mathrm{BER}(\mathrm{M}_k, \mathrm{SNR}_k)$	Analytical BER at a subcarrier k with modulation order M_k and a SNR_k
ψ	Angle of incidence
$P_{\mathrm{b(elec)}}$	Average electrical power per bit
$P_{\mathrm{s(elec)}}$	Average electrical power per symbol
P_{avg}	Average power
B	Bandwidth
G_{B}	Bandwidth utilisation factor of DCO-OFDM frame
i_{bias}	Bias current
P_{bias}	Biasing power
K_{B}	Boltzmann's constant
k_{b}	Bottom clipping level
$H(0)$	Channel DC gain
$H[k]$	Channel impulse response at sample k
$h(t)$	Channel impulse response
$H[m]$	Channel response at symbol m
$x_{\mathrm{clip}}(t)$	Clipped continuous time domain signal
κ	Clipping attenuation factor
U	Cluster of data symbols
$\hat{U}$	Cluster of data symbols and pilot symbol
$\mathrm{Q(u)}$	Complementary cumulative distribution function of the PDF of the standard Gaussian di
$x_{\mathrm{ACO}}(t)$	Continuous time domain signal of ACO-OFDM
$*$	Convolution operator
N_{CP}	Cyclic prefix length
R_b	Data rate
I_{DC}	DC bias current
β_{DC}	DC bias level

δ	Dirac function
$y[n]$	Discrete time received waveform
$x_{\mathrm{clip}}[n]$	Discrete DC biased and clipped time domain waveform
$x_{dc}[n]$	Discrete DC biased time domain waveform
$x[n]$	Discrete time domain waveform
d	Distance
$A_{\mathrm{eff}}(\psi)$	Effective detection area
P_{elec}	Electrical power
B_{DC}	Electrical power penalty due to the addition of a DC bias in DCO-OFDM
$B_{\mathrm{DC}}^{\mathrm{dB}}$	Electrical power penalty in dB due to the addition of a DC bias in DCO-OFDM
$E_{\mathrm{b(elec)}}/N_0$	Electrical SNR
ζ	Electrical-to-optical conversion coefficient
q	Electron charge
E_{b}	Energy per bit
$\hat{X}[m]$	Equalised data symbol m
$\hat{\theta}_{\mathrm{p}}[m]$	Estimated pilot phase
Ψ_{FOV}	Field of view of a detector
f	Frequency
$H(f)$	Frequency domain channel impulse response
$T(\psi)$	Gain of a receiver with optical filter
$g(\psi)$	Gain of non-imaging concentrator
$Q(\cdot)$	Gaussian Q-function
E_2	Higher energy level
N	IFFT/FFT length
$\jmath$	Imaginary unit, i.e. $j = \sqrt{(-1)}$
$x(t)$	Input time domain waveform
m	Lambertian order
$h_{\mathrm{LOS}}(t)$	Line-of-sight channel impulse response
$H_{\mathrm{LOS}}(0)$	Line-of-sight DC channel impulse response
R_{L}	Load resistance in Ω
i_{max}	Maximum current
P_{max}	Maximum optical power
P_{max}	Maximum power of a LED's linear dynamic range

$i_{\min}$	Minimum current
$P_{\min}$	Minimum power of a LED's linear dynamic range
(M)	Modulation order
M_k	Modulation order at sample k
$B_{\mathrm{PAM}}[k]$	M-PAM symbols carrying useful data k
w_{clip}	Nonlinear distortion
$k_{\mathrm{b_{norm}}}$	Normalised bottom clipping level
$k_{\mathrm{t_{norm}}}$	Normalised top clipping level
N_{subs}	Number of active subcarriers
b	Number of bits
b_k	Number of bits per symbol
R	Number of pilot iterations
$E_{b(opt)}/N_0$	Optical SNR
E_1	Original lower energy level
$X[k]$	Orthogonal subcarriers in frequency domain
$Y[k]$	Output frequency domain waveform
$y(t)$	Output time domain waveform
L	Oversampling factor
PAPR_0	PAPR threshold
V_{pp}	Peak-to-peak voltage
X_{mp}	Phase rotated dada symbol
E_{p}	Photon energy
$A_{\mathrm{p}}[m]$	Pilot amplitude at sample m
$X_{\mathrm{p}}^{\tilde{r}}[m]$	Pilot iteration with minimum PAPR
$\theta_{\mathrm{p}}[m]$	Pilot phase at sample m
X_p	Pilot sequence
h	Planck's constant
$\phi(u)$	Probability density distribution of the standard Gaussian distribution
P_{PAPR}	Probability of PAPR exceeds a particular threshold
η_{qe}	Quantum efficiency
ϕ	Radiant intensity angle
$R_{\mathrm{o}}(\phi)$	Radiant intensity pattern at angle ϕ
$\tilde{A}_{\mathrm{p}}[m]$	Received corrupted pilot amplitude

$\tilde{\theta}_{\mathrm{p}}[m]$	Received corrupted pilot phase
$Y[m]$	Received data symbol m
$P_{\mathrm{r-NLOS}}$	Received power for Non-LOS link
$P_{\mathrm{r-LOS}}$	Received power of line-of-sight scenario
A_{PD}	Receiver detection area
$H_{\mathrm{refl}}(0)$	Reflected path gain
n_{r}	Refractive index of an optical concentrator
ν_k^2	Relative energy at symbol k
R_{PD}	Responsivity of photodetector
f_s	Sampling Frequency
T_s	Sampling period
$x_{\mathrm{scaled}}[n]$	Scaled discrete time domain signal
α	Scaling factor
$\Phi_{1/2}$	Semi-angle of a LED
N_{o}	Single sided power spectral density of AWGN
SNR_k	SNR at sample k
$E_{\mathrm{b}}N_{\mathrm{o}}$	SNR per bit
η_{ACO}	Spectral efficiency of ACO-OFDM
η_{DCO}	Spectral efficiency of DCO-OFDM
$\eta_{\mathrm{PAM-DMT}}$	Spectral efficiency of PAM-DMT
c	Speed of light
σ_x	Standard deviation
$\mathrm{E}[\cdot]$	Statistical expectation
$X[k]$	Subcarrier at the discrete frequency k
k	Subcarrier index
Δf	Subcarrier spacing
P_e^T	Target error probability
T	Temperature in Kelvin
$x_0^2(t)$	Time domain signal power before clipping
$|H_0|^2$	Time invariant channel gain
$[k_{\mathrm{t}}$	Top clipping level
P_{t}	Transmitted power
σ_x^2	Variance of a signal x

$\sigma^2_{w_{\mathrm{clip}}}$	Variance of clipped signal
σ^2_n	Variance of discrete signal
$\sigma^2_{x_{\mathrm{scaled}}}$	Variance of scaled signal
σ^2_{shot}	Variance of shot noise
$\sigma^2_{\mathrm{thermal}}$	Variance of thermal noise
σ^2_{w}	Variance of white noise
λ	Wavelength

Chapter 1
Introduction

1.1 Motivation

The demand for wireless access is growing exponentially and is expected to surge significantly in the near future. This is primarily due to the increase in the number of internet users and newly emerging technologies and services such as internet of things (IoT), machine to machine (M2M) connectivity, augmented and virtual reality (AR/VR), smart televisions and cloud services [1]. It is estimated that nearly two-thirds of the global population will have internet access by the year 2023 which means that 5.3 billion internet users compared to 3.9 billion users in 2018 [2]. The number of the global connected devices to the network will be more than three times of the number of total population and half of that connected devices will be M2M connections by 2023. Therefore, the overall number of connected M2M is expected to reach to 14.7 billion in 2023 [2]. The global internet protocol (IP) traffic growth has increased three folds between 2017 and 2022 which means that the internet traffic generated has reached 396 Exabytes per month by 2022. Non-PC devices have contributed 81% of the global IP traffic [1]. This rapid growth in connectivity and huge demand for high data rate is expanding the necessity for more resources of the limited available radio frequency (RF) spectrum and infrastructures of existing networks. Therefore, supporting technologies and complementary networking infrastructures are required to complement the congested, licensed and expensive RF spectrum. Various technologies are considered as candidate solutions with higher frequency spectrum to ease the demand on the RF technology such as millimetre waves (mm-Wave) and visible light communications (VLC) [3].

VLC systems have been attracting enormous research interest as an attractive complementary solution for the congested frequency spectrum of RF. VLC occupies the nano-meter wavelength region ranging between $\sim$380 nm and $\sim$780 nm of the electromagnetic spectrum (EM). Additionally, VLC has a unique property that enables a dual functionality of illumination and high speed wireless communication. Moreover, it offers huge and unlicensed spectrum for high data rate transmission. In addition, the use of low-cost commercially available off-the-shelf

front end devices, such as light emitting diode (LED)s and photodetector (PD)s, further highlights the attraction of VLC technology. Furthermore, significant energy and cost saving can be enabled by reusing the existing lighting infrastructures for communication purposes [4]. VLC technology is a potential candidate for a range of innovative applications such as indoor communication, indoor positioning and localisation, M2M communication, underwater communications, and IoT [5,6]. In addition, VLC system offers inherent security and can be employed in homes, offices, intelligent transportation systems and places where sensitive electronic devices exist such as in hospitals and areas that are non RF friendly environments [5–9]. Visible light communication consortium (VLCC) was established to provide standardisation for VLC technologies. The standardisation draft for light communication (IEEE 802.15.7-2018) was issued and approved by Institute of Electrical and Electronics Engineers (IEEE) group for short-range optical wireless communications (OWC) [10]. The IEEE 802.15.7 is the completed standard by IEEE for MAC and physical layers [11].

The advancement of solid-state lighting (SSL) LEDs, their low cost, long operational lifetime, high energy efficiency, and easy maintenance enable wide adoption of LED in most illumination applications. As a result, LED lighting is expected to dominate 84% of the illumination market in 2030 [5]. Consequently, this enables the emergence of VLC for data connectivity. Therefore, innovative applications have emerged due to the advancement and advantages of LEDs technologies. Moreover, the fast-switching speed property of LED enables the data modulation on the radiated intensity with eye safety consideration [12]. This property allows for data transmission using the intensity of the LED in addition to the prime illumination functionality. The advantages of VLC technology have enabled enormous research interest in recent years for various VLC applications such as indoor communication [13, 14], positioning [15–17], vehicular communication [18–21] and underwater communication [22, 23].

The VLC system uses off-the-shelf incoherent optical components which restrict the signal propagation and reception mechanism to intensity modulation and direct detection (IM/DD). Modulation techniques such as on-off keying (OOK), pulse amplitude modulation (PAM) and pulse position modulation (PPM) can be implemented straightforward for the VLC system [24]. However, the performance of such schemes degrades as their spectral efficiency increases due to the high inter-symbol interference (ISI) [7]. Optical orthogonal frequency division multiplexing (O-OFDM) technique is an alternative candidate for VLC for its advantages such as simplified single-tap equaliser, multi-path propagation resilience, ISI mitigation and robustness

against channel frequency selectivity [25–28]. The O-OFDM signal is required to be real and positive to meet the the IM/DD requirement. Therefore, Hermitian symmetry is imposed into the time domain signal of the O-OFDM to obtain a real signal [29]. The unipolar O-OFDM signal can be obtained by various techniques such as direct current (DC) bias, clipping at zero level and unpopular methods. The widely employed modulation technique in VLC system is direct current optical orthogonal frequency division multiplexing (DCO-OFDM) where DC bias is added to the signal to create a unipolar signal. However, the unipolar signal is obtained at a significant energy loss [29]. Various unipolar O-OFDM modulation techniques were proposed as energy efficient alternatives to the widely known DCO-OFDM such as: asymmetrically clipped optical orthogonal frequency division multiplexing (ACO-OFDM) [30], unipolar orthogonal frequency division multiplexing (U-OFDM) [31], Flip-OFDM [32] and pulse-amplitude modulated discrete multitone modulation (PAM-DMT) [33]. In these techniques, the frame structures are exploited to realise a unipolar signal. However, the restrictions imposed on their frame structures result in spectral efficiency losses which make their spectral efficiency equal to half of that of DCO-OFDM.

In spite of the advantages of applying O-OFDM for the VLC, they all are effected by inherent high peak-to-average power ratio (PAPR). The O-OFDM variants whose signals comprises of the sum of independent subcarriers in the time domain which results in individual subcarriers added up coherently to produce high PAPR peaks [34]. Consequently, high electrical peaks must be clipped at lower and/or upper levels to contain the signal swing inside the inherently limited dynamic range of LED to avoid driving the optical driver into and beyond its saturation region [35]. As a result, this clipping constraint induces undesirable signal distortion and clipping noise which degrade the performance of the system. Therefore, the high electrical PAPR values must be reduced to benefit from the dynamic range of the optical light source in full. Reducing the high PAPR values will help the optical light source to operate inside its linear dynamic region and hence, reduces the clipping distortion of the transmitted signal caused by the nonlinearity [26, 36]. Various solutions have been proposed to address the PAPR challenge. The electrical PAPR reduction techniques are classified into distortion and distortion-less techniques. The distortion techniques are the ones distort the signal to achieve PAPR reduction at the expense of system performance. This include: clipping and filtering [37–41], peak windowing [42], companding [43] and peak cancellation [44, 45]. On the other hand, the distortion-less techniques include multiple signalling and probabilistic techniques, and coding techniques. The multiple signalling and probabilistic techniques work in one of two ways.

The first way is achieved by generating multiple permutations orthogonal frequency division multiplexing (OFDM) signal and selecting the signal with the lowest PAPR for transmission. The second way relies on modifying OFDM signal by introducing phase shifts, adding peak reduction carriers or modifying constellation points [37]. This includes techniques such as: selective mapping (SLM) [26, 46–49], partial transmit sequence (PTS) [39, 50–53], tone injection (TI) [54], tone reservation (TR) [55], active constellation extension (ACE) [56, 57], constrained constellation shaping [58]. Coding techniques for PAPR reduction purposes in OFDM includes, linear block coding [59–61] and turbo coding [62–64]. The importance of optimal condition of the O-OFDM signalling prior to transmission has encouraged significant research effort being directed towards PAPR property and average transmitted power reduction techniques in O-OFDM. Therefore, this research on PAPR reduction of the transmitted optical power under the restricted dynamic range of the VLC system is well motivated.

In this work, pilot-assisted (PA) technique is considered and implemented for PAPR reduction and its performance for O-OFDM based VLC system is studied through simulation, analytical, and experimentally. PA technique is an effective solution for high PAPR peaks reduction which was proposed in [26]. PA technique is used to rotate the data frame phase by a randomly generated pilot sequence in order to avoid coherent addition of the subcarriers as much as possible. Number of phase iterations are used to rotate the phase of data symbol in the frequency domain and evaluate the PAPR in the time domain that is obtained by inverse fast Fourier transform (IFFT) operation. The pilot sequence that generates the lowest PAPR signal is embedded with the data symbols for transmission. The pilot symbol's phase is chosen based on the SLM algorithm while the maximum likelihood (ML) algorithm is used to recover the pilot phase at the receiver side [65]. The performance of PA is evaluated using PAPR metric and its impact on the bit-error-rate (BER), signal-to-noise-ratio (SNR) and achievable data rate of the O-OFDM based VLC system is studied experimentally and compared to the performance of the conventional system without PAPR reduction. Furthermore, the PA PAPR reduction impact on the clipping noise caused by the nonlinearity of LED is presented in this thesis. Generalised details of the PA technique for O-OFDM based VLC system is presented in Chapter 3.

1.2 Objectives

The aim of this thesis is to reduce the high PAPR peaks of O-OFDM modulation techniques based VLC for the purpose of improving the system performance. The effect of reducing the

high PAPR peaks on the clipping noise is investigated analytically and verified through simulation, then the results are compared with counterpart conventional system without PAPR reduction technique implemented. An implementation of PA technique to reduce the high PAPR of O-OFDM variants is carried out experimentally for single and wavelength division multiplexing (WDM) VLC links. The experimental performance of PA scheme is verified through simulation. The performance of the proposed system is compared with conventional system without PAPR reduction. Furthermore, system performance optimisation through the used parameters and signal processing techniques is achieved to overcome limitations such as clipping noise that are imposed by frond-end devices of VLC system. In order to achieve these aims, specific objectives are as follows:

- Investigate, analytically, the impact of reducing the PAPR of O-OFDM signalling on the clipping noise then verify the results through simulation.

- Compare the obtained analytical and simulation results with that of conventional systems without PAPR technique implemented.

- Develop a PA based VLC system simulation framework that reduces the high PAPR peaks in O-OFDM modulation techniques.

- Evaluate, through simulation, the PAPR reduction gain using PA technique on differently distributed O-OFDM modulation techniques.

- Investigate, through simulation, the PAPR reduction impact using PA technique on the SNR and BER performance of the O-OFDM based VLC systems.

- Develop an experimental test-bed for a single blue LED VLC link, in order to investigate the performance of the PA PAPR reduced selected O-OFDM modulation techniques.

- Develop an experimental test-bed for VLC link with three-wavelengths, in order to investigate the performance of PAPR reduction of the O-OFDM techniques based WDM system.

- Compare the performance of the PA systems with the conventional counterpart systems without PA.

5

1.3 Contributions and Publications

The major contributions to knowledge made in this thesis will be outlined in this section in addition to the publications completed in the development of these contributions.

1.3.1 Contributions to Knowledge

The first major contribution of this thesis is to investigate the effect of PAPR reduction of DCO-OFDM system in the presence of double-sided clipping. The PAPR reduction is obtained by PA technique. The double-sided clipping is introduced to the time domain signal due to the limitation of the front-end devices of VLC system. The signal clipping introduces clipping noise and signal distortion to the transmitted signal. The attenuation factor and the variance of the clipping noise of the received waveform are determined in closed-form which included in the derivation and calculation of the system SNR. The system's BER performance of the PAPR reduced pilot-assisted DCO-OFDM (PA DCO-OFDM) system is investigated at three different clipping levels. The clipping levels are varied by the amount of the forward DC biasing that is added to the transmitted signal to fit the dynamic range of the light source. Analytical study of the proposed system performance in terms of BER is obtained and verified through simulation at the selected clipping levels. The BER performance of PA DCO-OFDM is then compared to that of conventional DCO-OFDM without PAPR reduction.

Another key contribution of this thesis is to evaluate and reduce the high PAPR peaks of the PAM-DMT waveform by implementing the PA technique. The system performance is investigated experimentally using a single blue LED for VLC link. The experimental performance of PA scheme is verified through simulation. The system parameters are optimised and the performance of the resulting pilot-assisted PAM-DMT (PA PAM-DMT) is utilised with adaptive bit and power loading and investigated experimentally in terms of BER and achievable data rate. The performance of PAPR reduced PA PAM-DMT and conventional PAM-DMT without PAPR reduction are compared in terms of BER over a range of sampling rates. The proposed PA PAM-DMT has achieved better BER performance in comparison to that of conventional PAM-DMT.

Finally, Another major contribution of this thesis is to reduce the undesirable high PAPR of DCO-OFDM and PAM-DMT using PA technique to minimises signal clipping and nonlinearity distortion caused by front-end devices, and maximise achievable data rate while maintaining

the error performance. PA DCO-OFDM and PA PAM-DMT based WDM VLC systems using three different off-the-shelf LEDs are experimentally demonstrated and their performance are investigated. WDM system is utilised to efficiently modulate the three different wavelengths. Additionally, signal processing technique (bit and power loading) is applied to improve the system performance by utilising the available bandwidth of each wavelength. Evaluation of PA DCO-OFDM and PA PAM-DMT systems' data rate and BER per wavelength are carried out and then compared to that of conventional DCO-OFDM and PAM-DMT without PAPR reduction respectively. The PA DCO-OFDM and PA PAM-DMT based WDM VLC system have achieved more than 8% data rate higher than that of their conventional counterparts without BER degradation.

1.3.2   List of Publications

Over the course of investigating the aforementioned contributions to knowledge, the following publications have been contributed:

1.3.2.1   Journal Papers

- **H. Alrakah**, T. Gutema, S. Sinanovic and W. Popoola, "PAPR Reduction in DCO-OFDM Based WDM VLC", in Journal of Lightwave Technology, vol. 40, no. 19, pp. 6359-6365, 1 Oct.1, 2022, doi: 10.1109/JLT.2022.3196505.

- **H. Alrakah**, M. Hijazi, S. Sinanovic and W. Popoola, "Clipping Noise in Visible Light Communication Systems with OFDM and PAPR Reduction", in Photonics (Under Review).

1.3.2.2   Conference Papers

- **H. Alrakah**, T. Gutema, S. Sinanovic and W. Popoola, "PAPR Reduction in PAM-DMT based WDM VLC", in 2022 13th International Symposium on Communication Systems, Networks and Digital Signal Processing (CSNDSP), 2022, pp. 174-178, doi: 10.1109/CSNDSP54353.2022.9907952.

- **H. Alrakah**, T. Gutema, F. Offiong, and W. Popoola, "PAPR Reduction in DCO-OFDM and PAM-DMT Based VLC Systems", in Conference on Lasers and Electro-Optics,

Technical Digest Series (Optica Publishing Group, 2022), paper JTh3B.38.

- **H. Alrakah**, S. Sinanovic and W. Popoola, "Pilot-Assisted PAPR Reduction in PAM-DMT based Visible Light Communication Systems", 2021 IEEE Latin-American Conference on Communications (LATINCOM), Santo Domingo, Dominican Republic, 2021, pp. 1-6, doi: 10.1109/LATINCOM53176.2021.9647764.

- K. Akande, F. Offiong, **H Alrakah** and W. Popoola, "Performance Comparison of MIMO CAP Receivers in Visible Light Communication", in 2018 11th International Symposium on Communication Systems, Networks and Digital Signal Processing (CSNDSP), 2018, pp. 1-5, doi: 10.1109/CSNDSP.2018.8471813.

1.4   Thesis Outline

This chapter provides an overview of the motivations behind VLC system including the wireless access demand and growth, the advancements of VLC technologies, concepts, and applications. Additionally, VLC system advantages and limitation are introduces, which suggest that VLC can provide high speed data transmission over a short distance in comparison with RF technologies. Techniques to overcome VLC system main challenges which are considered in this work are introduced. Furthermore, the objectives, aims, contribution to knowledge, list of publications, and thesis outline of this thesis are presented in this chapter. The remainder of the thesis is structured as follows:

Chapter 2 provides background information on OWC system focusing on VLC system. The background review includes the principles of the front-end devices, modelling of the VLC channel, noise, system impairments and challenges, and employed solutions. Description of single-carrier modulation techniques is given. Furthermore, O-OFDM modulation variants that are implemented in this work such as DCO-OFDM, ACO-OFDM and PAM-DMT are presented including principles, performance and limitations. Additionally, signal processing techniques that are adapted for performance improvement are presented.

Chapter 3 presents the principles of PAPR challenge in VLC system, PAPR evaluation in O-OFDM based systems and its effect on the transmitted signal. In addition, the existing PAPR reduction techniques that are proposed for OFDM based systems are discussed. Detail description of PA technique is presented including its implementation in O-OFDM and PAPR

reduction gain.

Chapter 4 presents an analytical study of the effect of PAPR reduction on the clipping noise that is induced by front-end devices of VLC system. The considered system (DCO-OFDM) with PAPR reduction technique included (PA DCO-OFDM) is described in the presence of clipping noise and the analysis of the attenuated received signal is given. The BER performance of the PAPR reduced PA DCO-OFDM system is given in the presence of clipping noise in addition to comparison with its counterpart conventional system without PAPR reduction implemented. Simulation result of error performance of the PA DCO-OFDM system is presented to validate the analytical result.

Chapter 5 presents experimental study of PA PAM-DMT system performance in a indoor single VLC link. The description of PA PAM-DMT based VLC system and the PAPR reduction procedure and gain through PA are presented. Additionally, the experimental setup, methodology, data transmission, and empirical results showing the PAPR effect on the error performance of the system are presented. The validation of the empirical results through simulation is given. Study of the experimental error performance of PA PAM-DMT system after its optimisation through signal processing techniques is presented in this chapter. The experimental optimised error performance result with comparison to conventional system without PAPR reduction is given as well.

Chapter 6 describes experimental demonstration and performance investigation of PAPR reduction in PA DCO-OFDM and PA PAM-DMT based WDM VLC utilising three different LEDs. Experiment setup of WDM system, system optimisation including wavelengths optimisation are presented. Systems performance in terms of BER and achievable data rate are presented and compared with the conventional systems without PAPR reduction.

Chapter 7 provides a conclusion for all the works presented in this thesis, limitations and suggested future work.

Chapter 2
Background and Literature Review

2.1 Introduction

In this chapter, the background concepts underlining this thesis, such as VLC technology and O-OFDM modulation scheme and its variant such as DCO-OFDM, ACO-OFDM and PAM-DMT are presented. The state-of-the-art regarding these concepts in the literature are presented in this thesis to give a solid background for the used technology and techniques that are developed and implemented in this thesis. The background review include the principles of the front-end devices of VLC system, modelling of the optical wireless channel, signal processing techniques that are adapted for performance improvement, the fundamentals and challenges of the above mentioned technologies and techniques.

2.2 Optical wireless communications

The early forms of visual based communications are smoke signals, beacon fires. The earliest practical visual based communication system was the development of the optical telegraph by Claude Chappe 1792 [66]. However, the first historical information transmission using light was initially introduced and demonstrated by Alexander Graham Bell and his assistance Charles Sumner Tainter in 1880 [67]. The photophone invention in 1880 is considered to be the first practical OWC system that used the sunlight as a carrier to convey a voice messages over a distance of 200 m. The photophone based systems were outperformed and eclipsed by the success of radio-based communication in late 1890s due to their limited range and dependence on weather conditions [68]. The semiconductor based light sources advancement facilitated the emergence and development of optical communications. Gfeller's and Bapst's pioneering work in 1979 that introduced an infrared based OWC system, where 260 Mbps of data rate was achieved in short range wireless indoor environments [69]. OWC systems based on free space optical (FSO) communication for different range were studied extensively for back-haul applications [70, 71]. The invention of the blue LED by Isamu Akasaki enabled the existence

of the power efficient white light LED technologies [72]. This is in turn enabled Prof. Masso Nakagawa and his fellow researchers at Keio University in Japan to consider the white LEDs for lighting and communication purposes [73]. Many interesting applications have emerged due to this dual functionality of white LEDs. The dual functionality of LED is based on the fast-switching speed property which enabled the widespread of the VLC system [74]. This property allows for information to be propagated on the LED radiated power by rapid, steady flickering intensity without being perceived by human eyes. The high frequency switching property of LED is not available with other lighting technologies, hence, the VLC based LED systems provide the illumination and high speed connectivity simultaneously.

In OWC, there is high interest in using the VLC as it offers huge and unlicensed spectrum for high data rate transmission ranging between 400 THz and 800 THz (380 nm - 780 nm) when compared to the RF spectrum. The use of low-cost commercially available off-the-shelf front end devices, such as LEDs and PDs, further highlights the attraction of VLC system. VLC system is a potential candidate for many applications such as indoor positioning, underwater communications and internet of things (IoT). In addition, VLC system offers inherent security and can be employed in homes, offices and places where sensitive electronic devices exist such as in hospitals and areas where wired and radio-frequency (RF) wireless communications are not suitable [7–9, 75]. Furthermore, it can enable significant energy and cost saving by reusing the existing lighting infrastructures for communication purposes [4].

The first adaptation of VLC based LED device in the literature was reported in [76], where the modulation of an audio message is demonstrated using a visible beam emitting light from an LED traffic light. Full research into VLC for indoor environment and home network has started afterwards with the pioneering work in [77] by Tanaka *et al*, where wireless home networking is proposed using white coloured LEDs. Full duplex Ethernet point-to-point free space link established by the Reasonable Optical Near Joint Access (RONJA) in 2001, achieving 10 Mbps over a distance of 1.4 km [78]. VLCC was established by major research and industrial parties in Japan soon after in 2003 to provide standardisation for VLC technologies. The standardisation draft for light communication (IEEE 802.15.7-2018) was issued and approved by IEEE group for short-range OWC [10]. Using off-the-shelf LEDs and WDM technique, data rate of 15.7 Gbps have been achieved over a free space link of 1.6 m [79].

In order to fully realise the full advantages of VLC, the challenges associated with its deployment must be addressed. The VLC challenges emanate from its system components, the VLC

system components are shown in Fig. 2.1. The challenges can be related to the transmitter, channel, and the receiver. Various solutions including signal processing have been proposed to mitigate these challenges in order to achieve a reliable communication link. The challenges and the solutions that are employed to mitigate their impact on the VLC link are discussed in details in this chapter.

2.3 Front-End Devices
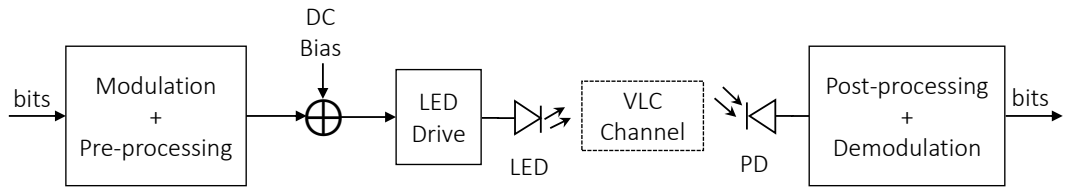
Figure 2.1: *VLC system components.*

The optical front-end in the VLC system can be divided into two main parts, transmitter and receiver as presented in Fig. 2.1. The VLC transmitter consists of a single or multiple light sources emitting at a single or multiple wavelengths. In addition, other optical components are used at the transmitter side such as lenses, reflectors and diffusers. In the other end, receiver incorporates a single or multiple photodetectors with the aid of other optical components such as lenses (concentrators), reflectors and filters. In the frond-end system design, the optical transmitter has to achieve the quality of service requirement while meeting the eye-safety standards. The optical receiver is required to capture enough photons to ensure appropriate detection of the transmitted signal [80]. SSL sources such as LEDs and laser diode (LD)s are the possible candidates for VLC transmitters. Photodetectors such as P-type intrinsic N-type photodiode (PIN-PD) and avalanche photodiode (APD) are suitable choice for VLC receivers due to their relatively high responsivity.

2.3.1 The Light Emitting Diode

LEDs are the most suitable light sources for VLC system due to their low power consumption, low cost, vast deployment as illumination source. LEDs radiate incoherent light by spontaneous emission process. This occurs when forward bias current is applied across a p-n junction of semiconductor materials which excites electrons in the material to move to higher energy level

13

[81, 82]. In the spontaneous process, the emitted photon is assumed to have same energy of the band-gap of the semiconductor's material. Then the thermal energy above absolute zero excites the electrons to travel to higher unstable energy level and when these electrons return to their original stable energy level, photons are emitted. The photons are emitted with energy that is proportional to the difference between the two energy levels. Assuming an electron drops back from the higher level E_2, to the original lower energy level E_1, a photon is emitted with energy $E_\mathrm{p} = E_2 - E_1$. The frequency f and the wavelength λ of the emitted photon is related to energy difference levels and the emitted photon energy can be given by the following [81]

$$E_\mathrm{p} = E_2 - E_1 = hf = \frac{hc}{\lambda} \tag{2.1}$$

where h is the Planck's constant and c is the speed of light. The incoherent light radiation is a result of a random process with no phase correlation between different photons in the energy level transition [81].

The radiation pattern of a LED can be approximated using a generalised Lambertian radiation model. The semi-angle at half power that is representing the field of view of a LED, $\Phi_{1/2}$, is used to characterise the radiation pattern. Therefore, the distribution of the radiant intensity pattern of a transmitter at angle, ϕ, is given by [83]:

$$R_\mathrm{o}(\phi) = \begin{cases} \dfrac{(m_1 + 1)}{2\pi} \cos^{m_1} \phi & \text{for} \quad \Phi \in [-\pi/2, \pi/2] \\ 0 & \text{for} \quad \phi \geq \pi/2 \end{cases} \tag{2.2}$$

where m is the Lambertian order expressing directivity of the light source beam, which is given by:

$$m_1 = \frac{-\ln 2}{\ln(\cos(\Phi_{1/2}))} \tag{2.3}$$

The Lambertian order m_1 is related to the transmitter semi-angle, $\Phi_{1/2}$, at half power hence, for commercially available LEDs, the $\Phi_{1/2}$ is around $60°$, which corresponds to $m_1 = 1$ [83]. The angle at the maximum radiated power corresponds to $\phi = 0$ [81]. Based on a desired application, a desired radiation pattern can be obtained using multiple LEDs and optical elements to minimise the radiated power loss, and interference and maximise the system throughput. This results in communications coverage improvement and spectral efficiency enhancement per unit area. The overall VLC system performance is affected by the current-voltage (I-V) and

luminance-current (L-I) transfer function of the light source. An ideal light source is assume to have a linear I-V and L-I transfer function. However, the commercially available LEDs have nonlinear I-V and L-I transfer function. The nonlinearity of the transmitter front-end limits its dynamic range which restricts the transmitted signal swing. Therefore, the nonlinearity distorts the transmitted signal and degrades the system SNR. The linear dynamic range of the light source is limited between its turn-on voltage and the optical power saturation. The turn-on voltage results in a lower level clipping distortion of the transmitted signal, whereas, the optical power saturation causes an upper level clipping of the signal. These clipping distortions contribute to the transmitted signal power, resulting in the average transmitted power by the transmitter within the linear region of its dynamic range. For example, blue LED (Vishay VLMB1500-GS08) has linear dynamic range between 20-100 mA where the waveform can be transmitted within this range without clipping nor saturation [84].

The frequency response of the transmitter is directly proportional to the system throughput. The frequency response of a LED is approximated with a low pass filter response. The 3-dB bandwidth of a LED is commonly used to contrast the frequency profile. The 3-dB bandwidth of a LED is proportional to the input bias current while considering the linear region of the LED dynamic range. The 3-dB bandwidth of common available LEDs is ranging between 10s of KHz and a few MHz, e.g. Vishay VLMB1500-GS08 LED has a 3 dB bandwidth of 11.7 MHz at input current of 20 mA. The low modulation bandwidth of a LED represents a bottleneck in achieving high speed communication based VLC. The roll-off of the frequency response of a LED is important since the modulation bandwidth of the LED can exceed the known 3-dB when equalisation algorithms are used. Practical frequency responses of three different RGB LEDs, Red: 598-8D10-107F, Green: 598-8081-107F and Blue: 598-8D90-107F are measured against the input bias current and their 3 dB values found to be 25.6 MHz, 37 MHz and 60.6 MHz at input bias current of 45 mA, 50 mA and 45 mA respectively, as shown in Fig. 6.4 of Section 6.3.2. Different types of LEDs are available such as white-coloured LEDs, phosphor-converted LED (PC-LED), micro-sized gallium nitride GaN LEDs, resonant cavity LEDs and organic LEDs.

2.3.2 The Laser Diode

Light amplification by stimulated emitted radiation (LASER) diodes (LDs) is another light source candidate for VLC system that generates light. The light radiation in LDs is based on

stimulated emission as the name suggests. The stimulated emission is a result of an external energy source (forward bias) that is incident on an atom in upper level energy E_2, which forces the atom to transit to lower energy level E_1. The energy change is emitted as a photon with the same phase and frequency of the incident which makes the emitted radiation coherent. The photon excitation by the external source stimulates the emission of another photon and so on [81]. The emitted photons enters a cavity with two different reflection ends, one with almost 100% reflection while the other is with very low reflection proprieties to allow for monochromatic light emission with very narrow wavelength band. This results in highly directional photons emission of the LD which is generally characterised by a Gaussian function [81, 85].

2.3.3 Photo-Detector

The key device in the front-end receiver of the optical system is a PD that converts the incoming optical signal into an equivalent electrical signal to retrieve the original transmitted data. Semiconductor photodetectors are commonly used in optical communication systems and known as Optical to Electrical converters (*photodiodes*). PD is characterised by light collection pattern, bandwidth, spectral response, detection area, sensitivity and noise figure. The signal generated by a PD is proportional to the instantaneous received optical power that is detected on the PD detection area. The detected optical signal is generally weak, having propagated through communication channel, hence, the PD must meet rigorous performance requirement such as high sensitivity, low noise level and sufficient bandwidth to achieve a desired data rate. Trade-off between bandwidth, gain, cost, etc is often considered to achieve the optical conversion which affects the PD's performance [81, 86]. The challenge at the receiver side is to capture sufficient photons to ensure correct detection of the transmitted signal. Ideally, large detection area of the receiver would allow to collect large number of photons. However, large detection area has a high capacitance which results in undesirable low bandwidth. Therefore, optical components such as concentrators are used [80].

The ratio of the number of the generated electron-hole pairs to the incident photons at the PD detection area in a given time is expressed as the quantum efficiency η_{qe} and defined as follows [81]

$$\eta_{qe} = \frac{\text{Electrons output}}{\text{Photons input}} \tag{2.4}$$

A common type of PD is the P-type intrinsic N-type photodiode (PIN), which is made up of an intrinsic material layer that is sandwiched between two layers of P-type and N-type semiconductor materials. In PIN, an incident photon is absorbed in the intrinsic layer which creates a photon-hole pair resulting in an electrical current flow. Another type of commonly used photodetector is APD, which uses the same principles in PIN photodiode with combination of significant photon amplification through avalanche effect to obtain a higher current from an incident photon, hence, higher gain [86]. This requires a higher revers bias current than that needed for a PIN photodetector leading to higher power requirement. The gain results in a higher sensitivity which promotes APD to applications where low optical power is expected at the detection area such as long range VLC systems and underwater OWC.

Single photon avalanche diode (SPAD) is another type of photodetectors in the optical field with high gain similar to APD. The SPAD operates in the Geiger region, where a single incident photon induces an avalanche effect that are directly detectable which allows for individual photons to be detected [87]. SPAD photodetectors have the highest sensitivity when compared with other PDs types. Therefore, SPADs are considered for severely attenuated received optical power scenarios such as downhole monitoring [88]. The bandwidth of SPAD is limited by the dead time which is required to detect newly arriving photons which quantifies the recovery time. The nonlinear response of a SPAD is another drawback due to the limitations in the maximum number of photons that SPAD can detect [88].

2.4   VLC Channels and Noise

The radiated power by a VLC optical source is incoherent and as a result, intensity modulation (IM) is adapted, where the modulating waveform $x(t)$ is impressed upon an instantaneous radiated intensity of the optical source of the VLC system. The radiated intensity is then detected using direct detection (DD) process to generate a proportional photo-current using a PD. Thus, the VLC channel is referred as IM/DD channel.

The VLC channel can be modelled as a baseband linear, time-invariant system model as shown in Fig. 2.2, and can be expressed as follows:

$$y(t) = \zeta R_{\text{PD}}(h(t) * x(t)) + w(t) \tag{2.5}$$

where $x(t)$ and $y(t)$ denote the channel input and output waveforms respectively, $h(t)$ is the
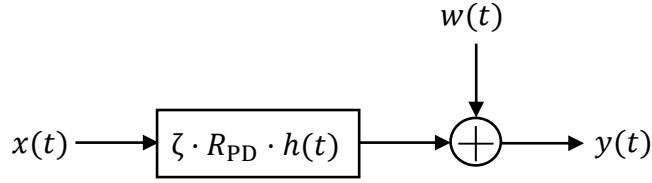
Figure 2.2: *VLC channel model.*

impulse response of the VLC channel, $w(t)$ is the additive white Gaussian noise (AWGN), R_{PD} represents the responsivity of the photodetector in A/W, ζ is the electrical-to-optical conversion coefficient of optical source in W/A and "$*$" symbol denotes the convolution operation. The two main sources of noise at the VLC receiver are shot and thermal noises. The shot noise is due to random fluctuation of the received photo-current, where the thermal noise is generated by the receiver electronics. The both noises are signal-independent noise and hence, the $w(t)$ can be modelled as AWGN with total noise variance, σ_w^2, and can be given by the following:

$$\sigma_w^2 = \sigma_{shot}^2 + \sigma_{thermal}^2 \tag{2.6}$$

The shot noise variance, σ_{shot}^2, can be estimated by the following [89]:

$$\sigma_{shot}^2 = 2qR_{PD}P_{opt}B \tag{2.7}$$

where q denotes the electron charge, P_{opt} is the received average optical power at the photodetector and B is the transmission bandwidth. The variance of the thermal noise, $\sigma_{thermal}^2$, is expressed by the following [89]:

$$\sigma_{thermal}^2 = \frac{4\mathrm{K_B}TB}{R_L} \tag{2.8}$$

where $\mathrm{K_B}$ is the Boltzmann's constant, T is the operating temperature in Kelvin and R_L is the load resistance in Ω.

In (2.5), the $x(t)$ corresponds to the instantaneous optical radiated power by the optical source and $y(t)$ is the generated photo-current by the receiving PD, which is proportional to the received instantaneous power over the PD's detection surface.

As the FSO channel input, $x(t)$, represents instantaneous optical power rather than amplitude signal, two fundamental constraints are imposed on the transmitted signal, $x(t)$. First, $x(t)$

must be non-negative and that is given by [81]:

$$x(t) \geq 0, \tag{2.9}$$

Secondly, a maximum transmitted optical power, P_{max}, must meet the eye safety requirement. Hence, the average transmitted power of $x(t)$ is restricted by a specified maximum power, P_{max}, and that is given by [81]:

$$P_{\text{max}} \geq \lim_{T \to \infty} \frac{1}{2T} \int_{-T}^{T} x(t) \, dt \tag{2.10}$$

The radiant intensity of the optical source at beam's angle, ϕ, is given by:

$$P(\phi) = R_{\text{o}}(\phi) P_{\text{t}} \tag{2.11}$$

where $R_{\text{o}}(\phi)$ is the radiant intensity pattern of the optical source at angle, ϕ, and given in (2.2) and P_{t} is the transmitted power.

The channel impulse response is determined by the VLC frond-ends frequency response in addition to the light reflections due to the multipath propagation. The frond-ends response is generally emulated by a low-pass frequency response, which can be estimated practically by the overall channel response in a line of sight (LOS) link. This limits the low-pass effect of the VLC channel into a DC channel gain. In VLC system, the LOS link length is short and the channel is considered non-frequency selective channel. Thus, the path loss depends on the square of the distance between the optical source and the photodetector. Therefore, a VLC link with a Lambertian optical source, a receiver with an optical filter with gain, $T(\psi)$ and non-imaging concentrator with gain, $g(\psi)$, the LOS scenario channel impulse response for a receiver with a detection area, A_{PD}, at distance, d, from the transmitter and angle, ϕ, is shown in Fig. 2.3, and can be expressed as follows [81]:

$$h_{\text{LOS}}(t) = \frac{A_{\text{PD}} R_{\text{o}}(\phi)}{d^2} T(\psi) g(\psi) \cos \psi \, \delta\left(t - \frac{d}{c}\right) \tag{2.12}$$

where $R_{\text{o}}(\phi)$ is the radiant intensity pattern of the optical source at transmittance angle, ϕ, which is given in (2.2), ψ is the angle of incidence, c is the speed of light in free space, $\delta\left(t - \frac{d}{c}\right)$ is the Dirac function and represents the signal propagation delay. The LOS channel impulse response expression in (2.12) assumes that $\phi < 90°$ and $\psi <$ field of view (FOV) and

the distance $d \gg \sqrt{A_{\text{PD}}}$. The non-imagining concentrator gain, $g(\psi)$, is given by:

$$g(\psi) = \begin{cases} \dfrac{n_{\text{r}}^2}{\sin^2 \Psi_{\text{FOV}}} & 0 \leq \psi \leq \Psi_{\text{FOV}} \\ 0 & \psi > \Psi_{\text{FOV}} \end{cases} \tag{2.13}$$

where n_{r} is the refractive index of the optical concentrator and the FOV of the receiver, $\Psi_{\text{FOV}} \leq \pi/2$. The non-imaging concentrator is usually used in exchange for large-area detector for indoor VLC system. Large-area detector increases the manufacturing cost in addition to junction capacitance which decreases the detector bandwidth and increases noise of the receiver. Therefore, optical concentrator is a cost-effective method to increase the overall effective detection area of the receiver. The effective detection area of the optical receiver at radiation incident angle, ψ, is given by [81]:

$$A_{\text{eff}}(\psi) = \begin{cases} A_{\text{r}} \cos \psi & 0 \leq \psi \leq \pi/2 \\ 0 & \psi > \Psi_{\text{FOV}} \end{cases} \tag{2.14}$$

where A_{r} is the active area that is collecting the radiation incident at angle ψ, which is usually smaller than the FOV of the optical receiver.
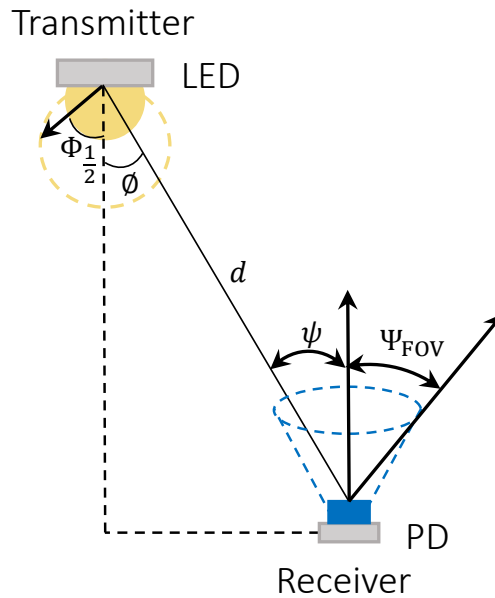
Figure 2.3: *Line-of-Sight (LOS) propagation model.*

Alternatively, the VLC channel can be characterised in frequency domain by applying the fast

Fourier transform (FFT) into the channel impulse response to attain the frequency response of the channel, $H(f)$, and can be obtained as follows [83]:

$$H(f) = \int_{-\infty}^{\infty} h(t)e^{-j2\pi ft} \, dt \tag{2.15}$$

The channel DC gain can be given from (2.15) as follows:

$$H(0) = \int_{-\infty}^{\infty} h(t) \, dt \tag{2.16}$$

The DC gain of the channel in LOS scenario can be estimated as follows [83]:

$$H_{\mathrm{LOS}}(0) = \begin{cases} \dfrac{A_{\mathrm{PD}} R_{\mathrm{o}}(\phi)}{d^2} T(\psi)g(\psi)\cos\psi & 0 \leq \psi \leq \Psi_{\mathrm{FOV}} \\ 0 & \psi > \Psi_{\mathrm{FOV}} \end{cases} \tag{2.17}$$

where ϕ is the transmittance angle, ψ is the angle of incidence, Ψ_{FOV} is the PD FOV, A_{PD} is the active detection area of the PD, $R_{\mathrm{o}}(\phi)$ is the radiation intensity and given in (2.2), d^2 is the distance between the transmitter and the receiver, $T(\psi)$ is the optical band-pass filter gain at the PD. The received power for a LOS scenario can be calculated using (2.17) and expressed as follows [81]:

$$P_{\mathrm{r-LOS}} = H_{\mathrm{LOS}}(0)P_{\mathrm{t}} \tag{2.18}$$

There could be non-directional LOS propagation with multi-order paths due to light reflections in indoor environments. Non-line of sight (NLOS) links are often referred to as a diffuse links and more complex to predict. In contrast to LOS links, NLOS links have a higher path loss and require a higher transmit power and a receiver with a larger collecting area. NLOS link modelling depends on many factors such as the room dimensions, plaster walls, ceiling, floor, various moving objects and partitions in the room between the transmitter and the receiver, the window size of the room, etc. [81, 83]. In general, the received power for NLOS link is defined as:

$$P_{\mathrm{r-NLOS}} = (H_{\mathrm{LOS}}(0) + H_{\mathrm{NLOS}}(0)) \, P_{\mathrm{t}} \tag{2.19}$$

$$= \left(H_{\mathrm{LOS}}(0) + \sum_{refl} H_{\mathrm{refl}}(0) \right) P_{\mathrm{t}} \tag{2.20}$$

where $H_{\mathrm{refl}}(0)$ represents the reflected paths gain. The radiated intensity that passes through a NLOS link arrives at the receiver through multiple paths with different gains at varying times. Thus, the impulse response is obtained by integrating all the multipath propagated components and detected at the receiver. The NLOS impulse response of multipath propagation is generally estimated using the Ray-tracing algorithm presented in [90] to generate an impulse response that includes higher-order reflections presented at the receiver. It is achieved by dividing a room surfaces into sub-blocks that act as receiving optical rays as given in (2.17) and illustrated by the NLOS paths in Fig. 2.4. Then, each reflective sub-block re-emits its corresponding optical rays with a reflectivity factor, ρ, as first-order Lambertian emitter with radiant intensity given in (2.2). However, replicas of the optical re-emitted signal will reach the receiver with different delays and path losses as a result of the diffused channel which would lead to ISI if the maximum delay spread of the diffused channel approaches the symbol duration [90]. In another approach, the received optical power of the NLOS link is evaluated using a single reflection only [69]. While, higher-order reflections, which arrive much later at the receiver than first-order reflections, may be ignored.
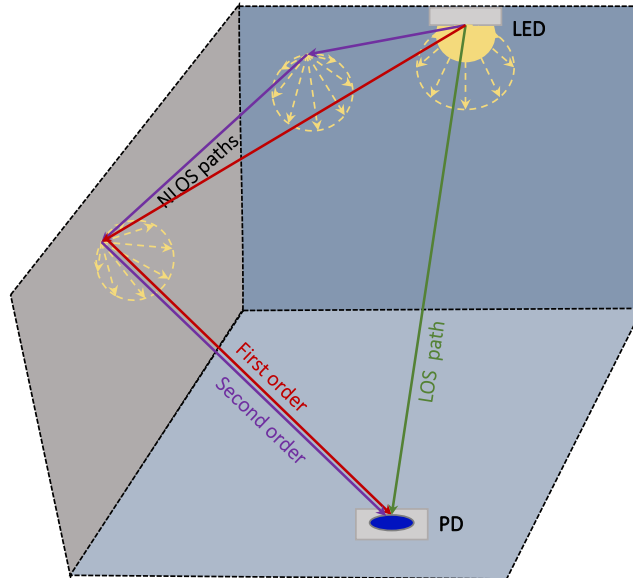
Figure 2.4: *LOS and NLOS propagation paths between a VLC frond-end devices.*

2.5 VLC system Impairments

The limited bandwidth of VLC system that has a LED as a light source is a major challenge. In addition, LED has a nonlinear operating region which restricts the transmitted signal amplitude swing and results in clipping of signals with high PAPR. Furthermore, the VLC link is generally short, hence, the range of transmission is limited due to the radiated optical power attenuation with distance. There are other challenge resources associated with the VLC link such as ambient light noise that significantly decrease the link SNR, resulting in BER degradation. Thus, signal processing techniques are adapted to address those challenges and improve the VLC system performance. In order to enhance the bandwidth of the VLC light source and compensate for the nonlinearity effect, the following signal processing techniques can be employed.

2.5.1 Bandwidth Enhancement

The modulation bandwidth of VLC system is generally low and the following techniques can be employed for enhancement.

- **Blue filtering:** Typically, white illumination is obtained by blue-emitting LED with yellow phosphor coating on the top of the blue LED chip such as in the case of PC-LED. The low modulation bandwidth is due to the slow time response when the entire white spectrum is detected at the receiver which limits the 3 dB bandwidth of the light source to ∼ 2-3 MHz [91]. However, the slow response of the yellow phosphor can be filtered out using a blue filter at the receiver, hence, the modulation bandwidth of the LED can be increased up to ∼ 20 MHz. The filtering of the yellow response results in power penalty due to the yellow components energy loss [12].

- **Pre-Equalisation:** The frequency response of LED is pre-equalised by employing an analogue circuit at the transmitter to increase the usable modulation bandwidth of a single LED [92]. The transmitted data is equalised by three parallel different drivers (low, medium and high) frequencies prior to biasing process. The pre-equalisation process requires initial measurement of the actual frequency response of the LED to design sufficient resonant frequency for equalisation. The pre-equalisation process is reported to increase the modulation bandwidth of a single LED to 45 MHz and increase the system data rate from 40 Mbps to 80 Mbps [12, 92]. Multiple LEDs are pre-equalised using a

driving technique to form a single link that achieves an aggregate bandwidth after tuning the frequency response of each LED by a resonant driving technique is reported in [93]. This technique improves the bandwidth of employed 16 LEDs from 2.5 Mhz to 25 MHz. The modulation bandwidth of the LED can be optimised in addition to the pre-equalisation process with bit and power loading technique when multi-carrier modulation (MCM) techniques are employed. To achieve this, larger constellation format can be assigned adaptively for the subcarriers that corresponds to higher modulation bandwidth while ensuring the error probability, P_e^T, is kept below a specified forward error correction (FEC) target. An another pre-equaliser is reported in [94], where a new model is proposed to compensate for the low frequency response of a white LED. Firstly, a LED frequency response model with one zero and two poles is proposed then used to design a pre-equaliser. The zero and poles of the equaliser can be adapted by the LED's to obtained an almost flat response improving the frequency response bandwidth of the white LED from ~1.5 MHz to about 100 MHz. Furthermore, data rate of 180 Mbps is demonstrated over 1.5 meters link with BER around 10^{-3} using OOK modulation technique [94].

- **Post-Equalisation:** Post-equalisation process uses a simple first order equaliser (zero forcing equaliser (ZFE)) which is performed at the receiver side followed by an amplification process. The proposed system is reported to improve the bandwidth from 3 MHz to 50 MHz and has yielded data rate of 100 Mbps [12]. The post-equaliser can be combined with pre-equaliser and work has been reported in [95] where the LEDs' frequency response bandwidth is increased by 65 MHz. The ZFE is a frequency-domain equaliser (FDE) which can be used to compensate for the optical channel impairments and can be implemented by multiplying the received OFDM symbols with the inverse of the estimated channel impulse response, and the resulting equalised symbol, $\tilde{X}[k]$, is given by [96]:

$$\tilde{X}[k] = \tilde{H}^{-1}[k] \times Y[k] \tag{2.21}$$

  where $\tilde{H}^{-1}[k]$ is the inverse of the estimated channel impulse response (CIR), $\tilde{H}[k]$, and $Y[k]$ is the received OFDM symbol. The CIR estimation can be found in (5.9). The ZFE is subject to noise enhancement at the amplification stage. Therefore, minimum mean squared error (MMSE) can be considered to minimise the error and avoid the noise enhancement [97]. Moreover, adaptive equalisers such as least mean squares (LMS) and recursive lease squares (RLS) can be implemented for high-speed VLC systems as they

are immune to noise enhancement and can be automatically adapted to the time-varying response of the VLC channel. The adaptive equalisers include decision feedback equalizer (DFE) and feedforward equaliser (FFE) have been implemented for VLC systems to achieve high data rate where training symbols are used for the adaptive equalizer weight adaptation [12, 98]. Training symbols lead to spectral efficiency losses, especially when the channel is time-variant, resulting in high computational complexity costs. Therefore, a trade-off must be considered between the adaptive equalizer gain and the spectral efficiency loss as well as the complexity of the computational process.

2.5.2 Nonlinearity Effect Compensation
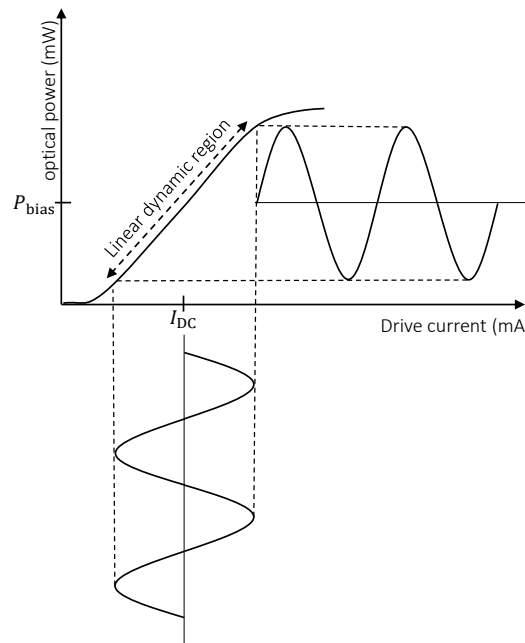
Figure 2.5: *The current-output power of an LED with bias current I_{DC} and P_{bias}.*

In the VLC system, LED is biased by a constant current source (DC bias current) that supports the entire forward voltage range across the LED. This is required to convert the transmitted bipolar signal to a unipolar corresponding signal for the incoherent transmission. The bias current is combined with the data waveform current, producing the total forward current through the LED. The total forward current through the LED and the system constraints imposed by the front-end devices yield the radiated optical power. Thus, the radiated optical power is proportional to the DC bias current [36]. However, the commercially available LEDs have nonlinear transfer function between the DC bias current and the output optical power. The nonlinear re-

lation is because of the p-n junction barrier and the saturation effect of the LED. The LED's nonlinear transfer characteristic can be described by the nonlinear relation between the DC bias current, I_{DC}, and the forward voltage, V_{pp}, which can be translated into nonlinear relation between the transmitted electrical power, P_{elec}, and the radiated optical power, P_{opt} [99].

The nonlinearity of the LED limits its dynamic range which restricts the transmitted signal swing. Therefore, the nonlinearity distorts the transmitted signal and degrades the system BER performance. Thus, to minimise the nonlinearity distortion of the VLC system, the transmitted data signal should be within the linear dynamic region of the LED. The linear dynamic region of the LED is limited between its turn-on voltage and the optical power saturation as shown in Fig. 2.5. The turn-on voltage results in a lower level clipping distortion of the transmitted signal, whereas, the optical power saturation causes an upper level clipping of the signal. The overall VLC system performance is affected by the clipping noise caused by the limited dynamic region of the front-end of the system where, these clipping distortions contribute to the average transmitted power by the LED within the linear region of its dynamic range [12, 36, 99]. Therefore, the data carrying signal should be transmitted within the linear dynamic region of the LED and this can be achieved by biasing the LED at the mid-point of its linear dynamic region. However, signals with high PAPR peaks is highly affected by the nonlinearity distortion and clipping noise caused by the limited dynamic range of the LED.

The nonlinearity effect of the LED has been compensated by different methods in the literature. Pre-distortion has been employed to compensate for the nonlinearity effect in [100], where a pre-distorter is used as a linearisation technique to compensate for the LED nonlinearity over a range of input current. Post-distortion technique has been applied in [101], to estimate and compensate for the nonlinearity effect of the LED at the receiver. Signal clipping technique is a simple method to overcome the nonlinearity distortion especially when MCM techniques are employed as they are affected by high PAPR values. Signal clipping makes the amplitude of the signal fall within the linear dynamic region of the LED where, the transmitted signal is clipped at the transmitter and the clipping process can be symmetrical or at lower and/or upper levels [26, 36, 102]. Clipping process usually degrades the error rate performance of the system because it is not reversible process at the receiver.

2.6 Modulation Techniques of VLC

The incoherent optical sources are widely believed to be prominent transmitter choices for VLC system due to their low cost, simplicity of design and ease of implementation. Due to incoherent optical sources' bandwidth limitations, modulation techniques with high spectral efficiency are crucial to the design of high speed VLC systems. The transmission mechanism in VLC system is IM/DD which restricts the transmitted waveform to be real and positive [81]. Different modulation techniques have been proposed and implemented in order to enable modulation techniques for the IM/DD optical systems.

Single-carrier modulation techniques such as OOK, pulse-width modulation (PWM), PPM and PAM can be simply implemented for VLC systems. However, the limited frequency response and the time dispersive channel of the VLC front-ends result in an ISI which degrades the performance of the system at high speed transmission. Therefore, at high data rate transmission, single-carrier modulation schemes require complex equalisation process at the receiver side. As a result, the performance of such schemes degrades as their spectral efficiency increases [7].

Another modulation approach for VLC systems implementation is single-carrier frequency division multiplexing (SCFDM) which is a promising key technology for long term evolution (LTE) network [103]. SCFDM has similar throughput and complexity performance of the well-known orthogonal frequency division multiple access (OFDMA) however, the SCFDM has better PAPR [103]. SCFDM variants including asymmetrically clipped optical single-carrier frequency division multiplexing (ACO-SCFDM), enhanced asymmetrically clipped optical single-carrier frequency division multiplexing (E-ACO-SCFDM) and layered/enhanced asymmetrically clipped optical single-carrier frequency division multiplexing (L/E-ACO-SCFDM) are proposed for VLC system in [104, 105]. In L/E-ACO-SCFDM, multiple information layers transmitted simultaneously to increase the spectral efficiency of ACO-SCFDM with its inherited low PAPR [104].

On the other hand, MCM techniques such as discrete multi-tone (DMT) modulation variants are regarded as convenient modulation candidates for VLC systems. This is due to their advantages such as simplified equalisation process, multi-path propagation resilience, ISI mitigation and robustness against channel frequency selectivity [26–28]. Different DMT modulation variants have been proposed for the IM/DD systems such as DCO-OFDM, ACO-OFDM and PAM-DMT. DCO-OFDM is a widely used modulation scheme for VLC system due to
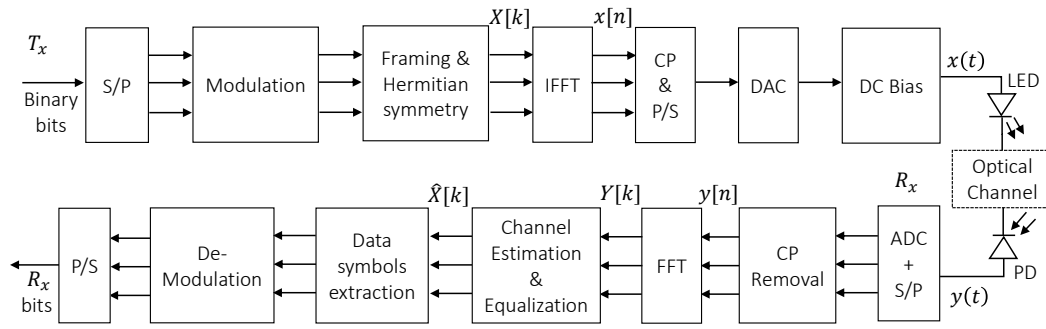
Figure 2.6: *Block diagram of Multi-carrier modulation techniques based VLC system.*

its high spectral efficiency when compared to other DMT techniques [106]. In addition, the light sources such as LEDs requires a DC bias, I_{DC}, to turn them on which already exists in DCO-OFDM for unipolar waveform conversion purpose [26]. Moreover, using DCO-OFDM in VLC offers an efficient use of the limited modulation bandwidth of illumination LEDs used in VLC [107]. However, DC bias is required to create the unipolar signal which results in significant energy losses [106]. ACO-OFDM and PAM-DMT systems are proposed in [108] and [33] respectively to overcome the energy losses in DCO-OFDM. In ACO-OFDM and PAM-DMT systems, the properties of Fourier transformation are used to exploit the frame structures. Therefore, the time-domain signal is clipped at the zero level to realise the unipolar signal and the DC bias is required only to turn on the light source [27]. Thus, ACO-OFDM and PAM-DMT are considered energy efficient schemes. However, the spectral efficiency of these schemes is half of the spectral efficiency in DCO-OFDM [109].

2.6.1 Single-Carrier Modulation Techniques

In OOK modulation scheme, the presence and absence of light intensity are used to encode the incoming binary bits. It is therefore possible to control illumination by adjusting the light intensity of the OOK two binary states without compromising the system performance. Similarly, multi-level intensity can be used to encode the binary bits with M-ary pulse-amplitude modulation (M-PAM) [110]. The M-PAM exploits the $(\log_2 M)$ levels to increase the spectral efficiency compared to OOK technique [111]. In the PPM, the incoming data bits are modulated into shorter duration with position index that varies the optical pulse position. PPM technique is more energy efficient with non-return-to-zero (NRZ) than OOK, however, PPM requires more bandwidth in order to achieve similar data rates of OOK [112]. Variable pulse

position modulation (VPPM) is a variant type that is controlled by the width of the pulse and would support dimming in conjunction with PPM to prevent the visible light flickering. The VPPM technique was proposed in IEEE 802.15.7 and considered as a combination of PPM and PWM techniques [113].

2.6.2 Multi-Carrier Modulation Techniques

2.6.2.1 DCO-OFDM

DCO-OFDM modulation technique general process is illustrated in Fig. 2.6. Information binary bits are generated and mapped into complex-valued multi-level, (M), quadrature amplitude modulation (QAM) symbols. The number of bits, b, that are mapped in each M in M-QAM symbols is given by $M = 2^b$. The mapped symbols are then modulated into orthogonal subcarriers $X[k]$, with subcarrier spacing $\Delta f = \frac{1}{NT_s}$, where N is the DCO-OFDM symbol length. The sampling period $T_s = \frac{1}{f_s}$, where f_s is the Nyquist sampling frequency and must be $f_s \geq 2B$, and B is the available bandwidth of the optical system.

The optical source is modulated by the intensity of a baseband real-valued waveform which means that the time-domain signal of DCO-OFDM must be real and positive. The real-valued signal is obtained by imposing Hermitian symmetry on the mapped symbols in frequency domain which is given by: $X[k] = X^*[N - k]$, for $k = 1, 2, \ldots N/2 - 1$, where $X[0] = X[N/2] = 0$ [114]. The DCO-OFDM frame in frequency domain is given by:

$$X[k] = \left[0, X_1, \ldots, X_{N/2-1}, 0, X^*_{N/2-1}, \ldots, X^*_1\right] \tag{2.22}$$

Applying the IFFT transformation on the frequency domain frame of DCO-OFDM in (2.22) transforms the the waveform to time-domain signal, $x[n]$, and given by [29]:

$$x[n] = \frac{1}{\sqrt{N}} \sum_{k=0}^{N-1} X[k]\, e^{j2\pi \frac{kn}{N}} ; \qquad 0 \leq n \leq N - 1 \tag{2.23}$$

where k is the subcarrier index and N is the IFFT/FFT length, which should be set to an even power of two value in order to satisfy the IFFT/FFT operation computational complexity of $\mathcal{O}(N \log_2(N))$.

The last few samples of each discrete time-domain waveform of DCO-OFDM are repeated at the beginning of each symbol as cyclic prefix (CP). CP length, (N_{CP}), must be greater than the channel delay spread to guarantee the ISI mitigation. Therefore, the DCO-OFDM symbol length becomes ($N + N_{\text{CP}}$). The CP is prefixed at the beginning of DCO-OFDM symbols to transform the linear convolution with the optical channel to circular one, which helps to equalise the effect of the channel efficiently in frequency domain using a single-tap equalizer [29]. The unipolar time-domain baseband waveform of DCO-OFDM is achieved by adding a sufficient DC bias level to the signal [115]. Details of DC bias requirements can be found in Fig. 2.8. Zero level clipping is applied on the transmitted waveform to clip any remaining negative peaks followed by digital-to-analogue converter (DAC) process to obtain a continuous time-domain waveform $x(t)$. DCO-OFDM waveforms are demonstrated in Fig. 2.7. The resulting continuous time-domain waveform $x(t)$ is used to modulate the optical source then the data signal is transmitted over the optical channel.

At the receiver, the received signal is detected by a PD which converts the received optical radiation into a current signal prior to the trans-impedance amplifier (TIA) which converts the current to corresponding voltage signal, $y(t)$. The voltage signal is then amplified to an appropriate level for analogue-to-digital converter (ADC) process. The received time-domain waveform, $y(t)$, is expressed by:

$$y(t) = x(t) * h(t) + w(t) \tag{2.24}$$

where $x(t)$ is the transmitted time-domain waveform, $h(t)$ is the optical channel impulse response, $w(t)$ is the AWGN at the receiver and "$*$" symbol denotes a convolution operation. The received serial waveform is converted to discrete time-domain waveform, $y[n]$, by the ADC then to parallel prior to the CP removal as shown in Fig. 2.6. The FFT property is then applied to obtain the frequency domain waveform and convert the convolution to a multiplication process. The FFT process is given by the following [29]:

$$Y[k] = \frac{1}{\sqrt{N}} \sum_{n=0}^{N-1} x[n] \, e^{-j2\pi \frac{kn}{N}} \; ; \qquad 0 \leq k \leq N - 1 \tag{2.25}$$

The frequency domain waveform, $Y[k]$, is expressed as follows:

$$Y[k] = X[k] \times H[k] + W[k] \tag{2.26}$$

where $H[k]$ is the CIR at sample k, $X[k]$ is the transmitted signal at sample k, and $W[k]$ is the frequency domain estimated AWGN at sample k, at the receiver. The data symbols are then extracted and the channel effect is estimated and the data carrying symbols are equalized using a ZFE that is given as follows:

$$\hat{X}[k] = \frac{Y[k]}{H[k]} \tag{2.27}$$

Reverse processes are then followed to recover the transmitted signal as shown in Fig. 2.6. The equalised data symbols are QAM demodulated, followed by BER calculation based on the demodulated binary streams. Representation of DCO-OFDM discrete time-domain waveforms is shown in Fig. 2.7, note that the same samples are plotted in (b), (c) and (d).
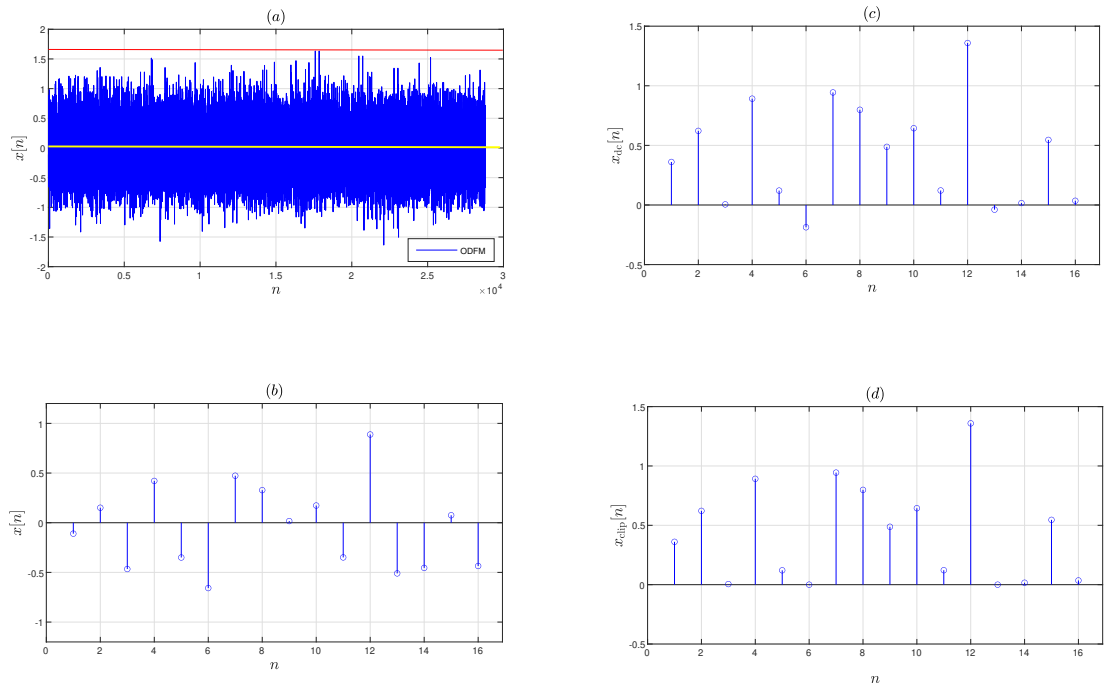
Figure 2.7: *DCO-OFDM waveform visualisation, (a) DCO-OFDM discrete time-domain signal, $x[n]$, (b) Number of samples of DCO-OFDM discrete time-domain signal, $x[n]$, (c) DC biased DCO-OFDM samples, $x_{\mathrm{dc}}[n]$, and (d) DCO-OFDM clipped DC biased samples, $x_{\mathrm{clip}}[n]$.*

The DC bias is employed for DCO-OFDM waveform to convert it from bipolar to unipolar waveform and to facilitate the minimum signal clipping caused by the frond-ends devices of

the VLC system. The DC bias can be defined as a β_{DC} multiple of the standard deviation, σ_x, of the signal in the time domain as shown in (2.28). The ideal DC bias point should be placed at the centre of the linear region of the light source dynamic range. The dynamic range of the optical source is the linear region between the turn-on voltage point and the saturation power point of the light source. The non distorted time-domain waveform of DCO-OFDM follows Gaussian distribution when the length of IFFT operation length is > 64 [36]. The DC bias required to convert the bipolar signal in DCO-OFDM to unipolar is written as follows [116]:

$$B_{DC} = \beta_{DC}\sqrt{E\{x_0^2(t)\}} \tag{2.28}$$

where $E[\cdot]$ is the statistical expectation, $x_0^2(t)$ is the time-domain signal power before clipping and β_{DC} is a non negative constant. The electrical power penalty due to the DC bias addition to the DCO-OFDM waveform in comparison with the bipolar OFDM is given by [106]:

$$B_{DC}^{dB} = 10\log_{10}(\beta_{DC}^2 + 1) \tag{2.29}$$
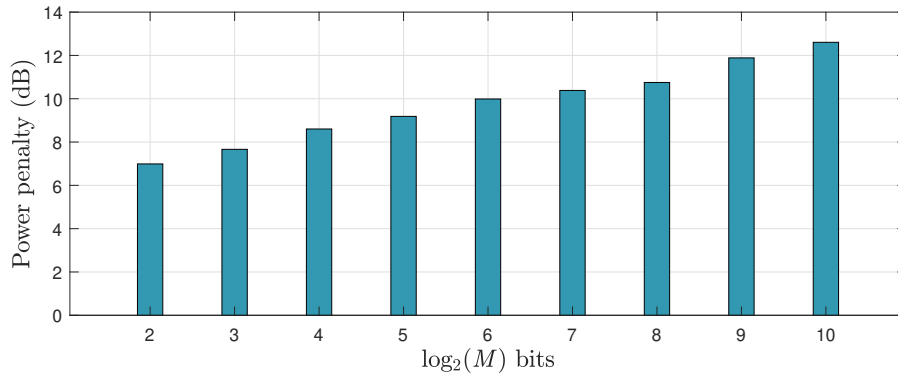
Figure 2.8: *Power penalty due to DC bias addition to DCO-OFDM compared with bipolar OFDM signal.*

Bipolar DCO-OFDM requires a large B_{DC} value to have the signal mean power placed in the centre of the light source dynamic range as shown in Fig. 2.8, ensuring lower and upper level clipping minimisation [36]. B_{DC} cannot be generalised for all constellation sizes because the additional dissipation of electrical power that caused by DC bias addition increases as the modulation order, M, increases. An estimation of the power penalty based on (2.29), at a BER target of 10^{-4} due to the DC bias requirement is shown in Fig. 2.8. This power penalty is calculated at the sufficient B_{DC} as shown in Table. 2.1 which is added to bipolar OFDM signal to make

the real-valued signal $x(t)$ unipolar. The condition $B_{DC} \geq |\min[x(t)]|$ must be met to avoid any lower level clipping of $x(t)$ by the front-ends devices of the VLC system. OFDM signals

QAM level	4	8	16	32	64	128	256	512	1024
β_{DC}	2	2.2	2.5	2.7	3	3.15	3.3	3.8	4.15
sufficient B_{DC}^{dB}	6.9	7.6	8.6	9.2	10	10.4	10.75	11.9	12.6
small B_{DC}^{dB}	3.9	-	6	-	7.3	-	9	-	-

Table 2.1: *Required DC bias levels for real-valued DCO-OFDM to be converted to unipolar signal as a function of modulation order.*

have high PAPR in general and it is practically impossible to convert all its negative samples into corresponding unipolar ones by adding DC bias. To investigate the effect of different DC bias levels on the clipping noise level, electrical power and therefore the BER performance, the transmitted signal is biased by a sufficient and a small DC bias B_{DC} values for comparison as listed in Table 2.1. The B_{DC} addition increases the electrical power dissipation and reduces the clipping noise as shown in Fig. 2.9. The effect of clipping noise is negligible when a sufficient B_{DC} values is used. For a given BER, the required $E_{b(elec)}/N_0$ is approximately equal to that of the bipolar signal plus the DC bias level in dB [108, 116] .

As the OFDM signals have high PAPR peaks, the signals have to be bias to an appropriate level to fit the linear dynamic range of the light source. Otherwise, the signal is clipped by the front-ends devices and distorted due to clipping noise which results in BER performance degradation as shown in Fig. 2.9.

The DCO-OFDM signal must be real and positive values to modulate the intensity of the light source of the IM/DD based VLC system. Real-valued signal is obtained by imposing Hermitian symmetry on the frequency domain signal [117]. The useful bandwidth of DCO-OFDM is limited to the upper side band (USB) whereas the lower side band (LSB) occupied by the Hermitian symmetry. The USB conveys the useful information and the LSB is redundant. The DCO-OFDM uses orthogonal subcarriers at different frequencies to convey the information bits. This means that, the orthogonality is guaranteed by transmitting the DCO-OFDM symbols with equal subcarrier spacing. Therefore, N subcarriers are evenly divided across the frequency range from $-\frac{1}{2T_s}$ to $\frac{1}{2T_s}$, where $T_s = \frac{1}{f_s}$, is the signal sampling period. The spectral efficiency of DCO-OFDM with a constant loading of modulation format assumption can be defined as
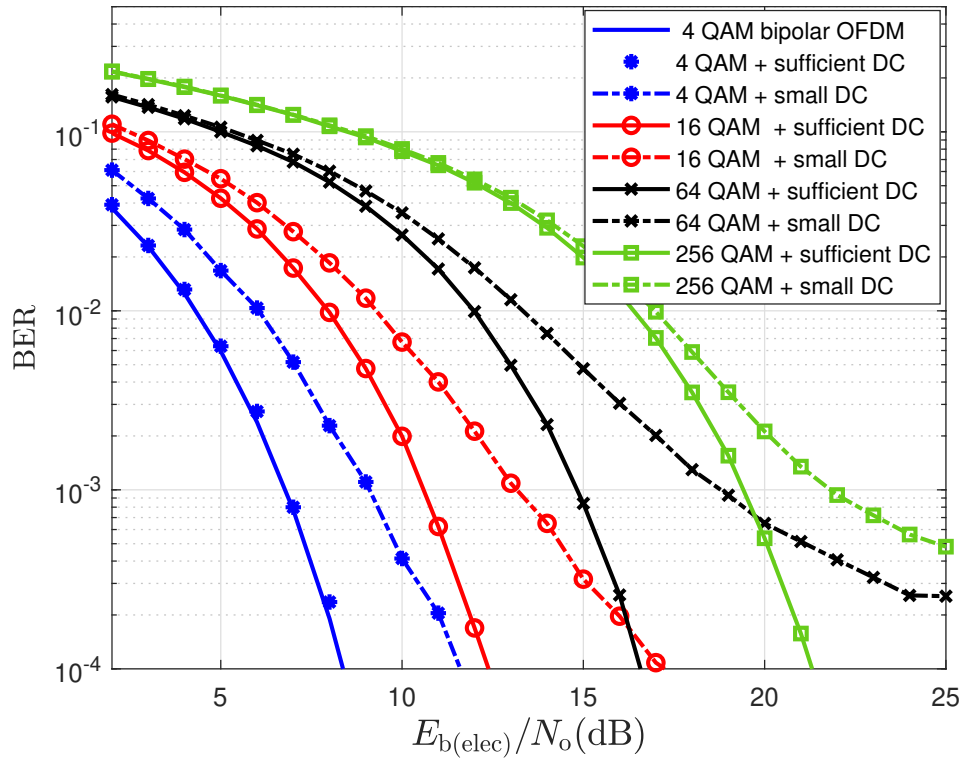
Figure 2.9: *BER performance of DCO-OFDM with sufficient and smaller DC bias values listed in Table. 2.1, using [4, 16, 64, 256] QAM modulation orders over AWGN channel.*

[117]:

$$\eta_{\text{DCO}} = \frac{\frac{\text{Number of bits within DCO-OFDM frame}}{\text{Duration of the frame}}}{\text{Available bandwidth}} \quad \text{bits/s/Hz} \tag{2.30}$$

Which can be written as follows:

$$\eta_{\text{DCO}} = \frac{\frac{\frac{N-2}{2}\log_2(M)}{(N+N_{\text{CP}})T_{\text{s}}}}{B} \quad \text{bits/s/Hz} \tag{2.31}$$

where N is the IFFT/FFT length, M is the constellation size and N_{CP} is CP length. The USB available system bandwidth, B, is assumed to be $B = \frac{f_{\text{s}}}{2}$ and $T_{\text{s}} = \frac{1}{f_{\text{s}}}$ where f_{s} is the sampling

frequency and $f_{\rm s} = 2B$ for simplicity. Therefore, the spectral efficiency can be given by:

$$\eta_{\rm DCO} = \frac{\frac{N-2}{2} \log_2{(M)} \times f_{\rm s}}{B(N + N_{\rm CP})}$$

$$(2.32)$$

$$= \frac{\frac{N-2}{2} \log_2{(M)} \times 2B}{B(N + N_{\rm CP})} \quad \text{bits/s/Hz}$$

Therefore, the spectral efficiency of DCO-OFDM can be given by:

$$\eta_{\rm DCO} = \frac{(N-2) \log_2{(M)}}{(N + N_{\rm CP})} \quad \text{bits/s/Hz} \qquad (2.33)$$

For large DCO-OFDM frame length, N, the spectral efficiency of the DCO-OFDM in (2.33), can be approximated to the following:

$$\eta_{\rm DCO} \approx \log_2(M) \quad \text{bits/s/Hz} \qquad (2.34)$$

The time-domain signal, $x(t)$, of the real-valued bipolar OFDM follows Gaussian distribution for large $N \geq 64$, with zero mean and variance σ_x^2, where σ_x is the standard deviation of $x(t)$ [108]. The average power of an OFDM frame is given as:

$$P_{\rm avg} = {\rm E}[x^2(t)]$$

$$= \sigma_x^2$$

$$(2.35)$$

Therefore, the energy per bit can be denoted as follows:

$$E_{\rm b} = \frac{\text{Average power of the OFDM frame} \times \text{Duration of the frame}}{\text{Total number of bits within the frame}}. \qquad (2.36)$$

Assuming constant constellation size, M, this can be written as:

$$E_{\rm b} = \frac{\sigma_x^2 N T_s}{\frac{N-2}{2} \log_2(M)}. \qquad (2.37)$$

Since $T_{\mathrm{s}} = 1/f_{\mathrm{s}}$ and $f_{\mathrm{s}} \geq 2B$ for large value of N, the energy per bit can be defined as:

$$E_{\mathrm{b}} = \frac{\sigma_x^2 N \frac{1}{f_s}}{\frac{N-2}{2} \log_2(M)},$$

$$= \frac{\sigma_x^2 N}{\frac{N-2}{2} \cdot 2B \log_2(M)}, \tag{2.38}$$

$$\approx \frac{\sigma_x^2}{B \log_2(M)}.$$

From (2.38), the SNR per bit can be given by:

$$\frac{E_{\mathrm{b}}}{N_{\mathrm{o}}} = \frac{\sigma_x^2}{B N_{\mathrm{o}} \log_2(M)},$$
$$= \frac{\sigma_x^2}{\sigma_n^2 \log_2(M)}. \tag{2.39}$$

where N_{o} is the single sided power spectral density (PSD) of the aAWGN and σ_n^2 is the noise variance at the receiver.

A suitable DC bias B_{DC} is required to convert $x(t)$ to unipolar signal and to avoid the nonlinearity distortion. However, this required a very high B_{DC} as the DCO-OFDM inherently have high PAPR. If a large B_{DC} is added to the signal, the optical energy-per-bit to the single sided noise power $E_{b(opt)}/N_0$ becomes very large which makes DCO-OFDM energy inefficient technique. Sufficient B_{DC} value is used instead of large DC bias as shown in Fig. 2.8 and Table. 2.1 to avoid large clipping levels as it is unpractical to convert all negative values to positive ones, which means clipping is practically unavoidable and can only be minimised by PAPR reduction techniques employment [116].

2.6.2.2 ACO-OFDM

The principle of ACO-OFDM is to load the useful information QAM symbols on the odd subcarriers and set the even subcarriers to zeros. Following the system structures in block diagram in Fig. 2.6, the complex-valued odd subcarriers are converted to real-valued by imposing Her-

mitian symmetry $X[k] = X^*[N - k]$, for $k = 1, 2, \ldots N/2 - 1$. Thus, the frequency domain frame of ACO-OFDM is given by [106]:

$$X[k] = \left[0, X_1, 0, X_3 \ldots, X_{N/2-1}, 0, X_{N/2-1}^*, \ldots, X_1^* \right] \tag{2.40}$$

where N is the length of the ACO-OFDM frame. $X[0]$ and $X[N/2]$ are set to zero. $X[k]$ in (2.40) is the input of IFFT which translates the frequency domain signal $X[k]$ to discrete time-domain waveform $x[n]$ which can be expressed by:

$$x[n] = \frac{1}{\sqrt{N}} \sum_{k=0}^{N-1} X[k]\, e^{j2\pi \frac{kn}{N}}; \qquad 0 \leq n \leq N - 1 \tag{2.41}$$

Skipping even subcarriers creates a symmetry in the time-domain signal, $x[n]$, which allows clipping the negative samples of ACO-OFDM signal without the need of DC bias to achieve unipolar samples. This symmetry is given in (2.44) which can be achieved by loading the modulated symbols into the odd subcarriers then clip the signal $x[n]$ as shown in (2.45) without loosing any useful information as the clipping noise falls on the even subcarriers only [102,116]. The IFFT output is real-valued time-domain baseband waveform of the ACO-OFDM which is used to modulate the light source intensity. The symmetry property can be proven from (2.41) as follows [102]:

$$
\begin{aligned}
x[n] &= \frac{1}{\sqrt{N}} \sum_{k=0}^{N-1} X[k]\, e^{j2\pi \frac{kn}{N}} \\
x\left[n + \frac{N}{2} \right] &= \frac{1}{\sqrt{N}} \sum_{k=0}^{N-1} X[k]\, e^{\frac{j2\pi(n + \frac{N}{2})k}{N}} \\
&= \frac{1}{\sqrt{N}} \sum_{k=0}^{N-1} X[k]\, e^{\frac{j2\pi kn}{N}}\, e^{j\pi k}.
\end{aligned} \tag{2.42}
$$

By selecting and modulating the even subcarriers only, the time-domain signal can be written as:

$$x\left[n + \frac{N}{2} \right] = -x[n] \tag{2.43}$$

However, loading the complex-valued QAM symbols onto the odd subcarriers only, the obtained symmetry can be given by:

$$\left[n + \frac{N}{2} \right] = x[n] \tag{2.44}$$

37

Clipping the negative peaks of the time-domain signal of ACO-OFDM is represented by the following [118]:

$$x_c[n] = \frac{1}{2}\big(x[n] + |x[n]|\big) \tag{2.45}$$

The zero level clipping is distortion-less as the clipping noise affects only the even subcarriers which are not carrying any useful information. The resulting signals in (2.41), (2.44) and (2.45) are shown in Fig. 2.10, where the same samples are illustrated in (b) and (c).
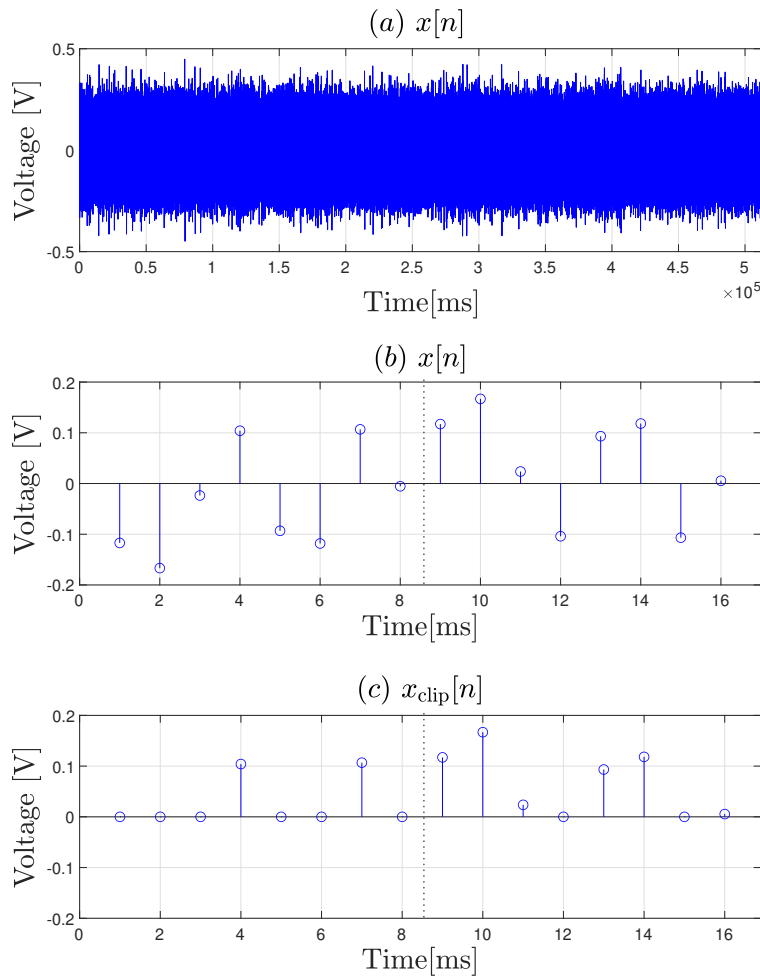
Figure 2.10: *(a) ACO-OFDM discrete time-domain signal. (b) Symmetric ACO-OFDM time-domain samples. (c) Clipped symmetric ACO-OFDM time-domain samples. (b) and (c) are the same samples before and after clipping at zero level respectively.*
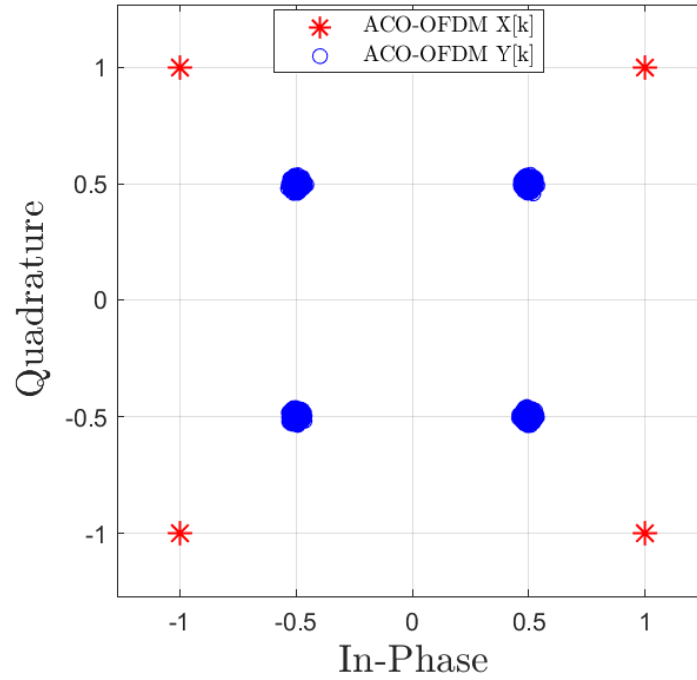
Figure 2.11: *4-QAM ACO-OFDM constellation points illustration, $X[k]$ at the transmitter and $Y[k]$ at the receiver.*

Clipping the negative peaks of $x[n]$ results in amplitude reduction by exactly 50% as shown by the constellation diagram in Fig. 2.11. This means that, half of the signal power in ACO-OFDM is lost due to negative peaks clipping and 3 dB penalty should be applied to its SNR when compared with bipolar OFDM [102, 108]. The BER performance of ACO-OFDM is plotted in Fig. 2.12. This shows the ACO-OFDM requires 3 dB more power than the same bipolar OFDM QAM size to achieve the same BER performance. At the receiver side, the received signal is demodulation and the information can be recovered from the odd subcarriers after applying FFT on the received symbols whereas the even subcarriers are discarded [108]. Re-scaling the odd subcarriers carrying information by a factor of 2 can be applied after FFT process to compensate the energy loss due to the zero level clipping.

In ACO-OFDM, half of the active subcarriers are used to carry information representing the odd subcarriers whereas the even subcarriers are set to zero. Therefore, the subcarriers carrying useful data is only $N/4$ independent unipolar subcarriers. As results, the spectral efficiency of
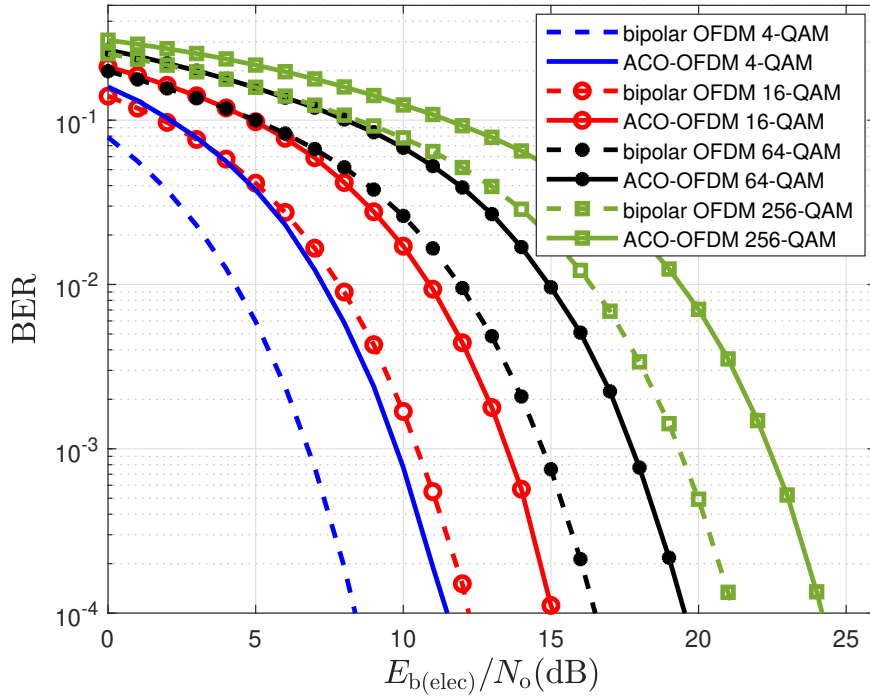
Figure 2.12: *BER Comparison of ACO-OFDM and bipolar OFDM over flat channel using [4, 16, 64, 256] QAM levels.*

ACO-OFDM system can be defined using (2.30) as follows:

$$\eta_{\text{ACO}} = \frac{\frac{(N-2)}{4}\log_2(M)}{\frac{(N+N_{\text{CP}})T_{\text{s}}}{B}} \qquad \text{bits/s/Hz} \qquad (2.46)$$

For large ACO-OFDM frame length, N, the available system bandwidth is assumed to be $B = \frac{f_{\text{s}}}{2}$ and $T_{\text{s}} = \frac{1}{f_{\text{s}}}$ where f_{s} is the sampling frequency. Therefore, the spectral efficiency of ACO-OFDM can be rewritten as follows:

$$\eta_{\text{ACO}} = \frac{\frac{(N-2)}{4}\log_2(M) \times f_{\text{s}}}{\frac{f_{\text{s}}}{2}(N+N_{\text{CP}})} \qquad \text{bits/s/Hz}$$

$$(2.47)$$

$$= \frac{\frac{(N-2)}{2}\log_2(M)}{(N+N_{\text{CP}})} \qquad \text{bits/s/Hz}$$

Therefore, the spectral efficiency of ACO-OFDM, η_{ACO}, is given by:

$$\eta_{\text{ACO}} = \frac{(N-2)\log_2(M)}{2(N + N_{\text{CP}})} \quad \text{bits/s/Hz} \tag{2.48}$$

The length of CP is often selected to be around 5 samples and constant M constellation size loading is assumed for simplicity. Therefore, the η_{ACO} in (2.48) can be approximated to the following:

$$\eta_{\text{ACO}} \approx \frac{1}{2}\log_2 M \quad \text{bits/s/Hz} \tag{2.49}$$

The statistics of real-valued ACO-OFDM time-domain signal, $x_{\text{ACO}}(t)$, follows a truncated Gaussian distribution [102]. Due to ACO-OFDM's symmetry, negative peaks can be removed by clipping at zero level without signal distortion. This clipping leads to a factor of 2 requirement that is introduced at the transmitter to re-scale the ACO-OFDM unipolar signal $x_{\text{clip}}(t)$ which induces an overall SNR penalty of 3 dB. ACO-OFDM technique is power efficient because no DC bias is required when compared with DCO-OFDM as the DC biasing increases the dissipated electrical and optical power at the transmitter substantially [102].

2.6.2.3 PAM-DMT

In PAM-DMT, the imaginary components of the complex-valued PAM symbols are modulated and, the real parts are not used and set to zeros. This results in $X[k] = \jmath B_{\text{PAM}}[k]$, where $B_{\text{PAM}}[k]$ is the M-PAM symbols carrying useful data that are loaded on the imaginary components where $k = 1, 2, \ldots, N/2 - 1$ and $N = 2(N_{\text{subs}} + 1)$ where N_{subs} is the active subcarriers carrying information [33]. A VLC system optical source is modulated by a real-valued baseband waveform which means that the time-domain signal of PAM-DMT must be real and positive. The real-valued time-domain signal is achieved by imposing a Hermitian symmetry on the PAM mapped symbols in the frequency domain which is given by: $X[k] = X^*[N/2 - k]$, where X^* indicates the conjugate of X and $X[0] = X[N/2] = 0$. The PAM-DMT frame in the frequency domain with the Hermitian symmetry is given as follows:

$$X_{\text{H}} = \left[0, X_1, \ldots, X_{N/2-1}, 0, X^*_{N/2-1}, \ldots, X^*_1\right] \tag{2.50}$$

Applying IFFT operation of size N to the frequency domain signal results in corresponding

41

discrete time-domain signal $x[n]$. This can be expressed as follows [33, 102]:

$$x[n] = \frac{1}{\sqrt{N}} \sum_{k=0}^{N-1} X[k]\, e^{j2\pi k \frac{n}{N}} \qquad (2.51)$$

where $n = 0, 1, 2, \ldots, N-1$. This is can be rewritten by:

$$x[n] = \frac{1}{\sqrt{N}} \sum_{k=0}^{N-1} X[k] \left(\cos 2\pi k \frac{n}{N} + j \sin 2\pi k \frac{n}{N} \right) \qquad (2.52)$$

By selecting the imaginary part of the time-domain signal the following is obtained:

$$x[n] = \frac{-2}{\sqrt{N}} \sum_{k=0}^{N/2-1} jX[k] \sin \left(2\pi k \frac{n}{N} \right)$$

$$\qquad (2.53)$$

$$= \frac{-2}{\sqrt{N}} \sum_{k=1}^{N/2-1} B_{\text{PAM}}[k] \sin \left(2\pi k \frac{n}{N} \right)$$

where $B_{\text{PAM}}[k]$ is the M-PAM modulated symbol that is loaded on the imaginary parts of $X[k]$. The time-domain waveform follows an anti-symmetry property which can be visualised in Fig. 5.1. The anti-symmetry, $x[n] = -x[N-n]$, if N is even this means that $|x[n]| = |x[N-n]|$. Therefore, the clipping of the negative peaks in the time-domain PAM-DMT signal $x[n]$ does not affect the useful information as the same information are loaded on the positive components of the second half of the waveform. This means that zero level clipping distortion only affects the real components of the subcarriers, and the useful data can be recovered from the imaginary components as shown in Fig. 2.13 [33].

In PAM-DMT system, the bipolar signal is clipped at zero level to convert the bipolar signal into a unipolar one. Therefore, the DC bias is not required for this purpose which decreases the electrical and optical power dissipation. Thus, this makes PAM-DMT more power efficient when compared to DCO-OFDM. However, a minimum DC bias is still required due to the turn on voltage of the used optical light source. In comparison with bipolar OFDM at an appropriate constellation format, PAM-DMT system has 3 dB fixed penalty as half of the power is lost due to clipping at zero level. In addition, the PAM-DMT technique is more attractive than the ACO-OFDM since all of the subcarriers in PAM-DMT are used to carry information. Hence,
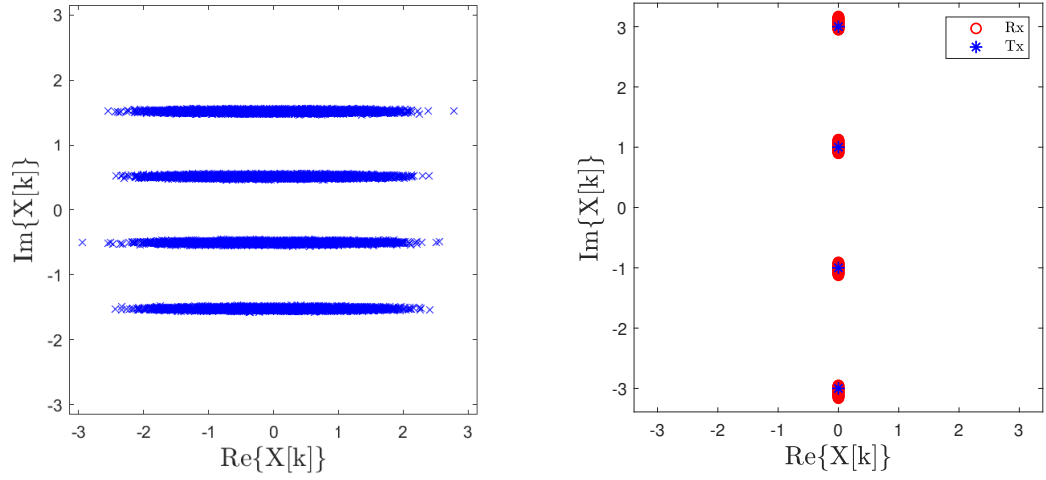
(a) *Real components of clipped PAM-DMT wave-form.*

(b) T_x *and* R_x *imaginary components of clipped PAM-DMT waveform.*

Figure 2.13: *Clipped PAM-DMT waveforms.*

the PAM-DMT performance can be optimised by employing bit and power loading techniques to be optimally adapted to the frequency response of the channel. The spectral efficiency of PAM-DMT is similar to that of DCO-OFDM in (2.33), and can be given by:

$$\eta_{\text{PAM}-\text{DMT}} = \frac{(N-2)\log_2(M)}{(N+N_{\text{CP}})} \quad \text{bits/s/Hz} \tag{2.54}$$

This can be approximated for large PAM-DMT frame length, N, by the following:

$$\eta_{\text{PAM}-\text{DMT}} \approx \log_2(M) \quad \text{bits/s/Hz} \tag{2.55}$$

where M denotes the constellation order of M-PAM modulation. It should be noted that the BER performance of M-PAM has to be compared to that of M^2-QAM. This makes the spectral efficiency of PAM-DMT comparable to that of ACO-OFDM at the same BER performance.

2.6.2.4 Other MCM Techniques

A number of MCM modulation approaches exist to obtain unipolar for IM/DD systems, that can provide an energy efficient alternatives to DCO-OFDM. In addition to the aforementioned techniques, this include the following techniques:
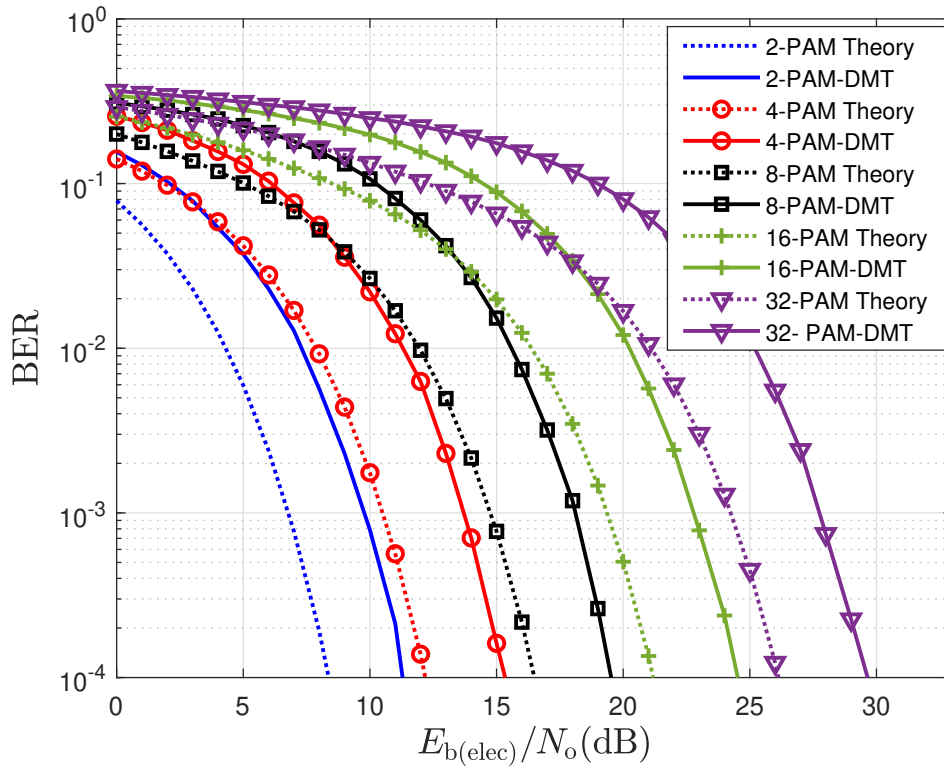
Figure 2.14: *BER Comparison of PAM-DMT and theoretical M-PAM over flat channel using [2, 4, 8, 16 and 32]-PAM levels.*

- U-OFDM and **Flip-** OFDM:

U-OFDM and Flip-OFDM were proposed in [31] and [32] respectively. The concept and the performance of both systems are identical. The time-domain signal is obtained in a similar manner as in DCO-OFDM. Then to achieve the unipolar signal, the time-domain signal is divided into two blocks: a positive block and a negative one. In the positive block, the original signal frame is used and the negative samples are set to zero. In the negative block, the original signal frame is multiplied by -1, to switch the frame signs then set all the negative samples to zero. This processes result in unipolar signal containing all the positive and negative samples of frame in the time domain. Each block is transmitted separately. Increasing the number of samples in the signal frame decreases the spectral efficiency of these two techniques. At the receiver side, the original signal is recovered by subtracting the negative block from the positive block which results in doubling the noise at every resulting sample. Therefore, a 3 dB power penalty is introduced to the system's SNR when compared with bipolar OFDM at appropriate constellation

format. This indicates that the spectral efficiency of U-OFDM and Flip-OFDM is similar to that of ACO-OFDM and PAM-DMT at appropriate constellation size which is half of the spectral efficiency of DCO-OFDM due to the imposed restrictions on their frame structures [31, 32, 102].

- **Enhanced unipolar orthogonal frequency division multiplexing** (eU-OFDM): the concept of eU-OFDM is to form a single time domain eU-OFDM frame by superimposing multiple U-OFDM time-domain streams. The superimposing process at the transmitter and demodulation process at the receiver are detailed in [119]. eU-OFDM technique increases the spectral efficiency of U-OFDM to approach that of DCO-OFDM without the need DC biasing, apart from the turn-on requirement. Thus, the technique avoids energy losses due to the biasing of the light source. eU-OFDM scheme achieves significant saving in terms of electrical and optical power dissipation at the cost of increasing computational complexity in the modulation and demodulation processes [119].

- **Superposition modulation techniques based on PAM-DMT**:

  The superimposed modulation techniques are rely on the frame structure of PAM-DMT to superimpose multiple inherent unipolar time-domain signal streams at different modulation depths that used to modulate the light source. The modulation depth, D, is the number of superimposed layers of data streams. Enhanced pulse-amplitude modulated discrete multitone modulation (ePAM-DMT) was proposed in [120], to achieve equivalent spectral efficiency of DCO-OFDM with lower energy requirement. The concept of ePAM-DMT is to design a hierarchy frame that converts all the inter-stream interference into the real part of the subcarriers to avoid signal distortion and the data can be transmitted and recovered using the imaginary components only. The ePAM-DMT frame generation starts with a PAM-DMT frame at depth-1 and another depth is superimposed and so on. Procedure of this technique is detailed in [120]. The spectral efficiency of this scheme is approximately the same to that of DCO-OFDM as the optimal combinations of constellation format at each stream depth and their relative scaling factors have been determined and applied at different spectral efficiencies. However, the ePAM-DMT suffers from high PAPR values and optical power dissipation.

  Another superposition modulation technique based on PAM-DMT is augmented spectral efficiency discrete multitone (ASE-DMT) that was proposed in [121]. ASE-DMT make use of most available subcarriers in the OFDM frame. The superimposed waveform gen-

eration starts with conventional PAM-DMT at first depth. However, selective loading of the imaginary and real components of the subcarriers is employed unlike conventional PAM-DMT. Higher levels depths can only be superimposed on the first depth stream if the data symbols in frequency domain are loaded on the real components of the subcarriers. The superimposing process is arranged in the frequency domain for each depth. After generating all the depths, Hermitian symmetry is imposed into each depth stream to guarantee a real-valued time-domain waveform that is obtained by IFFT operation. This is followed by zero level clipping and CP addition. The zero level in the first is distortion less to the information at the same depth because the all the clipping distortion fall into the real components of the subcarriers. The overall waveform of the ASE-DMT is generated by superimposing the waveforms of all depths. The ASE-DMT technique avoids the losses of spectral and energy efficiency in ePAM-DMT and close the gap to the spectral efficiency of DCO-OFDM at the cost of doubling the computational complexity. This scheme increases the undesirable high PAPR values which limits the system performance due to the nonlinearity distortion and clipping noise.

- **Superposition modulation techniques based on ACO-OFDM**:

Many superposition modulation techniques based on conventional ACO-OFDM have been proposed for VLC system based IM/DD mechanism. This includes asymmetrically DC-biased optical orthogonal frequency division multiplexing (ADO-OFDM) [122]. The ADO-OFDM uses the odd subcarriers to load conventional ACO-OFDM and even subcarriers to load DCO-OFDM. A transmitter is developed to transmit both ACO-OFDM and DCO-OFDM waveforms and the data can be recovered at the receiver using conventional methods. The clipping distortion of the odd-indexed subcarriers falls on the even-indexed subcarriers which can be estimated and cancelled at the receiver. This results in a 3 dB penalty to the system SNR. Similar approach is hybrid asymmetrical clipped orthogonal frequency division multiplexing (HACO-OFDM) [123]. In HACO-OFDM, ACO-OFDM is loaded on the odd-indexed subcarriers and PAM-DMT is loaded on the even-indexed subcarriers to improve the spectral efficiency of U-OFDM. At the receiver, the loaded ACO-OFDM subcarriers are demodulated first to allow for the clipping distortion to be estimated followed by the loaded PAM-DMT subcarriers which are affected with minimal distortion from the clipping noise of the ACO-OFDM subcarriers. The real components of the even-indexed subcarriers remain unused which leads to spectral efficiency loss comparing with DCO-OFDM.

Other ACO-OFDM superposition approaches include spectral and energy efficient optical orthogonal frequency division multiplexing (SEE-OFDM) in [124] and enhanced asymmetrically clipped optical orthogonal frequency division multiplexing (eACO-OFDM) [4] where both techniques use similar principles. A similar concept was proposed in [125] under the term layered asymmetrically clipped optical orthogonal frequency division multiplexing (LACO-OFDM).

2.7 Summary

A detailed review of the state of the art of the VLC has been given in this chapter. The review covers the VLC front-end devices, channel modelling, link impairments and employed digital signal processing (DSP) techniques to overcome those impairments and improve the system performance. In addition, different modulation techniques are discussed with a focus on O-OFDM techniques that are considered and implemented in this thesis. The performance and inherit constraints of the O-OFDM modulation techniques are also included in this chapter.

Chapter 3
Peak-to-Average Power Ratio

3.1 Introduction

This chapter presents the principles of PAPR challenge in VLC system, PAPR evaluation in O-OFDM based systems and its effect on the transmitted signal. In addition, the existing PAPR reduction techniques that are proposed for OFDM based systems are discussed. Detail description of PA technique is presented including its implementation in O-OFDM and PAPR reduction gain.

The O-OFDM signal in the time domain is the sum of a number of independent and identically distributed samples, follows the Gaussian distributions according to the central limit theorem (CLT) [126]. The CLT theorem holds for any practical frame length $N \geq 64$. The O-OFDM frame length, N, includes Hermitian symmetry that introduces some form of correlation into the frame but the distribution of the time-domain waveform, $x(t)$, is still Gaussian for large N. This implies the possibility of coherent addition of individual subcarriers in the time domain of the O-OFDM frame which results in high peaks. These peaks are often measured with respects to the average electrical power of the time-domain signal via the metric of electrical PAPR [26]. The PAPR values imply the ratio of the maximum instantaneous power to the average power of the O-OFDM waveform.

The high PAPR peaks are undesirable in OWC system due to the limited operating dynamic range of the front-end devices. As a result, it is impossible to accommodate all signal swings within the limited linear dynamic region of the light source without clipping the signal at lower and/or upper level. On the other hand, the light source would be operating at its saturation region to contain all the signal swing which is undesirable as well. Therefore, the PAPR peaks will cause the optical source to operate outside its linear dynamic region to contain full amplitude swings of the signal. In addition, signal clipping at lower and/or upper level clipping is imposed by the frond-end devices of the system. This in turn restricts the average transmitted optical power and induces distortion, and clipping noise to the transmitted signal. This

results in SNR reduction and system performance degradation [26]. To avoid the aforementioned undesirable affect of the inherent high PAPR peaks of the O-OFDM system, the high PAPR values must be reduced to benefit from the full linear dynamic range of the light source. Various solutions have been proposed in the literature to address the PAPR challenge for the RF and OWC systems. The most common and effective solutions and techniques will be included and discussed in this chapter.

3.2 PAPR of Optical OFDM Systems

There are several used metrics to measure the high peaks of a transmitted signal including, cubic metric (CM) in [127], instantaneous-to-average power ratio (IAPR) in [128], peak-to-mean envelope power ratio (PMEPR) in [129] and the commonly used PAPR [26]. PAPR metric is a widely used metric to measure high power peaks of a time-domain signal, and will be used throughout this work. The PAPR is the ratio between the maximum power and the average power of the real-valued discrete time-domain signal $x[n]$ [130]. To sufficiently capture all the signal peaks across the O-OFDM frame, the the frequency domain signal is over-sampled using zero padding process. The adequate oversampling factor is $L = 4$ [26]. Thus, the time-domain frame length, N, becomes NL. Therefore, the PAPR of the real-valued discrete time-domain O-OFDM signal is defined as:

$$\text{PAPR} \triangleq \frac{\max\limits_{0 \leq n \leq NL - 1} |x[n]|^2}{\text{E}[|x[n]|^2]} \tag{3.1}$$

where $\text{E}[\cdot]$ denotes the statistical expectation. The PAPR of an O-OFDM signal increases as the signal length, N, increases. The theoretical maximum possible PAPR value of an O-OFDM signal is $10 \log_{10}(N_{\text{subs}})$ in dB which is excessively high, where N_{subs} is the number of active subcarriers. However, such a high value is a rarely reached [131]. An effective statistical way to characterising PAPR is the complementary cumulative distribution function (CCDF). The CCDF is a widely used measure for PAPR reduction and defined as the probability that the O-OFDM frame PAPR exceeds a predefined value, PAPR_0, which can be expressed as the following [131]:

$$P_{\text{PAPR}} = \text{Pr}\{\text{PAPR} \geq \text{PAPR}_0\} \tag{3.2}$$

where P_{PAPR} is the probability that PAPR exceeds a particular threshold of PAPR_0. Illustration of PAPR of a MCM technique is shown in Fig. 3.1 and Fig. 3.4 in this chapter. The high PAPR peaks of an O-OFDM frame appear when individual subcarriers added up coherently in the time domain and is dependant on the time-domain frame length [34]. This is illustrated by using 4-QM conventional O-OFDM with varying the number of subcarriers to form different frame lengths, $N = [64, 256, 1024, 2048]$ for the investigation. In addition, the oversampling of the signal will be included in the frame length to obtain an accurate PAPR. The PAPR is measured by CCDF means and shown in Fig. 3.1. The PAPR values are independent from the QAM constellation size used, hence, 4-QAM is used for simplicity.
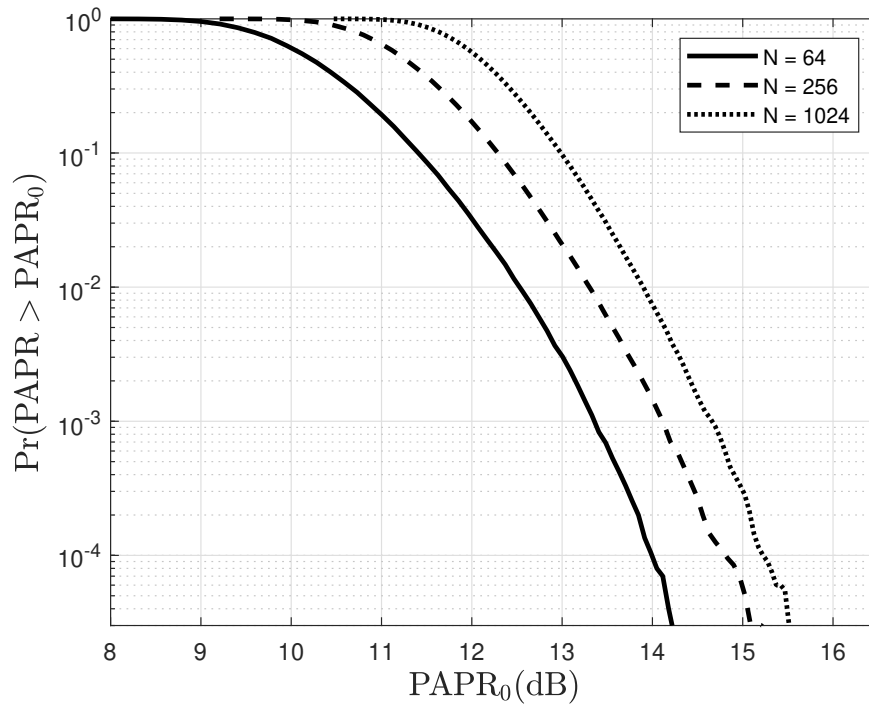
Figure 3.1: *PAPR CCDF plot for 4-QAM O-OFDM using N = [64, 256 and 1024] subcarriers and up-sampling factor L = 4 to demonstrate the effect of N size on the system PAPR.*

3.3 PAPR Reduction Techniques for Optical OFDM based Systems

The O-OFDM waveform has large PAPR peaks that would drive the optical driver at the transmitter into its power saturation point, resulting in distortion among the subcarriers, and cor-

rupting the signal spectrum, hence, degrading the system BER performance. To avoid such a problem, the average power of the signal may be reduced which reduces the SNR and degrades the system performance [37]. Therefore, the high PAPR issue is preferable to be solved rather than reducing the average optical power. Many solutions have been proposed in the literature to address the PAPR challenge.

The electrical PAPR reduction techniques are classified into distortion and distortion-less techniques. The distortion techniques are the ones distort the signal to achieve PAPR reduction at the expense of system performance degradation. This include: clipping and filtering [37–41], peak windowing [42], companding [43] and peak cancellation [44, 45]. On the other hand, the distortion-less techniques include multiple signalling and probabilistic techniques, and coding techniques. The multiple signalling and probabilistic techniques work in one of two ways. The first way is generate multiple permutations OFDM signal and select the signal with the lowest PAPR for transmission. The second way relies on modifying OFDM signal by introducing phase shifts, adding peak reduction carriers or modifying constellation points [37]. This includes: SLM [26, 46–49], PTS [39, 50–53], TI [54], TR [55], ACE [56, 57], constrained constellation shaping [58]. Coding techniques for PAPR reduction purposes in OFDM includes, linear block coding [59–61] and turbo coding [62–64].

Clipping is the simplest and most common used peak reduction technique. In signal clipping, any desired level of PAPR reduction gain can be attained, where part of the signal is clipped to fit the linear operating dynamic region of the light source. This is achieved at the cost of deteriorating the system BER performance [26, 47]. Another clipping method for optical network was proposed in [132] where the signal is clipped symmetrically then the clipping-noise-cancellation (CNC) algorithm is applied to mitigate the clipping noise effect. Classical SLM algorithm is another approach, where alternative sequences U carrying the same information are produced by multiplying the data vector by random phase sequences to change the PAPR proprieties. The data with lowest PAPR values is selected for transmission. The PAPR reduction gain increases when the number of phase sequences used increases. This method is limited by the spectral efficiency loss due to the number of side information that is transmitted with each data sequence for recovery [26, 47, 48]. Various methods based on SLM scheme is reported in [46, 133]. TI scheme uses correction method for PAPR reduction by remapping the original data that produces large PAPR peak into several new positions [47]. This method reduces the PAPR of the signal at the cost of complex transmitter, more signal power for trans-

mission and additional IFFT operations [47]. The PTS is another PAPR reduction technique that is used to partition the input OFDM data symbol into a subsets where these subsets are rotated with multiple factors. the modified subsets are then combined together again to generate a candidate data symbol and the candidate with the lowest PAPR value is selected for transmission. The PTS can achieve higher PAPR reduction gain when compared to SLM however PTS holds a higher computational complexity [134]. A Comparison of the PAPR reduction techniques is shown in Table. 3.1.

TR scheme is another method to reduce PAPR peaks which reserves subset of the transmitted subcarriers called peak reduction tones (PRT) for PAPR reduction [55]. The TR scheme requires optimised PRT position to perform efficiently and avoid performance degradation with non-optimal PRT position. The PRT position can be achieved with the iterative gradient algorithm (IGA). However, it is not straightforward to find the optimal PRT position and IGA requires long iteration times to converge which make the TR scheme with IGA is not suitable for real time implementation [55]. Pilot-assisted (PA) technique is an effective solution for PAPR reduction in O-OFDM systems [26]. PA technique is used to rotate the phase of data symbols block by a randomly generated pilot in order to avoid coherent addition of the subcarriers as much as possible. The pilot symbol's phase is chosen based on the SLM algorithm while the ML algorithm is used to recover the pilot phase at the receiver side [65]. Generalised details of the PA technique procedure and implementation for O-OFDM is included in this chapter. A Comparison of the PAPR reduction techniques is shown below in Table. 3.1.

Comparison Metrics					
Technique	**PAPR Gain**	**Complexity**	**BER Degradation**	**Side Information**	**Power Loss**
Clipping	Any desired	Low	Yes	No	Yes
Coding	≈ 3.5	High	No	Yes	Yes
PTS	≈ 3.5	High	No	Yes	No
SLM	≈ 2	High	No	Yes	No
PA	≈ 3	Low	No	No	No

Table 3.1: *PA in comparison with existing PAPR reduction techniques. Complexity refers to the computational complexity and PAPR gain is in dB.*

3.3.1 Pilot-Assisted PAPR Reduction Technique for Optical OFDM system
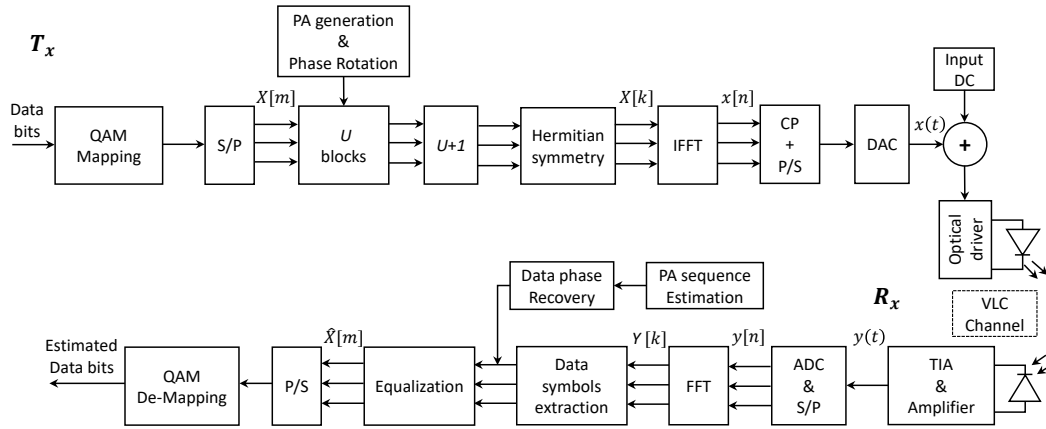
Figure 3.2: *Block diagram illustrating the pilot-assisted (PA) implementation in optical-OFDM system. S/P: serial-to-parallel converter, PA: pilot-assisted, U: number of data blocks with N_{subs}, U+1: U blocks with embedded PA symbol, CP: cyclic prefix addition, P/S: parallel-to-serial converter, DAC: digital-to-analogue converter, DC: direct current, TIA: transimpedance amplifier, ADC: analogue-to-digital converter.*

Pilot-assisted (PA) is an effective PAPR reduction technique for O-OFDM based system that was proposed in [26]. PA rotates the phase of individual subcarriers to avoid the possibility of them added up coherently in the time domain of the O-OFDM waveform. General implementation process of PA for O-OFDM is illustrated by the block diagram in Fig. 3.2.

O-OFDM system is affected by high PAPR peaks and to address the PAPR problem, the PA technique is applied as a high PAPR values reduction solution. The implementation process of PA for O-OFDM based VLC system is described in this section. Primarily to the PAPR reduction process, the incoming data bits are mapped into modulation formats such as M-QAM. The M-QAM symbols are formed into data carrying subcarriers (active subcarriers), $X[m]$, with length of N_{subs}, then grouped into clusters of U of data symbols to form X_m^u, $u = 1, 2, \ldots, U$. The data carrying frames are represented as: $X^u[m]$, where $m = 0, 1, \ldots, N_{\text{subs}} - 1$. Pilot sequence, X_p, with the same length of $X[m]$, amplitude $A_{\text{p}}[m]$ and phase $\theta_{\text{p}}[m]$ is generated and used to rotate the phase of block U then embedded with the data carrying subcarriers block, U, which becomes $\hat{U} = (U + 1)$ as shown n Fig. 3.3. The pilot symbol is represented as $X_{\text{p}}[m] = X^{U+1} = A_{\text{p}}[m]e^{j\theta_{\text{p}}[m]}$ [26] . The phase of the PA sequence is represented as θip; $i = 1, 2, \ldots, n_m$; $p = 1, 2, \ldots, P$, which is used to rotate the data carrying

symbols phase, θ_{iu}; $i = 1, 2, \ldots, n_m$; $u = 1, 2, \ldots, U$, to obtain the phase rotated signal X_{mp} as described in (3.3) [135].
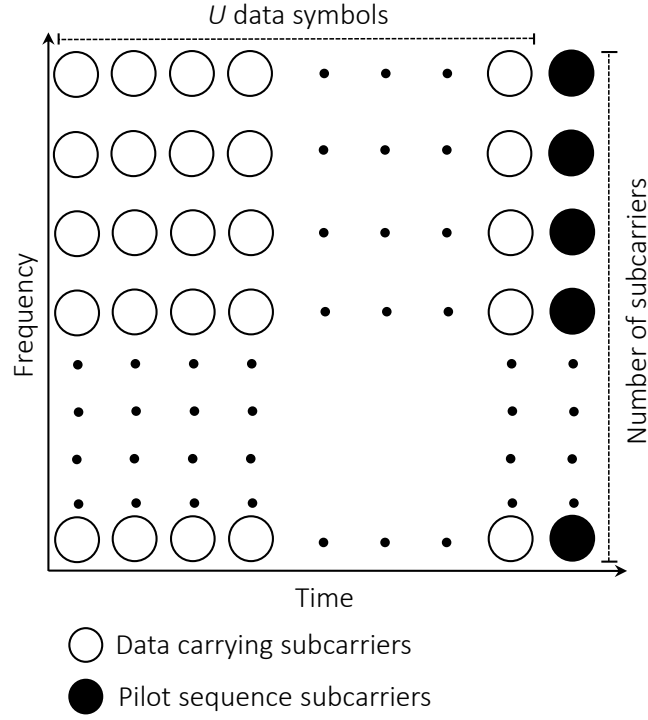
Figure 3.3: *An O-OFDM block of frames, $\hat{U}$, showing the data carrying subcarriers, N_{subs}, and pilot-assisted symbols.*

$$X_{mp} = \begin{pmatrix} a_{11}\big/\underline{\theta_{11} + \theta_{1p}} & \cdots & a_{1u}\big/\underline{\theta_{1u} + \theta_{1p}} & \cdots & a_{1U}\big/\underline{\theta_{1U} + \theta_{1p}} & 1\big/\underline{\theta_{1p}} \\ a_{21}\big/\underline{\theta_{21} + \theta_{2p}} & \cdots & a_{2u}\big/\underline{\theta_{2u} + \theta_{2p}} & \cdots & a_{2U}\big/\underline{\theta_{2U} + \theta_{2p}} & 1\big/\underline{\theta_{2p}} \\ \vdots & \vdots & \vdots & \vdots & \vdots & \vdots \\ a_{i1}\big/\underline{\theta_{i1} + \theta_{ip}} & \cdots & a_{iu}\big/\underline{\theta_{iu} + \theta_{ip}} & \cdots & a_{iU}\big/\underline{\theta_{iU} + \theta_{ip}} & 1\big/\underline{\theta_{ip}} \\ \vdots & \vdots & \vdots & \vdots & \vdots & \vdots \\ a_{n_m 1}\big/\underline{\theta_{n_m 1} + \theta_{n_m p}} & \cdots & a_{n_m u}\big/\underline{\theta_{n_m u} + \theta_{n_m p}} & \cdots & a_{n_m U}\big/\underline{\theta_{n_m U} + \theta_{n_M p}} & 1\big/\underline{\theta_{n_m p}} \end{pmatrix}$$

(3.3)

where a_{iu} is the QAM symbol amplitude, θ_{iu} is the phase of the ith subcarrier of the uth symbol and θ_{ip} is the phase of the ith pilot subcarrier of the pth pilot symbol sequence. For a given subcarrier m, the phase of each data entry $X^u[m]$, $u = 1, 2, \ldots, U$ and $m = 0, 1, \ldots, N_{\text{subs}} - 1$

is rotated by $\theta_\text{p}[m]$ while its amplitude is scaled by $A_\text{p}[m]$. The resulting signal is given by:

$$\hat{X}^u[m] = X^u[m] \times A_\text{p}[m]e^{j\theta_\text{p}[m]}. \tag{3.4}$$

The pilot phase, $\theta_\text{p}[m]$, could take any value between 0 and 2π. However, the pilot phase, $\theta_\text{p}[m]$, is set to 0 or π values only to maintain the original constellation of the input data QAM symbols, while the amplitude is constrained to unity in order to preserve the electrical power of the information signals. The implementation process of PA technique for PAPR reduction of O-OFDM system can be summarised as follows [26]:

- Group the QAM symbols into U blocks comprise of active subcarriers, N_subs, to obtain $X^u[m]$, where $u = 1, 2, \ldots, U$. and $m = 0, 1, \ldots, N_\text{subs} - 1$.

- Generate multiple iterations of pilot sequence candidates, R, with N_subs length, $X_\text{p}^r[m]$, where $r = 1, 2, \ldots, R$.

- Select the amplitude, $A_\text{p}[m]$, of the pilot sequence, $X_\text{p}^r[m]$, to be ± 1 only.

- Randomly set the pilot sequence phase $\theta_\text{p}[m]$ to 0 or π values only.

- Rotate the phase of the current block, U, by $\theta_\text{p}[m]$ of every pilot iteration r.

- Evaluate the PAPR_r of each iteration of $X_\text{p}^r[m]$ in the time domain using (3.1).

- Select the pilot iteration $X_\text{p}[m] = X_\text{p}^{\tilde{r}}[m]$ with the minimum PAPR value for PAPR reduction and transmission with the corresponding frames blocks U; where [35],

$$\tilde{r} = \underset{1 \leq r \leq R}{\text{argmin}} \, (\text{PAPR}_r) \tag{3.5}$$

- Embedding the pilot sequence $X_\text{p}^{\tilde{r}}[m]$ into the corresponding frames block, U, makes the number of frames per block $\hat{U} = (U + 1)$.

Due to the fact that the light sources of the VLC system transmit the data by an incoherent light intensity, the O-OFDM waveform are required to be real-valued and unipolar. Therefore, Hermitian symmetry is imposed into the data blocks, $X^{U+1}[m]$, while the unipolar waveform can be obtained by methods such as: DC bias, clipping at zero level, etc. The Hermitian symmetry, $X[m] = X^*[N/2 - m]$, is imposed into the data symbols in the frequency domain,

where X^* indicates the conjugate of X and $X[0] = X[N/2] = 0$. The O-OFDM frame in the frequency domain with the Hermitian symmetry is given by:

$$X_{\mathrm{H}}[k] = \left[0, X_1, \ldots, X_{N/2-1}, 0, X_{N/2-1}^*, \ldots, X_1^*\right]^{\mathrm{T}} \tag{3.6}$$

To capture all the signal peaks across the IFFT operation efficiently, zero padding is inserted into the frequency domain in (3.6). The optimum value for the oversampling factor, $L = 4$, [130]. Hence, (3.6) can be expressed by:

$$X[k] = \left[0, X[k], \underbrace{0, 0, \ldots, 0}_{\mathrm{N(L\text{-}1)/2}}, 0, \underbrace{0, 0, \ldots, 0}_{\mathrm{N(L\text{-}1)/2}}, X^*[NL - k]\right]^{\mathrm{T}} \tag{3.7}$$

where $N = 2(1 + N_{\mathrm{subs}})$ and N_{subs} is the number of active subcarriers in each O-OFDM frame.

This value of U is generally selected to obtain a good trade off between performance and the computational complexity as the PAPR increases as U increases. Furthermore, the number of iterations, R, is selected to an optimal value to achieve an effective PAPR reduction gain and low computational complexity [135]. An IFFT operation is applied into the frequency domain frames to obtain discrete time-domain corresponding frames, $x[n]$ followed by PAPR evaluation. The electrical PAPR of the time-domain frames is defined in (3.1). CP is not usually considered during the PAPR evaluation as it has negligible impact on the PAPR result. The parallel O-OFDM frames are then converted from parallel into a serial one followed by DAC to obtain the continuous time-domain signal $x(t)$ as shown by the system block diagram in Fig. 3.2. The PAPR reduction gain of the PA scheme of the time-domain signal of the O-OFDM is shown in Fig. 3.4.

At the receiver side, the incoming optical radiation is detected then converted into electrical current signal by the PD, followed by trans-impedance amplifier (TIA) that turns the current signal into a voltage corresponding one. This is followed by ADC to obtain a discrete time-domain signal $y^u[n]$. The signal, $y^u[n]$, is then converted back to parallel and FFT operation is applied in order to obtain a frequency domain signal $Y^u[k]$ as illustrated in the block diagram in Fig. 3.2. The redundant part (Hermitian symmetry) of the received frames blocks is discarded. Therefore, the received frequency domain signal can be given by the following:

$$Y^u[m] = H[m] \times \tilde{X}^u[m] \times +W[m]; \qquad u = 1, 2, \ldots, U + 1. \tag{3.8}$$
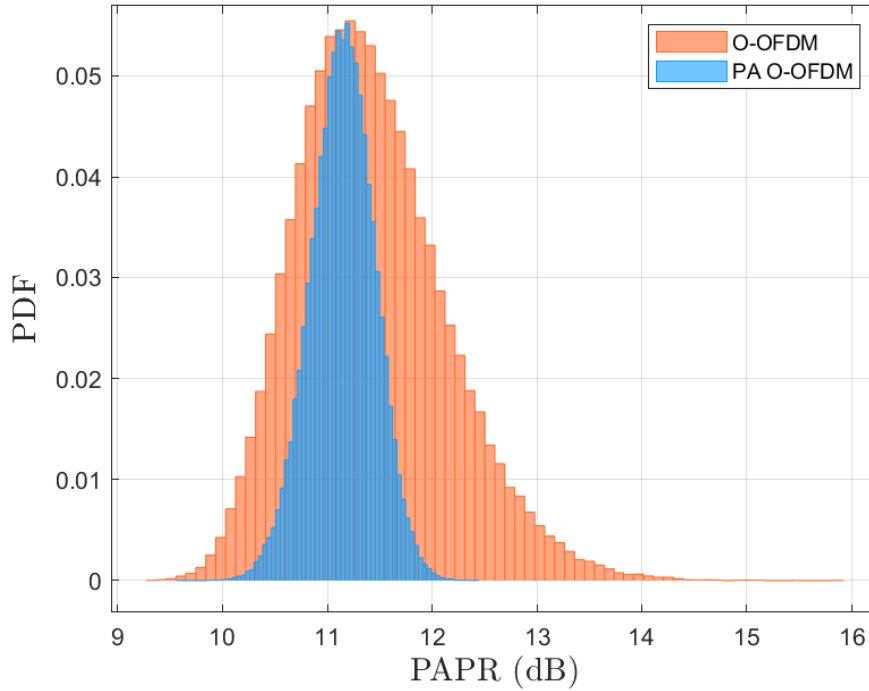
Figure 3.4: *PAPR distribution plot for 16-QAM O-OFDM with and without PAPR reduction using pilot-assisted with $N_\text{subs} = 127$ active subcarriers, $L = 4$, $N = 1024$ and $U = 5$. The mean and variance of O-OFDM signal without PAPR reduction are 11.3 dB and 0.51 dB respectively whereas it has a mean of 11.1 dB and a variance of 0.14 dB with PAPR reduction technique implemented.*

where $H[m]$ is the CIR at sample m, $\tilde{X}^u[m]$ is the transmitted signal at sample m, and $W[m]$ is the frequency domain estimated AWGN at sample m with zero mean and variance σ_w^2. The transmitted data symbols could be recovered by dividing every data samples m in $Y^u[m]$ by the received pilot samples in $Y^{u+1}[m]$ as follows [26]:

$$\hat{X}^u[m] = \frac{Y^u[m]}{Y^{U+1}[m]}; \qquad u = 1, 2, \ldots, U. \tag{3.9}$$

The received pilot signal at sample m, $Y^{U+1}[m] = H[m] \times \tilde{A}_\text{p}[m] e^{j\tilde{\theta}_\text{p}[m]}$, where the $\tilde{A}_\text{p}[m]$ and $\tilde{\theta}_\text{p}[m]$ are the received noise corrupted pilot samples amplitude and phase respectively. Thus, the extracted PA symbols are estimated using ML technique. The ML is an effective detection method to estimate the statistical parameter θ where the parameter values that are most likely to generate the observed data are chosen [65]. The estimation method of the corrupted pilot

58

sequence using the ML technique is described as follows [26]: the received PA sequences are extracted from the data blocks, then the corrupted phase $\hat{\theta}_{\mathrm{p}}[m]$ is estimated using ML technique to improve the data recovery. The estimate of the angle is taken between two values, ($\hat{\theta}_i = 0$ and π) that has the minimum Euclidean distance from the received pilot's phase $\tilde{\theta}_{\mathrm{p}}[m]$, The estimate argument is given by the following:

$$\hat{\theta}_{\mathrm{p}}[m] = \underset{1 \leq i \leq 2}{\operatorname{argmin}}[(\tilde{\theta}_{\mathrm{p}}[m] - \theta_{\mathrm{i}})^2] \tag{3.10}$$

The estimated pilot sequence becomes $\hat{X}_{\mathrm{p}}[m] = e^{j\hat{\theta}_{\mathrm{p}}[m]}$, which is equivalent to the following condition [26]:

$$\hat{X}_{\mathrm{p}}[m] = \begin{cases} +1, & \text{if} \quad \cos{(\tilde{\theta}_{\mathrm{p}}[m])} \geq 0 \\ -1, & \text{otherwise.} \end{cases} \tag{3.11}$$

Therefore, the transmitted data symbols can be estimated by the phase recovered pilot sequence symbols as [26]

$$\hat{X}^u[m] = \frac{Y^u[m]}{\hat{X}_{\mathrm{p}}[m]}; \qquad u = 1, 2, \ldots, U. \tag{3.12}$$
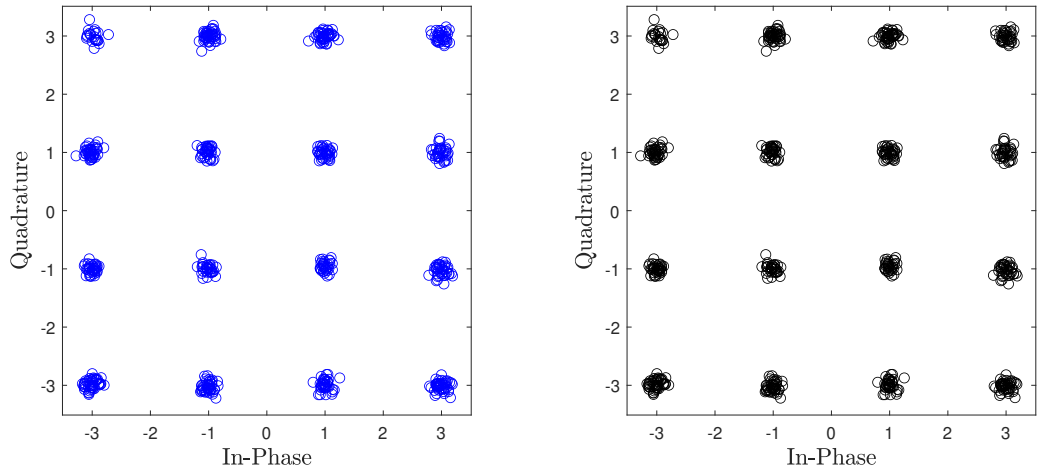
(a) *PA sequence estimation using ML algorithm* (b) *Using pre-knowledge of PA sequence*

Figure 3.5: *Constellation diagrams of 16-QAM O-OFDM with PAPR reduction using pilot-assisted with $N_{\mathrm{subs}} = 127$ active subcarriers, $L = 4$, $N = 1024$, $U = 5$ and at SNR = 22 dB. In (a) PA sequence is estimated using ML algorithm and in (b) pre-knowledge of PA sequence is used to recover the data.*

Finally, the estimated data symbols are mapped onto a QAM demodulator to obtain the binary bit streams from the estimated demodulated symbols. The received pilot amplitude, $\tilde{A}_{\mathrm{p}}[m]$, is constraint to unity. The constraint on the phase and amplitude of the pilot sequence at the transmitter side makes the estimation process by the ML algorithm suitable at the receiver side and helps to minimises the number of the estimate combinations that are needed to be searched for the pilot symbols sequence estimation [26]. The ML condition in (3.11) will estimate all the noise corrupted pilot phase, hence, the ML estimation result of the pilot sequence phase on a received data constellation diagram is shown in Fig. 3.5. This is compared with the same data constellation diagram where a pre-knowledge of the pilot phase is used to recover the data. The results show the effectiveness of the ML algorithm to correct all the pilot phase in the presence of noise thus, recover the phase of the rotated transmitted data correctly. This is achieved by simple ML decoder process to solve the ML criterion in (3.10), where only $N_{\mathrm{subs}}|\cdot|^2$ operations is required.
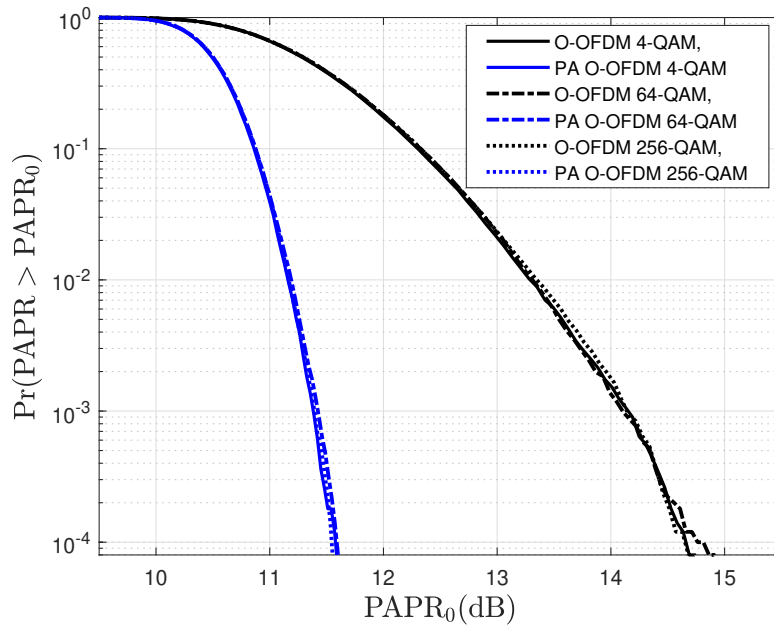
Figure 3.6: *PAPR CCDF plot for [4-64-256]-QAM O-OFDM with and without PAPR reduction using pilot-assisted with $N_{\mathrm{subs}} = 127$ active subcarriers, $L = 4$, $N = 1024$ and $U = 5$.*

The PAPR reduction capability of the PA technique in O-OFDM is shown in Fig. 3.4 as PAPR values distribution. This capability is affected by the number iterations R of pilot sequence

which means the more iterations used the higher the probability to achieve lower PAPR signal and this can be observed from Fig. 3.7. However, an optimum value of R is a practical approach because at higher number of R the PA PAPR reduction gain is limited. Hence, trade off between the PAPR reduction gain and the search complexity to find lower PAPR sequence phase. Moreover, the PAPR of the O-OFDM signal is independent from the constellation format used to modulate the data symbols as illustrated in Fig. 3.6. Therefore, the PA technique PAPR reduction gain is not affected by the used constellation size, hence, PA technique can be implemented with adaptive bit loading algorithm while achieving similar PAPR reduction gain.
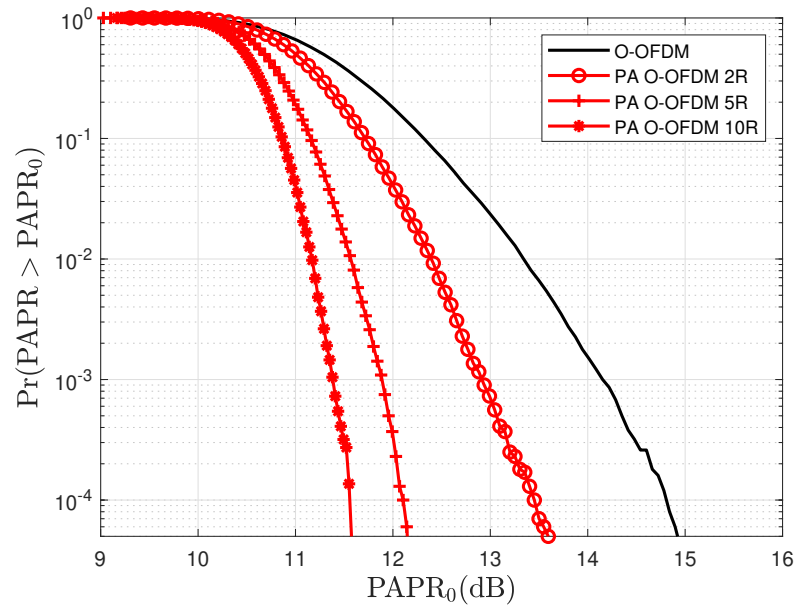
Figure 3.7: *PAPR CCDF plot for 16-QAM O-OFDM with and without PAPR reduction using pilot-assisted technique with $R = [2, 5, 10]$ iterations, $N_{\text{subs}} = 127$ active subcarriers, $L = 4$, $N = 1024$ and $U = 5$.*

3.4 Summary

A detailed review of the state of the art in the PAPR of the MCM techniques based OWC has been conducted in this chapter. This review covers the undesirable PAPR challenge of the O-OFDM signal that employed to modulate the intensity of the light source with limited dynamic range. This also includes the used metrics to measure the high PAPR, PAPR measurement and statistical characterisation method. In addition, PAPR simulation and results of

different O-OFDM signal are presented in this chapter. Furthermore, PAPR reduction techniques for the MCM modulation systems in the literature are covered. Details of pilot-assisted (PA) technique that is implemented to reduce the PAPR peaks of O-OFDM systems in this work is also included in this chapter. This includes the PA technique implementation details, procedure and performance.

The PA's PAPR reduction performance is validated for different OFDM based systems in simulation and experimentally in the rest of the thesis. This including analytical studies for the minimisation of the clipping noise in the limited dynamic range of light source of the VLC system.

Chapter 4
Study of Clipping Noise in PAPR Reduced DCO-OFDM System

4.1 Introduction

In this chapter, analytical study of clipping noise that leads to distortion in a DCO-OFDM based VLC system due to front-end devices limitations is presented. To mitigate the clipping noise, PAPR of the DCO-OFDM is reduced by the PA technique. The analytical BER performance of the system with PAPR reduction is verified through simulation and then compared to that of the conventional DCO-OFDM system without PAPR reduction at similar clipping levels. The proposed PA DCO-OFDM system shows better BER performance at all clipping levels. Specific contributions of this manuscript are as follows:

- Analytical investigation of a PAPR reduction using PA scheme in PA DCO-OFDM based VLC system in the presence of clipping noise.

- The PA technique is applied to reduce clipping/non-linear distortion and improve the error performance of the system.

- The BER performance of the PA DCO-OFDM is investigated analytically at different clipping levels and compared to the performance of conventional DCO-OFDM without PAPR reduction.

- The analytical comparison is verified through simulation at the selected clipping levels for the compared systems.

In VLC system, the saturation effect of the light source (LED) results in a limited linear dynamic range of the transmitter front-end devices. MCM signals based on OFDM, such as DCO-OFDM, ACO-OFDM and PAM-DMT with multi-level M-QAM/PAM, follow Gaussian and half-Gaussian distribution for a large number of subcarriers ≥ 64. As a result, such signals have a high PAPR, and transmitted by the optical transmitter in a nonlinear fashion [99]. The

nonlinear distortion and high PAPR result in transmitted signal clipping. The clipping is generally caused by front-end devices limitation of the VLC system and the insufficient forward DC biasing. Therefore, this degrades the system BER performance or increases the electrical SNR requirement due the nonlinear distortion. In order to alleviate this issue, Pilot-assisted (PA) technique is implemented on the OFDM signal to reduce its high PAPR peaks. PAPR reduction minimises the clipping noise and the nonlinearity effect which allows for higher input power and maximises the available SNR of the system. PA technique is an effective solution for PAPR reduction in optical OFDM based systems [26]. In this work, PA is applied on DCO-OFDM for PAPR reduction purpose by rotating the phase of the transmitted OFDM data frame using a randomly generated pilot sequence. The phase rotation is used in order to avoid coherent addition of subcarriers as much as possible. The used pilot sequence phase is selected based on the SLM algorithm [46] while recovered at the receiver side by ML algorithm [65].

4.1.1   The Aim of this Study

In this chapter, the DCO-OFDM modulation technique is considered with PAPR reduction using PA technique in (PA DCO-OFDM) with the presence of double-sided clipping is investigated analytically. The clipping is due to VLC front-end devices limitation. The signal clipping introduces clipping noise and signal distortion to the transmitted signal. The attenuation factor and the variance of the clipping noise at the received waveform are determined in closed-form which included in the derivation and calculation of the system SNR. The system's BER performance of the clipped PAPR reduced PA DCO-OFDM is investigated at three different clipping levels. The clipping levels are varied by the amount of the forward DC biasing that is added to the transmitted signal to fit the dynamic range of the light source. Adding insufficient forward DC biasing results in upper and/or lower clipping of the transmitted time domain signal. Hence, reducing the forward DC biasing from its optimal point increases the signal clipping at the bottom side. The clipping noise attenuation can be modelled at the receiver as additive zero-mean complex-valued Gaussian noise according to the Bussgang theorem and the CLT [136], [126]. This investigation is verified through simulation and analytical studies at the selected clipping levels and then compared to that of conventional DCO-OFDM without PAPR reduction.
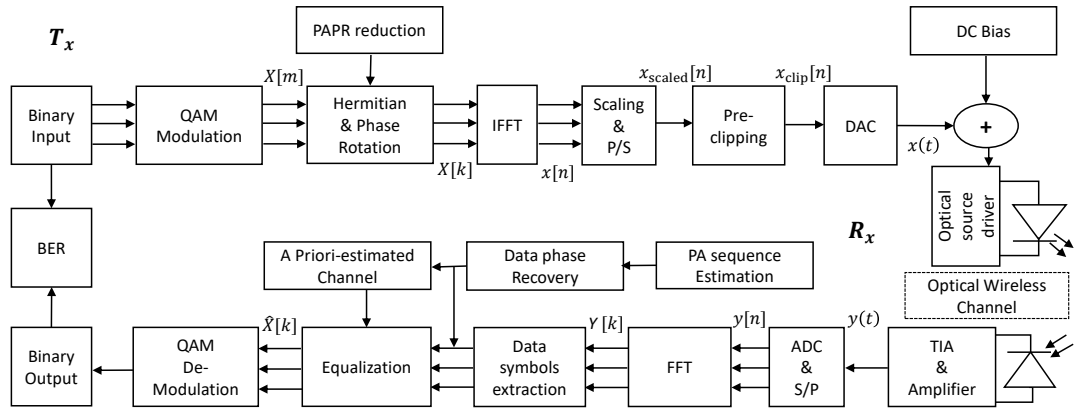
Figure 4.1: *Block diagram of the PA DCO-OFDM based VLC system.*

4.2 System Description

The system model considered in this study is illustrated in Fig. 4.1. First, a random bit stream is generated and encoded into complex-valued quadrature amplitude modulation (QAM) symbols $X[m]$ for $m = 1, 2, \ldots, \frac{N}{2} - 1$, where m is the active subcarriers index in the OFDM frame, and N is the OFDM frame size. The number of bits b that are mapped on each M-QAM symbol is given by $b = \log_2(M)$. The QAM symbols' vector $X[m]$ is considered with a unit variance. The conventional OFDM waveform is complex and bipolar. However, the transmission mechanism in OWC system is IM/DD which requires a real and positive waveform. This requirement is met by imposing Hermitian symmetry on the OFDM frame in the frequency domain, $X[l] = X^*[N - m]$. The OFDM frame in the frequency domain is given by the following [114]

$$X[k] = \left[0, X_1, \ldots, X_{\frac{N}{2}-1}, 0, X_{\frac{N}{2}-1}^*, \ldots, X_1^* \right] \tag{4.1}$$

where k is the subcarrier index with size N and $X[0] = X[N/2] = 0$. The utilisation factor for the OFDM frame's double-sided bandwidth B is denoted by G_{B} where $G_{\mathrm{B}} = (N - 2)/N$. The total number of enabled subcarriers on the OFDM frame is $G_{\mathrm{B}} \times N$. The OFDM frame activates all subcarriers which can enable different modulation format, M, across the OFDM frame. The average electrical power of the M-QAM symbol, $P_{\mathrm{s(elec)}} = P_{\mathrm{b(elec)}} \times \log_2(M)$, where $P_{\mathrm{b(elec)}}$ is the average electrical power per bit of the M-QAM symbol. The high PAPR peaks of the time domain signal are reduced using PA technique by rotating the phase of $X[k]$

prior to IFFT process as detailed in Section (6.2.2). The $X[k]$ symbols are then modulated into orthogonal subcarriers by applying an IFFT of size N to obtain a discrete time domain signal $x[n]$ as follows

$$x[n] = \frac{1}{\sqrt{N}} \sum_{k=0}^{N-1} X[k] \, e^{j2\pi \frac{kn}{N}} \; ; \qquad 0 \leq n \leq N-1 \tag{4.2}$$

where $j = \sqrt{(-1)}$. In general, a CP is included in OFDM-based systems to combat ISI and inter-carrier interference (ICI). This is done by copying the last few samples of the OFDM frame to the beginning of that frame to transform the linear convolution with the optical channel to a circular one. The CP length, N_{CP}, must be greater than the channel delay spread to mitigate ISI, hence the frame length becomes $(N + N_{\mathrm{CP}})$ [29]. The CP is omitted in this work for simplicity as it has negligible impact on the electrical SNR, spectral efficiency and electrical PAPR values of the system [26].

The discrete time-domain signal $x[n]$ is approximately Gaussian distributed with zero mean and variance of σ_x^2 according to CLT [126]. The average electrical power of the time domain signal $x[n]$ is proportional to its variance, σ_x^2 [116]. Therefore, to achieve a specific SNR, $x[n]$ should be scaled properly in relation with σ_x^2. Hence, the signal is scaled by a factor, α, to produce a specific $\sigma_{x_{\mathrm{scaled}}}^2$ of the scaled signal $x_{\mathrm{scaled}}[n]$. The variance, $\sigma_{x_{\mathrm{scaled}}}^2$, of the scaled signal is given as follows

$$\sigma_{x_{\mathrm{scaled}}}^2 = \alpha^2 \times \sigma_x^2 \tag{4.3}$$

where σ_x^2 is the variance of $x[n]$.

Light sources such as LEDs has limited dynamic range between $[i_{\min}, \, i_{\max}]$, that corresponds to minimum and maximum current points, respectively. To efficiently utilise that dynamic range, structure-specific signal pre-clipping has to be performed within the range $[k_{\mathrm{b}}, \, k_{\mathrm{t}}]$, which denotes the predefined bottom and top clipping levels, respectively as shown in Fig. 4.2. Then, the pre-clipped PA DCO-OFDM signal is biased to fit the linear dynamic range of the LED by a bias current, i_{bias}. The biasing process is employed to facilitate minimal bottom and top levels signal clipping by placing the signal mean in the middle of the LED's linear dynamic region [36]. The pre-clipping levels can be defined as follows

$$k_{\mathrm{b}} = i_{\min} - i_{\mathrm{bias}}, \qquad k_{\mathrm{t}} = i_{\max} - i_{\mathrm{bias}} \tag{4.4}$$

66

In the zero signal clipping scenario, the signal clipping is defined as: $k_\mathrm{b} = -\infty$, and $k_\mathrm{t} = +\infty$. The PA DCO-OFDM clipping levels can be negative and/or positive as long as the two clipping levels are not equal, $k_\mathrm{b} < k_\mathrm{t}$. In insufficient biasing scenarios, the signal is pre-clipped at bottom level, k_b. Moreover, the signal is pre-clipped at top level, k_t. Therefore, the clipped signal $x_\mathrm{clip}[n]$ can be expressed as follows

$$x_\mathrm{clip}[n] = \begin{cases} k_\mathrm{t} & \text{if } x_\mathrm{scaled}[n] \geq k_\mathrm{t}, \\ x_\mathrm{scaled}[n] & \text{if } k_\mathrm{b} < x_\mathrm{scaled}[n] < k_\mathrm{t}, \\ k_\mathrm{b} & \text{if } x_\mathrm{scaled}[n] \leq k_\mathrm{b}. \end{cases} \qquad (4.5)$$

When an OFDM time domain signal is clipped, it changes its mean and, as a result, its average optical power. To achieve a maximal signal power and to transform the electrical signal into an optical one, the linear dynamic range P_min and P_max should be mapped by the clipping levels, k_b and k_t as depicted in Fig. 4.2. Hence, to form such mapping, an input biasing power $P_\mathrm{bias} = \zeta \times i_\mathrm{bias}$, is required and can be expressed as

$$P_\mathrm{min} = \zeta(k_\mathrm{b} + i_\mathrm{bias}), \qquad P_\mathrm{max} = \zeta(k_\mathrm{t} + i_\mathrm{bias}) \qquad (4.6)$$

where ζ is the electrical to optical conversion coefficient.

The clipped continuous time domain waveform $x(t)$ is obtained from the clipped signal, $x_\mathrm{clip}[n]$, following the DAC process to modulate the intensity of the optical source. In general, the entire forward voltage range across the LED is supported by a sufficient constant bias current source which converts the bipolar time domain baseband waveform to a unipolar signal. The bias current is combined with the data waveform current, producing the total forward current through the LED. Since the radiated optical power by the LED is proportional to the forward current, the data waveform, the bias current i_bias and the system constraints imposed by the front-end devices are described in terms of optical power [36]. Therefore, the average transmitted optical power through the LED is given as

$$P_\mathrm{opt} = \zeta \times \mathrm{E}[\mathrm{x(t)}] + \mathrm{P}_\mathrm{bias} \qquad (4.7)$$

The PA DCO-OFDM frame is assumed to be transmitted within the -3 dB bandwidth of the used LED, hence, the optical channel is flat over the entire transmitted OFDM frame. The
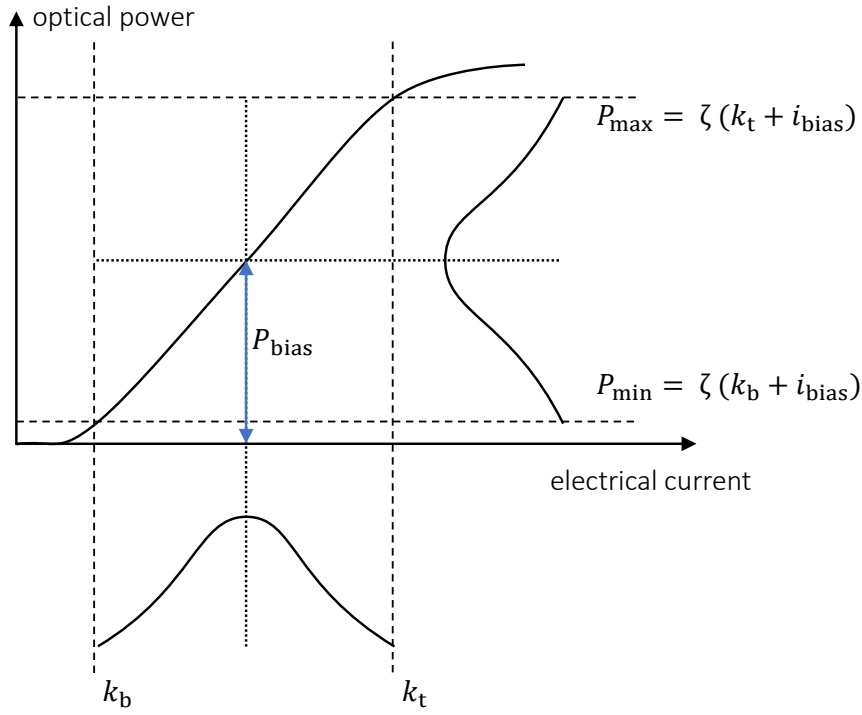
Figure 4.2: *An illustration of VLC optical source electrical signal to optical signal conversion.*

signal is unlikely to be clipped at the receiver side. For example, the PD has a linear dynamic range much higher than that of the transmitter, that needs very high amount of radiated power in order to drive the PD to its saturation region. At the receiver, a PD converts the received optical radiation into a current signal prior to a TIA which converts the current signal to the corresponding voltage. The voltage signal is then amplified to an appropriate level to obtain $y(t)$ prior to an ADC process. The received time domain waveform $y(t)$ is given by

$$y(t) = h(t) \circledast x_{\text{clip}}(t) + w_{\text{rx}}(t) \tag{4.8}$$

where $h(t)$ is the channel impulse response (CIR), $w_{\text{rx}}(t)$ is the received white Gaussian noise with variance $\sigma^2_{w_{\text{rx}}}$, and $\circledast$ denotes a convolution operation. The received signal $y(t)$ is then converted to a discrete time domain signal $y[n]$ by the ADC block followed by serial-to-parallel (S/P) transformation. The received signal is distorted by zero-mean real-valued bipolar AWGN $w_{\text{rx}}(t)$ which consists of the receiver's shot and thermal noises. The FFT is applied on $y[n]$ which transforms the signal back to the frequency domain and given by

$$Y[k] = \frac{1}{\sqrt{N}} \sum_{n=0}^{N-1} y[n]\, e^{-j2\pi \frac{kn}{N}} \; ; \qquad 0 \leq k \leq N-1 \tag{4.9}$$

The obtained frequency domain symbol $Y[k]$ can be expressed as follows

$$Y[k] = H[k] \cdot X_{\text{clip}}[k] + W_{\text{rx}}[k] \tag{4.10}$$

The AWGN $W_{\text{rx}}[k]$ noise after the FFT operation can be modelled as zero-mean complex AWGN with two sided power spectral density of $N_0/2$ per dimension and a variance of $\sigma_{w_{\text{rx}}}^2 = BN_0$ [36]. The embedded pilot sequence is extracted from the received data symbols, then its phase and amplitude are estimated based on the ML algorithm. The estimated pilot phase is used to reverse the phase rotation carried out at the transmitter. The received data symbols are then demodulated before being converted to bit streams followed by BER calculation based on the demodulated binary streams. In the simulation process for the analytical study validation, similar parameters and approach are used to investigate the system at an ideal case with no clipping introduced in addition to three clipping levels.

4.3 Analysis of Clipping Noise

The clipping of PA DCO-OFDM time domain signal changes the signal mean and, as a result, its average optical power. Since $x_{\text{clip}}[n]$ is approximately Gaussian, the nonlinear distortion effects caused by the clipping operation can be modelled according to the Bussgang theorem, and expressed as follows [136]

$$x_{\text{clip}}[n] = \kappa \cdot x_{\text{scaled}}[n] + w_{\text{clip}}[n] \tag{4.11}$$

where κ denotes the clipping attenuation factor and w_{clip} is the nonlinear distortion i.e. clipping noise imposed by the pre-clipping process and system front-end devices constraints. The nonlinear distortion w_{clip} is uncorrelated with the transmitted signal $x_{\text{scaled}}[n]$, $\text{E}[x_{\text{scaled}}[n] \cdot w_{\text{clip}}[n]] = 0$ where $\text{E}[\cdot]$ is the statistical expectation. The attenuation factor κ is a constant that is given as [36]

$$\kappa = \frac{\mathrm{E}[\mathrm{x_{scaled}}[n] \cdot \mathrm{x_{clip}}[n]]}{\sigma_{x_{scaled}}^2} \tag{4.12}$$

where $\sigma_{x_{scaled}}^2$ is the variance of $x_{scaled}[n]$. The nonlinear distortion w_{clip} is a non-Gaussian noise. However, due to the CLT, its representation in the frequency domain follows a Gaussian distribution with a zero mean and a variance $\sigma_{w_{clip}}^2$. The variance of the clipping noise is given as follows [36, 137]

$$\mathrm{E}[\mathrm{w_{clip}}] = \mathrm{E}[\mathrm{x_{clip}}], \tag{4.13a}$$

$$\sigma_{w_{clip}}^2 = \mathrm{E}[\mathrm{w_{clip}^2}] - \mathrm{E}[\mathrm{w_{clip}}]^2, \tag{4.13b}$$

$$\sigma_{w_{clip}}^2 = \mathrm{E}[\mathrm{x_{clip}^2}] - \kappa^2 \sigma_{x_{scaled}}^2 - \mathrm{E}[\mathrm{x_{clip}}]^2. \tag{4.13c}$$

Applying a FFT property to the received signal $y[n]$ translates the signal to the frequency domain and converts the convolution operation to multiplication one. In the frequency domain, the clipping noise $w_{clip}[n]$ is transformed into additive Gaussian noise according to CLT. Therefore, additive Gaussian noise component with zero-mean and variance $\sigma_{w_{clip}}^2$ is present at each modulated subcarrier in addition to the additive white Gaussian noise $w_{rx}[n]$. Therefore, the received signal in the frequency domain can be calculated as follows [36]

$$Y[k] = H[k] \left(\kappa \cdot X[k] + W_{clip}[k] \right) + W_{rx}[k],$$

$$\tag{4.14}$$

$$= \kappa H[k] X[k] + H[k] W_{clip}[k] + W_{rx}[k].$$

where $Y[k]$ is the desired received signal, $H[k]$ is the channel response at subcarrier k, $X[k]$ is the transmitted symbols, $W_{clip}[k]$ is the clipping noise, and $W_{rx}[k]$ is the additive white Gaussian noise. The received signal can be expressed as the summation of the desired signal, clipping noise and the receiver noise with zero mean for both noise signals as shown in (4.14). The SNR at the kth subcarrier is represented by $\Gamma[k]$, and can be expressed as follows [36]

$$\Gamma[k] = \frac{\kappa^2 \frac{1}{G_B} |H[k]|^2}{\sigma_{w_{clip}}^2 |H[k]|^2 + \sigma_{w_{rx}}^2}. \tag{4.15}$$

where G_B is the double-sided bandwidth utilisation factor of the optical OFDM frame and $\sigma_{w_{rx}}^2$

is the receiver noise power. The attenuation factor can be simplified from (4.12) as follows [36]

$$\kappa = Q(k_{b_{norm}}) - Q(k_{t_{norm}}) \tag{4.16}$$

where Q is the Q-function [36]. $k_{b_{norm}}$ and $k_{t_{norm}}$ are the normalised bottom and top clipping levels respectively, and can be expressed as follows [36]

$$k_{b_{norm}} = \frac{k_b}{\sigma_{x_{scaled}}} \tag{4.17}$$

$$k_{t_{norm}} = \frac{k_t}{\sigma_{x_{scaled}}} \tag{4.18}$$

The clipping noise variance is given as [36]

$$\begin{aligned}
\sigma^2_{w_{clip}} = {} & \kappa + k_{b_{norm}}\phi(k_{b_{norm}}) - k_{t_{norm}}\phi(k_{t_{norm}}) + k^2_{b_{norm}} \\
& [1 - Q(k_{b_{norm}})] + k^2_{t_{norm}}Q(k_{t_{norm}}) - \kappa^2 - \\
& [\phi(k_{b_{norm}}) - \phi(k_{t_{norm}}) + k_{b_{norm}}[1 - Q(k_{b_{norm}})] + \\
& k_{t_{norm}}Q(k_{t_{norm}})]^2
\end{aligned} \tag{4.19}$$

where $\phi(\cdot)$ is the probability density function (PDF) of the standard Gaussian distribution which is given by

$$\phi(u) = \frac{1}{\sqrt{(2\pi)}} \exp\left(\frac{-u^2}{2}\right) \tag{4.20}$$

The complementary cumulative distribution function (CCDF) of the PDF of the standard Gaussian distribution, $Q(\cdot)$, is given as

$$Q(u) = \frac{1}{\sqrt{(2\pi)}} \int_u^\infty \exp\left(-\frac{x^2}{2}\right) dx \tag{4.21}$$

The average electrical power of the clipped time domain signal is given by [36]

$$\begin{aligned}
\mathrm{E}[\mathrm{x_{clip}[n]}] = {} & \phi(k_{b_{norm}}) - \phi(k_{t_{norm}}) + k_{t_{norm}}Q(k_{t_{norm}}) + \\
& k_{b_{norm}}[1 - Q(k_{b_{norm}})].
\end{aligned} \tag{4.22}$$

The BER of the kth subcarrier can be approximated as follows [36]

$$\text{BER[k]} \approx \frac{4(\sqrt{M}-1)}{\sqrt{M}\log_2(M)}Q\left(\sqrt{\frac{3\times\Gamma[k]}{M-1}}\right) + \frac{4(\sqrt{M}-2)}{\sqrt{M}\log_2(M)}Q\left(3\sqrt{\frac{3\times\Gamma[k]}{M-1}}\right) \quad (4.23)$$

4.4 Results and Discussion

The performance of PA DCO-OFDM and conventional DCO-OFDM systems are compared in the presence of double-sided signal clipping under AWGN channel in terms of BER and as a function of electrical SNR. The analytical study is verified by simulation for both systems. The two systems are simulated using 4-QAM modulation format and IFFT/FFT size of 2048. The optical path gain coefficient, the system bandwidth and the electrical to optical conversion coefficient, ζ, are constrained to unity. The optical source is assumed to be an LED with a linear dynamic range between $i_{\min} = 5$ mA and $i_{\max} = 50$ mA, which is assumed to be the source of clipping noise [36]. No clipping at the receiver is assumed. The two systems are compared at ideal case with no clipping introduced in addition to three clipping cases for analytical and simulation BER performance. In the three clipping cases, the clipping levels are calculated according to the amount of the added bias current, i_{bias}, to the transmitted signal and the LED's linear dynamic range where, $i_{\text{bias}} = 9.8$ mA is selected as in [36]. Hence, the bipolar signal is pre-clipped prior to biasing process at bottom level, $k_{\text{b}} = i_{\min} - i_{\text{bias}}$, and at top level, $k_{\text{t}} = i_{\max} - i_{\text{bias}}$. In the first case (case 1), both signals are clipped at bottom level, $k_{\text{b}} = -4.8$ and top level, $k_{\text{t}} = 40.2$. In second case (case 2), the signals are clipped at $k_{\text{b}} = -3.8$ and $k_{\text{t}} = 41.2$, whereas, it is clipped at $k_{\text{b}} = -3$ and $k_{\text{t}} = 42$ in third case (case 3). This clipping levels are obtained by reducing the i_{bias} which increases the lower clipping level. The data signal is generated, scaled, clipped and biased in MATLAB as detailed in Section 4.2 to form the DCO-OFDM signal. In addition, the same data symbols with the same process and parameters are generated with PAPR reduction algorithm using $R = 10$ iterations to generate the PA DCO-OFDM signal. This process is implemented to investigate the effect of reducing the high PAPR peaks of the signal on the system BER performance. Furthermore, the two signals are compared in terms of BER at the same scaling factor and biasing point for every clipping level. In addition, as a benchmark for comparison with existing results, (ideal case and case 1) for DCO-OFDM in [36] is selected, and signal scaling, biasing and clipping levels are included. Hence, the average transmitted optical power $P_{\text{opt}} = 10$ mW. In the ideal case where no clipping is introduced to the transmitted signals, the two systems have achieved identical

BER performance as illustrated in Fig. 4.3a. In the clipping case 1, the i_{bias} is found to be 9.8 mA, and $\sigma_{x_{\mathrm{scaled}}}$ = 4.9 mA for DCO-OFDM as obtained in [36]. Whereas, reducing the PAPR of the signal in PA DCO-OFDM with same scaling factor α and i_{bias} realised at $\sigma_{x_{\mathrm{scaled}}}$ = 4.69 mA. This scaling and biasing setup yield the following normalised clipping levels. In DCO-OFDM, the normalised bottom clipping level $k_{\mathrm{b_{norm}}}$ = - 0.98, and the normalised top clipping level $k_{\mathrm{t_{norm}}}$ = 8.2. In PA DCO-OFDM, $k_{\mathrm{b_{norm}}}$ = -1.02, and $k_{\mathrm{t_{norm}}}$ = 8.57. The analytical and simulation of this case for the two systems are illustrated in Fig. 4.3b.
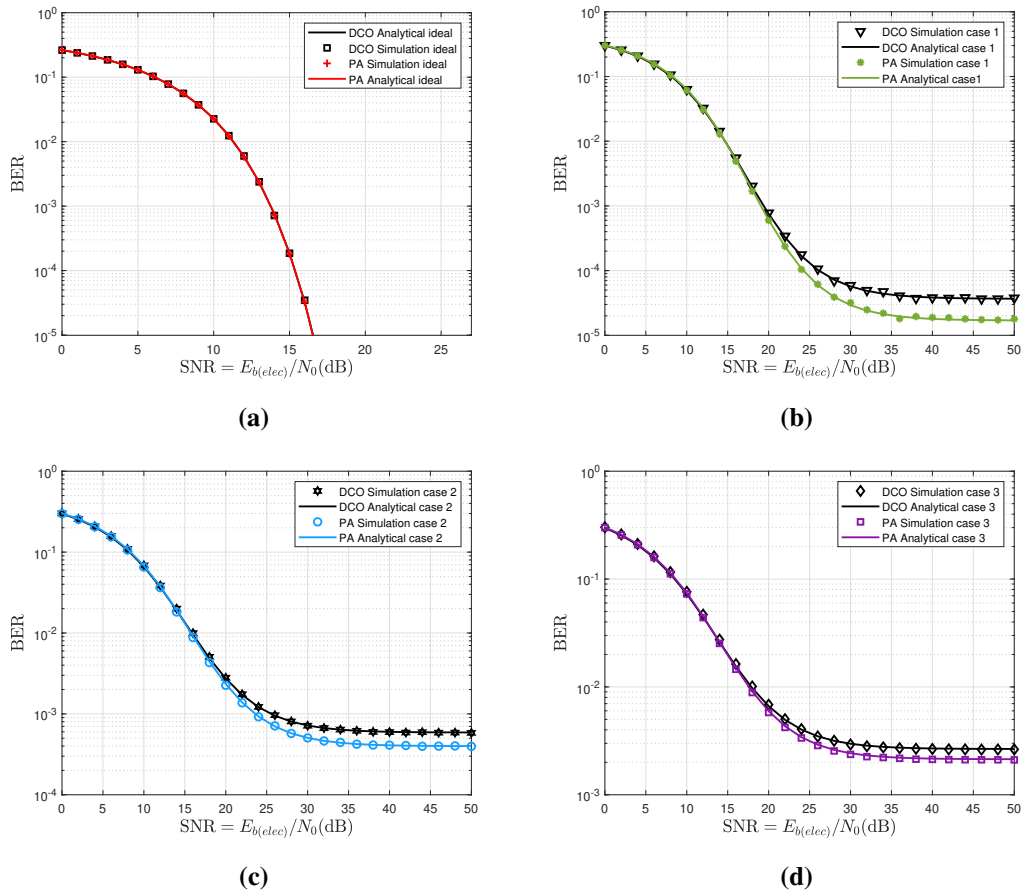
Figure 4.3: *Analytical and simulation BER for PA DCO-OFDM and conventional DCO-OFDM. (a) ideal case (zero clipping), (b) case 1 (minimum clipping), (c) case 2 (more clipping), (d) case 3 (severe clipping).*

In the second case (case 2), the bias current is reduced to i_{bias} = 8.8 mA, which increases the lower clipping level, hence, increases the clipping noise. Furthermore, this modifies the normalised clipping levels to be, $k_{\mathrm{b_{norm}}}$ = -0.78, and $k_{\mathrm{t_{norm}}}$ = 8.4 for DCO-OFDM While, for PA DCO-OFDM $k_{\mathrm{b_{norm}}}$ = -0.81, and $k_{\mathrm{t_{norm}}}$ = 8.78. The BER performance of this setup is

shown in Fig. 4.3c for both systems.

In the third case (case 3), the normalised clipping levels are modified by reducing the bias current, $i_{\text{bias}} = 8$ mA. This results in increasing the lower level clipping where $k_{\text{b}_{\text{norm}}} = -0.61$, and $k_{\text{t}_{\text{norm}}} = 8.57$ for DCO-OFDM While for PA DCO-OFDM, $k_{\text{b}_{\text{norm}}} = -0.64$, and $k_{\text{t}_{\text{norm}}} = 8.95$, which are shown in Fig. 4.3d.

In all clipping cases, the PA DCO-OFDM has achieved better BER performance than that of conventional DCO-OFDM without PAPR reduction as shown in Fig. 4.3b, 4.3c and 4.3d. PA DCO-OFDM requires less i_{bias} to convert the signal's negative peaks to positive, hence, PA DCO-OFDM is more efficient in terms of optical power than the conventional DCO-OFDM. Furthermore, PA DCO-OFDM is expected to perform better under clipping conditions as shown in Fig. 4.3, by reducing the high peaks of the OFDM waveform which results in minimising the nonlinearity effect and the clipping distortion. As a result, system SNR is maximised hence, better BER performance of the system is observed. In addition, PA DCO-OFDM allows the signal to have more swing within the linear dynamic range of the system transmitter and reduces the upper and/or lower level clipping effect. The error floor observed in the results is caused by the clipping. And in all cases, the error floor is lower with PAPR reduction technique implemented.

4.5 Summary

The clipping noise in PAPR reduced system (PA DCO-OFDM) is investigated in this work. This includes the clipping noise attenuation factor and the variance of clipping noise at the received waveform which are determined in closed-form. The SNR of the system is calculated based on the determined attenuation factor and noise variance. The system's analytical BER performance of the clipped PAPR reduced PA DCO-OFDM is verified through simulation studies at different clipping levels. The BER of PA DCO-OFDM is then compared to that of conventional DCO-OFDM without PAPR reduction at the selected clipping levels. The PA DCO-OFDM has achieved better BER performance than that of conventional DCO-OFDM without PAPR reduction in the all used clipping levels. The high PAPR values reduction of the transmitted signal in PA DCO-OFDM reduces the clipping noise hence, enhances the system BER performance. PAPR reduction has the potential to reduce the transmitted average optical power by reducing the required bias power P_{bias} which results in increasing the reliability of

the LED and hence, its lifetime span. The BER gain can be used to increase the transmitted optical power for longer transmission distance and/or higher achievable data rate.

Chapter 5

PAPR Reduction in PAM-DMT based VLC Systems

5.1 Introduction

In this chapter, The high PAPR peaks of the PAM-DMT system is evaluated and reduced by implementing the PA technique and the system performance is investigated experimentally for a VLC system. The experimental performance of PA scheme is then verified by simulation. The performance of PAPR reduced PA PAM-DMT and conventional PAM-DMT without PAPR reduction are compared in terms of BER. The system parameters are optimised and the performance of the resulting PA PAM-DMT is utilised with adaptive bit and power loading and investigated experimentally in terms of BER and achievable data rate. The performance of PA PAM-DMT is compared to that of conventional PAM-DMT. Specific contributions of this work are as follows:

- Experimental demonstration of a PAPR reduction using PA scheme in PA PAM-DMT based VLC system.

- For the first time, the PA technique is applied to a PAM-DMT based VLC system experimentally to reduce clipping/nonlinear distortion, and minimise the error performance while maintaining the achievable data rate.

- Comparison of PA PAM-DMT system's data rate and BER with that of conventional PAM-DMT without PAPR reduction.

- The experimental study is verified through simulation.

PAM-DMT was proposed in [33], to improve the spectral and energy inefficiency of ACO-OFDM and DCO-OFDM respectively. In PAM-DMT, the PAM symbols are modulated onto the imaginary components while, the real parts are set to zeros. PAM-DMT activates all subcarriers and

allows for asymmetrical clipping at zero level and transmit only the positive samples of the DMT signal.

Despite the advantages of the PAM-DMT technique, it is affected by high PAPR due to coherent addition of the individual subcarriers in the transmitted frame. PAPR induces signal distortion which is undesirable in OWC systems due to the limited dynamic range of the system front-end devices. This in turn restricts the average transmitted optical power and causes system performance degradation [26]. Various solutions have been proposed to address the PAPR challenge. PA scheme is use in this work to address PAPR challenge. PA is an interesting solution for the reduction of the PAPR in OFDM systems. This technique uses a random pilot to rotate the phase of the data frame in order to avoid the coherent addition of the subcarriers [26].

5.2   System Description

5.2.1   Optical PAM-DMT System

In PAM-DMT, the imaginary components of the complex-valued PAM symbols are modulated and, the real parts are not used and set to zeros. This results in $X[k] = jB_{\mathrm{PAM}}[k]$, where $B_{\mathrm{PAM}}[k]$ is the M-PAM symbols carrying useful data that are loaded on the imaginary components where $(k = 1, 2, \ldots, N/2-1)$ and $N = 2(N_{\mathrm{subs}}+1)$ where N_{subs} is the active subcarriers carrying information [33]. An optical source in a VLC system is modulated by a real-valued baseband waveform which means that the time domain signal of PAM-DMT must be real and positive. The real-valued time domain signal is achieved by imposing a Hermitian symmetry on the PAM mapped symbols in the frequency domain which is given by: $X[k] = X^*[N/2 - k]$, where X^* indicates the conjugate of X and $X[0] = X[N/2] = 0$. The PAM-DMT frame in the frequency domain with the Hermitian symmetry is given as follows:

$$X_{\mathrm{H}} = \left[0, X_1, \ldots, X_{N/2-1}, 0, X^*_{N/2-1}, \ldots, X^*_1 \right] \tag{5.1}$$

To sufficiently capture all the signal peaks across the IFFT length, zero padding is inserted into the frequency domain for oversampling. The value for the oversampling factor is chosen at $L = 4$ similar to [26], hence (5.1) can be given as follows:

$$X_{\text{H}} = \left[0, X(k), \underbrace{0, 0, \ldots, 0}_{\text{N(L-1)/2}}, 0, 0, \underbrace{0, 0, \ldots, 0}_{\text{N(L-1)/2}}, X^*(N_{\text{IFFT}} - k) \right] \tag{5.2}$$

The corresponding discrete time domain signal $x[n]$ is obtained by applying size N_{IFFT} IFFT to the frequency domain signal , where $N_{\text{IFFT}} = N \times L$ which can be expressed as follows [33]:

$$x[n] = \frac{-2}{\sqrt{N_{\text{IFFT}}}} \sum_{k=1}^{N_{\text{IFFT}}/2-1} B_{\text{PAM}}[k] \sin\left(2\pi k \frac{n}{N_{\text{IFFT}}}\right) \tag{5.3}$$

where $n = 0, 1, 2, \ldots, N_{\text{IFFT}} - 1$.Then CP is inserted at the beginning of each PAM-DMT frame to eliminate the ISI in dispersive channel [26]. The time domain waveform follows an anti-symmetry property which can be visualised in Fig. 5.1. As a result of the anti-symmetry $x[n] = -x[N - n]$, the clipping of the negative peaks in the time domain PAM-DMT signal $x[n]$ does not affect the useful information as the same information are loaded on the positive components of the second half of the waveform. This means that zero level clipping distortion only affects the real components of the subcarriers, and the useful data can be recovered from the imaginary components [33].

A continuous time domain signal $x(t)$ of the system is obtained by feeding the discrete signal $x[n]$ in (5.3) into a DAC which is then used to modulate the intensity of the light source [26]. At the receiver, the real components of the subcarriers are ignored while the imaginary part is selected and re-scaled by a factor of 2. The signal is transformed back to frequency domain using FFT then extracted then equalized and demodulated to recover the useful information [138].

5.2.2 High PAPR Reduction in PAM-DMT

PAM-DMT allows asymmetric clipping at zero values and convey the useful information on the positive parts of the PAM-DMT signal $x[n]$ which makes full use of the all available subcarriers in the PAM-DMT frame [33]. However, the inherent high PAPR problem of the system must be addressed to benefit from the full dynamic range of the light source. The high PAPR problem will cause the following: 1) the optical source will have to operate outside its linear dynamic region to contain full amplitude swings of the signal, 2) the upper level clipping by the frond-
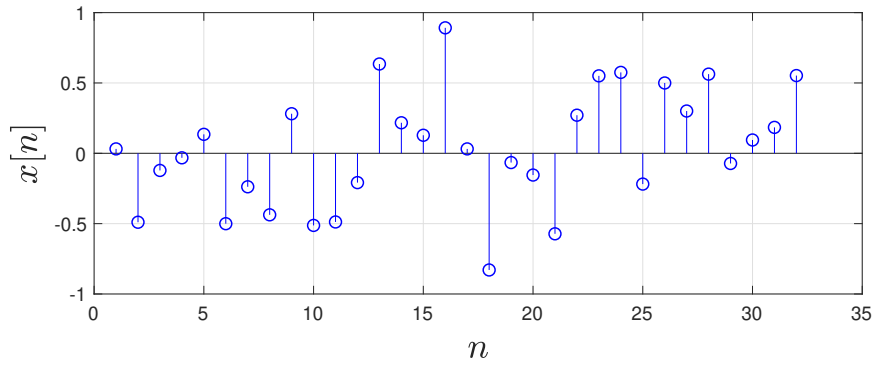
(a) *PAM-DMT time domain waveform.*
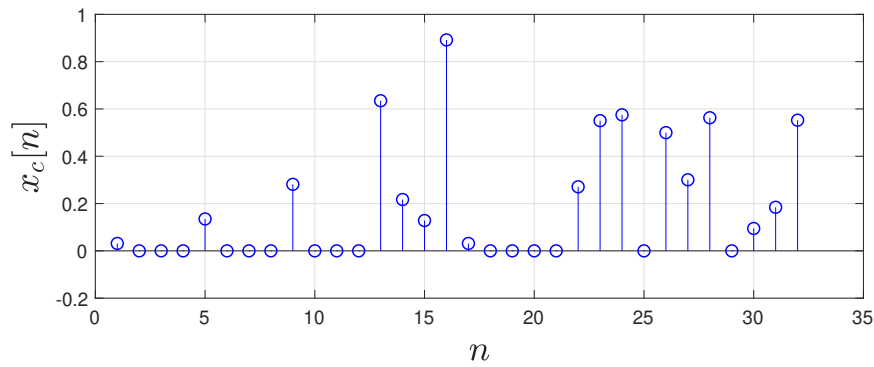
(b) *PAM-DMT clipped time domain waveform.*

Figure 5.1: *PAM-DMT time domain signal and clipped part.*

end devices of the system results in clipping noise and distortion introduced to the transmitted signal [35]. To address the PAPR problem, the PA is applied to reduce the high PAPR of the PAM-DMT system by rotating the phase of the PAM-DMT signal. However, its extension to PAM-DMT technique is not straightforward. In this section, PA technique implementation for PAM-DMT system is described and realised in the VLC system experimentally. The electrical PAPR of the over-sampled time domain PAM-DMT symbol is defined as follows [26]:

$$\text{PAPR} = \frac{\max\limits_{0 \le n \le N_{\text{IFFT}} - 1}(|x[n]|^2)}{\text{E}[|x[n]|^2]} \tag{5.4}$$

where $\text{E}[\cdot]$ is the statistical expectation. The PAPR is evaluated using the CCDF and it is the most used measure for PAPR reduction [26]. The CCDF is defined as the probability that the PAM-DMT frame PAPR exceeds a predefined reference value. High PAPR peaks appear when

individual subcarriers added up coherently in the time domain [34].

The procedure of PAPR reduction using PA technique in PAM-DMT is described as follows [26]:

- Group the frequency domain frames of PAM-DMT into U blocks comprise of active subcarriers N_{subs}; where, $X^u[k]$, $u = 1, 2, \ldots, U$.

- Generate R multiple iterations of pilot sequence candidates with N_{subs} length, X_{p}^r, where $r = 1, 2, \ldots, R$.

- Select the sequence X_{p}^r amplitude $A_{\text{p}}(k)$ to be ± 1 only.

- Randomly set the pilot sequence phase $\theta_{\text{p}}(k)$ to 0 or π values only, where $k = 1, 2, \ldots, N_{\text{subs}}$.

- Rotate the block U phase by $\theta_{\text{p}}(k)$ of every pilot iteration r.

- Calculate the PAPR_r value of each iteration of X_{p}^r.

- Select the pilot iteration $X_{\text{p}}(k) = X_{\text{p}}^{\tilde{r}}(k)$ with minimum PAPR value for transmission; where [35],

$$\tilde{r} = \underset{1 \leq r \leq R}{\text{argmin}} \, (\text{PAPR}_r) \tag{5.5}$$

- convert the selected pilot sequence $X_{\text{p}}(k)$ into the imaginary domain.

- Embedded the pilot sequence $X_{\text{p}}(k)$ into the corresponding block U of frames for high PAPR reduction, and thus the number of frames per block U will become $\hat{U} = (U + 1)$.

In this work, the high PAPR peaks of the transmitted signal is reduced where the number of PAM-DMT frames are grouped to form a block U, and $U = 5$ frames per block. This value is selected because the PAPR increases as U increases [26]. The considered number of iterations is selected to $R = 10$ iterations because it shows a good trade off between performance and complexity [135]. CP is not used during the PAPR evaluation in this work as it has negligible effect on the PAPR of the system.

At the receiver, the received PA sequences are extracted from the data blocks, then estimated using ML technique. The ML is an optimum detection method to estimate the statistical parameter θ where the parameter values that are most likely to generate the observed data are
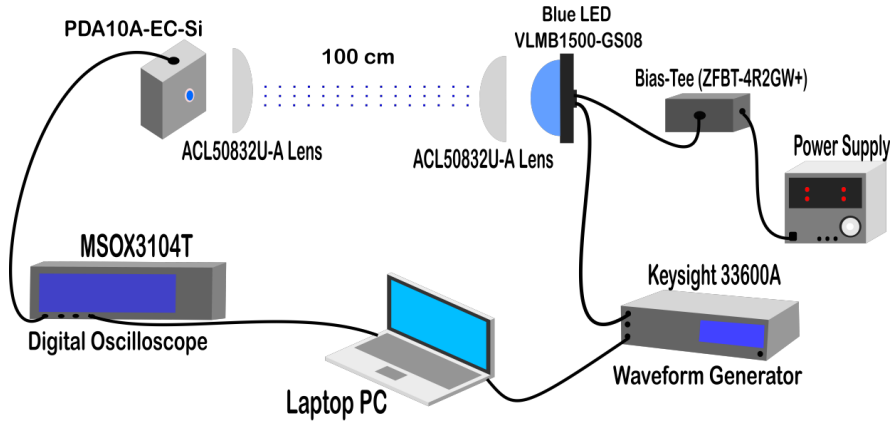
Figure 5.2: *An experimental setup for VLC system using a single Blue LED.*

chosen [65]. The ML technique is used in our work as follows [26]: at the receiver, the received PA sequences are extracted from the data blocks, then its noise corrupted phase $\hat{\theta}_{\mathrm{p}}(k)$ is estimated using ML technique to improve the data recovery. The estimate of the angle is taken between two values, $(\hat{\theta}_i = 0$ and $\pi)$ that has the minimum Euclidean distance from the received pilot's phase $\tilde{\theta}_{\mathrm{p}}$. The estimate argument is given by the following:

$$\hat{\theta}_{\mathrm{p}}(k) = \underset{1 \leq i \leq 2}{\mathrm{argmin}}[(\tilde{\theta}_{\mathrm{p}}(k) - \theta_{\mathrm{i}})^2] \tag{5.6}$$

The estimated pilot sequence becomes $\hat{\theta}_{\mathrm{p}}(k) = e^{j\hat{\theta}_{\mathrm{p}}(k)}$, which is equivalent to the following condition [26]:

$$\hat{\theta}_{\mathrm{p}}(k) = \begin{cases} +1, & \text{if} \quad \cos{(\tilde{\theta}_{\mathrm{p}}(k))} \geq 0 \\ -1, & \text{otherwise.} \end{cases} \tag{5.7}$$

In addition, the pilot's sequence amplitude, $\hat{A}_{\mathrm{p}}(k)$ is maintained to unity using the condition given in (5.7). The estimated PA phase $\hat{\theta}_{\mathrm{p}}(k)$ with recovered amplitude, $\hat{A}_{\mathrm{p}}(k)$, is then used to recover the phase of the corresponding subcarrier k for the corresponding block U of the received data prior to the equalisation process. The PA PAM-DMT system's PAPR reduction gain is discussed in the results section 5.4.

5.3 Experimental Setup and Data Transmission

An experiment is employed to evaluate the performance of PA PAM-DMT in a VLC system as illustrated in the experimental setup in Fig. 5.2 and the block diagram of the PA PAM-DMT
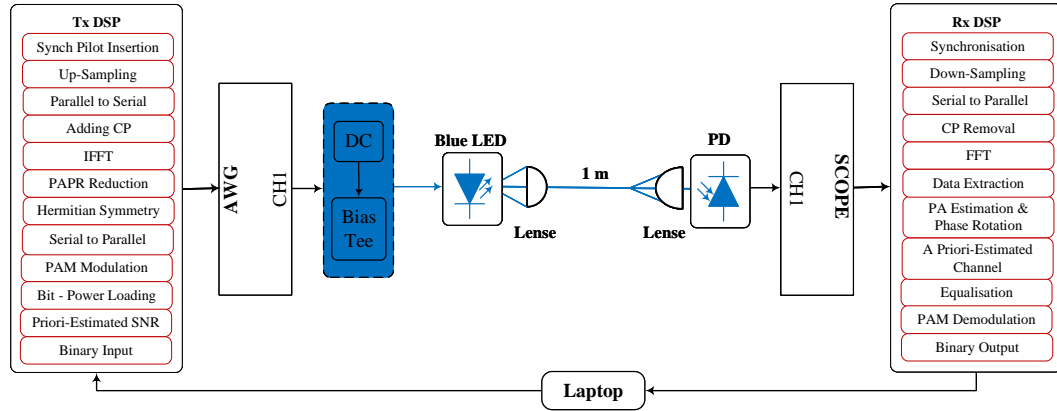
Figure 5.3: *An experimental block diagram for PA PAM-DMT based VLC system using a single Blue LED.*
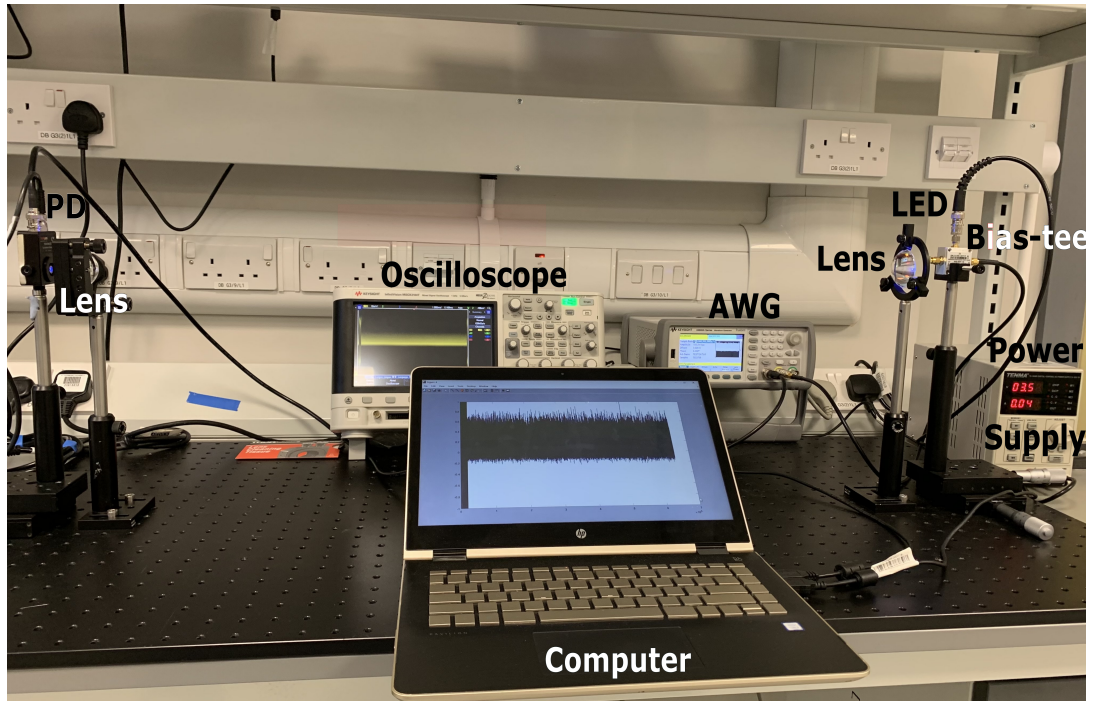
Figure 5.4: *The laboratory setup photograph of the optical VLC system showing the computer, the single Blue LED, optical lenses, AWG, oscilloscope and the photodetector.*

based VLC system is shown in Fig. 5.3. The real laboratory setup of the optical system is shown in Fig. 5.4. The system transmitter consists of a computer that controls a waveform generator, LED (Vishay VLMB1500-GS08) and a Bias-Tee. An amplified PD (PDA10A-EC-Si, 200-1100 nm, 150 MHz BW) is used as the optical signal receiver. The system performance in this work is investigated at $d = 100$ cm link distance. A longer distance measurement is possible using a higher power LED. A PA PAM-DMT signal is generated in MATLAB as detailed in section 5.2.1, and converted into an analogue waveform using arbitrary waveform generator (AWG) (Keysight 33622A) employed at 100 MHz transmission speed. The generated signal is DC biased using a bias-tee (ZFBT-4R2GW+). The DC bias is required for optical OFDM modulation techniques such as DCO-OFDM to convert the bipolar signal into a unipolar. This bias is not required for the unipolar PA PAM-DMT. However, a minimum DC bias is still required due to the turn on voltage of the used LED.

Two identical aspheric condenser lenses (ACL50832U-A) are used at the transmitter (LED) and the photo-receiver ends to collimate the output light of the LED and focus the light into the detection area of the PD respectively. The receiver is an amplified fixed gain detector which includes a reverse-biased PIN photo-diode, mated to a TIA. PD converts the received optical radiation into an electrical current signal which is converted afterwards into a voltage signal by the TIA [26]. The received signal is then captured with a digital oscilloscope (Keysight MSOX3104T - 1 GHz) and processed afterwards off-line using MATLAB. The received signal is equalized subsequently using zero forcing equalizer then demodulated using a PAM demodulator. The entire system 3 dB bandwidth is measured at 11.7 MHz.

The PA PAM-DMT system is investigated at different input current I_{DC} values to find the mid point of the linear region of the used LED. The I_{DC} point is selected in the linear region of the LED to avoid upper level clipping as much as possible. The operating point in this experiment is chosen to be around 3.31V which corresponds to a 20 mA input current to the LED as indicated in Fig. 5.5a as the PAM-DMT signal is clipped at zero level and only minimum DC bias is required due to the turn on voltage of the LED. Increasing the I_{DC} value increases the received optical power before the saturation point of the LED which causes system performance degradation as shown in Fig. 5.5b. However, minimising the clipping distortion due to front-end devices limitation is the priority of this work.

The system SNR is calculated at different input signal peak-to-peak voltage (V_{pp}) at the AWG
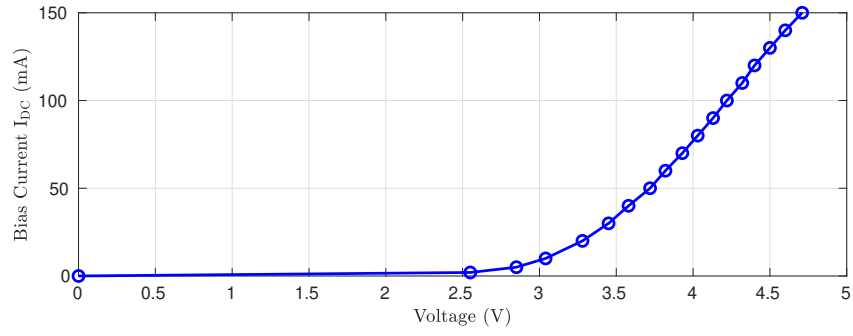
(a) *LED IV Curve.*
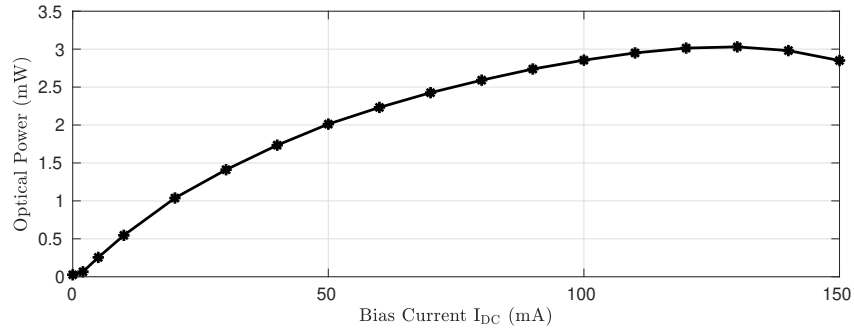
(b) *Received optical power vs input current I_{DC}.*

Figure 5.5: *Characteristics of LED (Vishay VLMB1500-GS08).*

using the CIR at the corresponding V_{pp} in frequency domain at the receiver side using (5.8).

$$\text{SNR}[k] = \frac{|H[k]|^2 \times |X[k]|^2}{|W[k]|^2} \tag{5.8}$$

where $H[k]$ is the CIR at sample k, $X[k]$ is the transmitted signal at sample k and $W[k]$ is the frequency domain estimated noise for sample k at the receiver. $H[k]$ is estimated using the prior knowledge of an embedded pilot to the transmitted signal as follows in (5.9):

$$\tilde{H}[k] = \frac{Y[k]}{X[k]} \tag{5.9}$$

where $Y[k]$ is given as follows in (5.10):

$$Y[k] = X[k] \times H[k] + W[k] \tag{5.10}$$

The noise estimate of the system is evaluated as shown below in (5.11):

$$\tilde{W}[k] = Y[k] - \tilde{H}[k]X[k] \tag{5.11}$$

The PA PAM-DMT system performance is investigated and compared to the conventional PAM-DMT without PAPR reduction in terms of received SNR and BER as detailed in Section (5.4).

5.4   Results and Discussions

In this work, the conventional PAM-DMT and PA PAM-DMT systems are compared in terms of PAPR values using the same random data streams, transmission parameters and system setup. The CCDF value of 10^{-4} is used in this work as a metric to compare the PAPR of both techniques. It can be observed from Fig. 5.6 that a PAPR reduction gain of 2.75 dB is achieved by applying PA scheme to the PAM-DMT system in PA PAM-DMT. At least one out of every 10^4 PAM-DMT frames has its PAPR greater than 17.5 dB. This is compared to values of 15.4 dB and 14.75 dB for PA PAM-DMT with $R = 5$ and 10 iterations respectively.
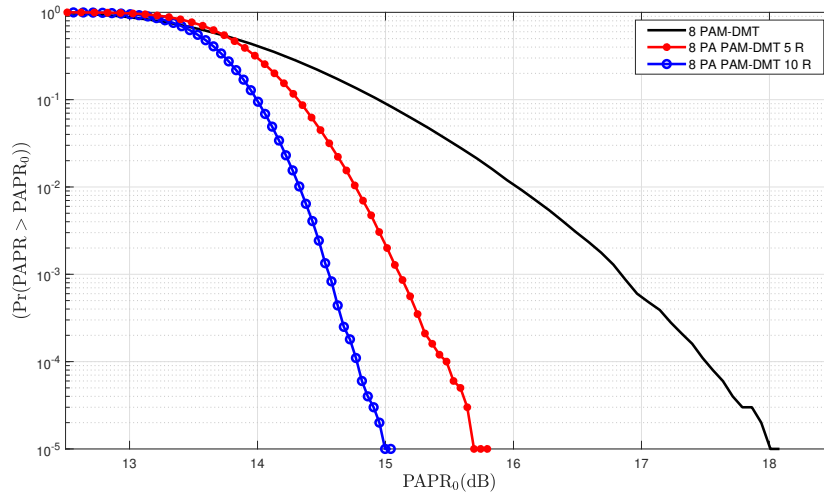
Figure 5.6: *PAPR CCDF plot for PA PAM-DMT and PAM-DMT.*

The distributions of the PAPR values of PAM-DMT and PA PAM-DMT for an 8-PAM constellation order are shown in Fig. 5.7. The PAM-DMT PAPR range is between 11.69 and 18.32 in dB. However, with PAPR reduction scheme used in PA PAM-DMT, the PAPR spread is considerably reduced to values between 12.08 and 15.16 in dB. This is a reduction of more than

3 dB in the range of PAPR values which translates to reducing the peak power and the average transmitted optical power. This results in minimising the signal distortion due to clipping caused by the front-end devices of the system hence, improves the system performance.
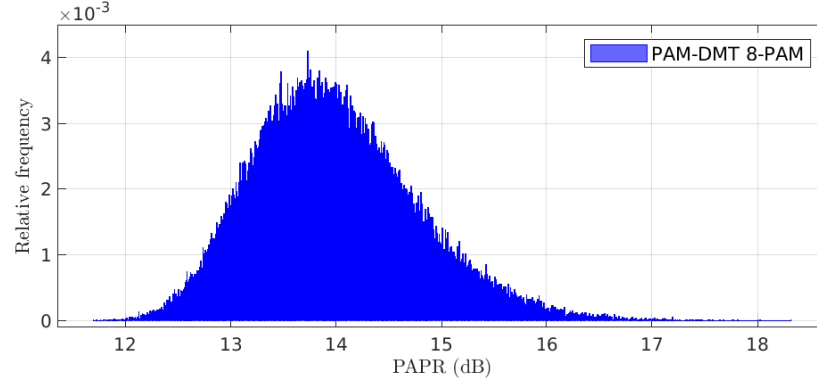
(a) *PAM-DMT PAPR distribution without high peaks reduction.*
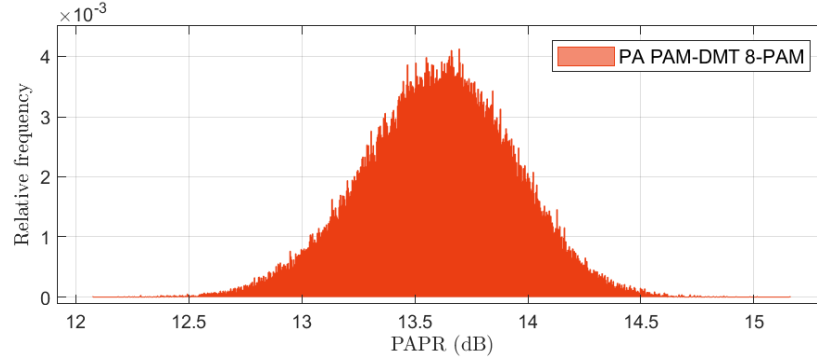
(b) *PA PAM-DMT PAPR distribution with high peaks reduction.*

Figure 5.7: *Distribution of the PAPR values of optical PAM-DMT and PA PAM-DMT.*

The system PAPR reduction gain of PA scheme shown in Fig. 5.6 and Fig. 5.7, is obtained using modulation format of 8-PAM, number of active subcarriers $N_{\text{subs}} = 127$, zero padding factor L = 4, data frames per block $U = 5$, PA iterations at $R = 5$ and 10 iterations and IFFT length $N =$ 1024 for 10^5 frames. This result quantifies the PA PAM-DMT PAPR reduction gain compared to the conventional PAM-DMT scheme. For instance, at a CCDF of 10^{-4}, the PA PAM-DMT yield almost 3 dB compared to the conventional PAM-DMT without PAPR reduction.

To determine the BER performance of PAM-DMT and PA PAM-DMT systems, the time domain signal $x[n]$ of both systems is normalised to unity prior to DAC. Then, the time domain signal is transmitted over a range of different transmit power levels V_{pp}. The system SNR is calculated at different V_{pp} using the CIR at the corresponding V_{pp} as presented in

(5.8). This operation is carried out in the frequency domain at the receiver side after estimating the pilot sequence embedded to the transmitted signal using ML estimator to recover the data phase. The SNR of the PA PAM-DMT system is marginally higher than that of the conventional PAM-DMT for all transmit power levels V_{pp} and and modulation format as shown in Fig. 5.8. The BER calculated from the equalized PAM demodulated symbols and plotted versus its transmit power level V_{pp}.

The BER performance of the system shows that, the PA PAM-DMT BER is marginally better than that of the conventional PAM-DMT for 4-PAM and 8-PAM levels as shown in Fig. 5.9. The BER of both techniques saturates beyond input V_{pp} of 300 mV. The PA technique reduces the high PAPR peaks in PA PAM-DMT system as shown in Fig. 5.6 with system BER performance improvement as illustrated in Fig. 5.9. The system BER approaches an error floor due to the limited number of transmitted symbols and the nonlinearity effect of the light source.
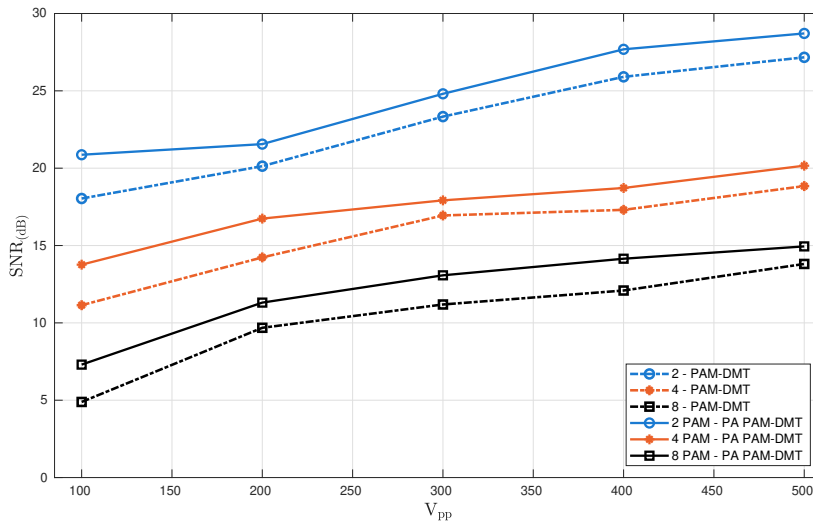
Figure 5.8: *Experimentally measured SNRs of PAM-DMT and PA PAM-DMT at a range of V_{pp} = [100 - 500] mV, sampling rate = 100 MHz and I_{DC} = 20 mA. PAPR reduction at $R = 10$ iterations, $U = 5$ data frames per block, zero padding factor $L = 4$, $N_{\mathrm{subs}} = 127$ active subcarriers and IFFT length N_{IFFT} = 1024.*

The BER performance improvement in the PA PAM-DMT system is a result of reducing the high PAPR peaks which increases the peak-to-peak of the optical modulation amplitude of the signal and minimises the signal distortion from clipping hence, improving the SNR of the system. The SNR of the PA PAM-DMT is marginally higher than that of the basic PAM-DMT
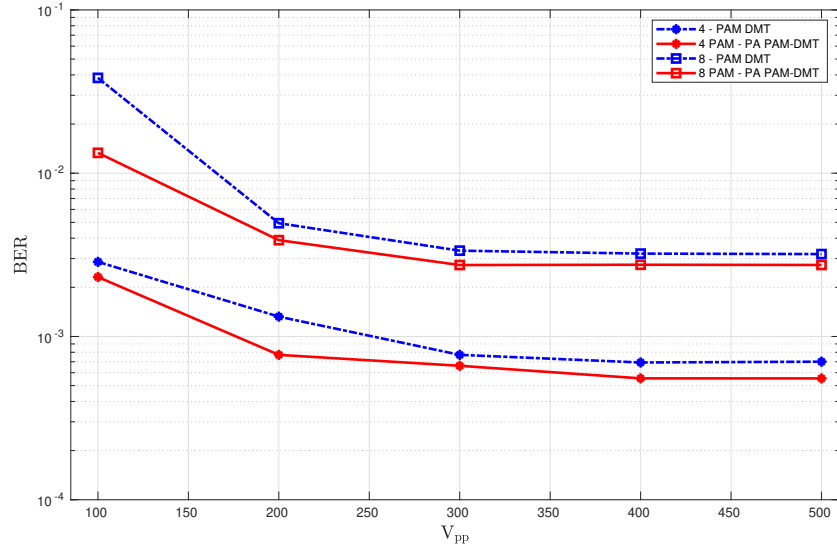
Figure 5.9: *Experimental BER plot for PAM-DMT and PA PAM-DMT using* $[4, 8]$*-PAM,* $U = 5$ *data frames per block,* N_{subs} = 127 *active subcarriers,* $L = 4$ *and IFFT length* N_{IFFT} *of* 1024.

for all given input V_{pp} and modulation orders as shown in Fig. 5.8. This is evident by expressing the SNR in terms of PAPR as shown in (5.12). The system SNR as a function of the signal average power $P_{avg} = \text{E}[x^2(t)] = \sigma_x^2$ is:

$$SNR = \frac{|H_0|^2 \max[|x[n]|^2]}{\sigma_n^2 \times \text{PAPR}} \tag{5.12}$$

where $|H_0|^2$ is the time invariant channel gain and σ_n^2 is the system noise variance which calculated using (5.11) [139]. The system SNR improvement as a function of the system's PAPR reduction as expressed in (5.12). This expression is used to simulate the error performance which is presented in Fig. 5.10, using first order low pass filter and $\sigma_n^2 = 1.1 \times 10^{-5}$. The simulation corroborates the experimental result of Fig. 5.9 that reduced PAPR does improve the BER. However, the nonlinearity effect is not considered for this simulation studies for both compared systems. Hence, the BER in Fig. 5.10 does not approach an error floor as in Fig. 5.9.

Reducing the PAPR of the VLC system allows for higher input power levels for LEDs, increases the system SNR and minimises the non-linearity effects caused by the LED's upper and lower clipping points. In addition, the PAPR reduction has the potential to reduce the transmitted average optical power which results in increasing the reliability of the LED and hence, the
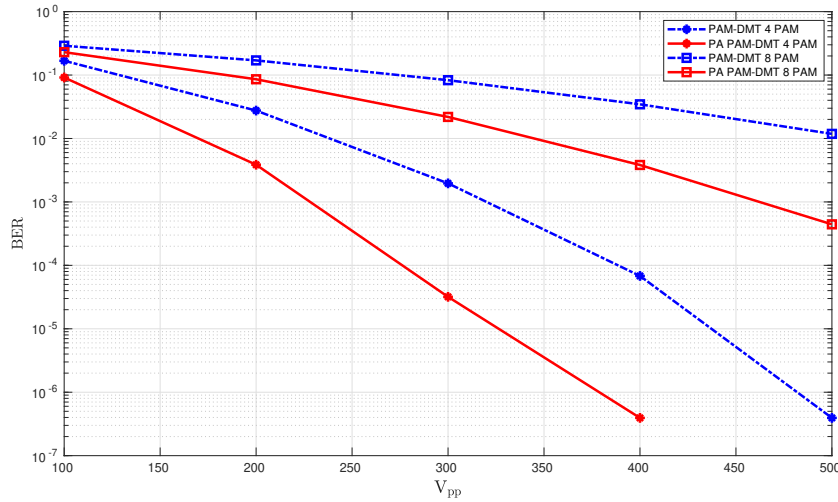
Figure 5.10: *BER simulation of PAM-DMT and PAPR reduced PA PAM-DMT measured at different values of V_{pp}, PAPR reduction at $R = 10$ iterations, upsampling factor $L = 4$, $N_{\mathrm{subs}} = 127$ active subcarriers and FFT length $N_{\mathrm{IFFT}} = 1024$.*

lifetime of the LED.

5.5   System Optimisation

5.5.1   Optical PAM-DMT with Bit and Power Loading

The PA PAM-DMT and PAM-DMT systems are optimised in this section using the experimental setup detailed in Section (5.3). VLC system has frequency-selective channel response which is attributed to the front-end devices frequency-dependent response and the optical channel itself [79]. In PAM-DMT system, the useful information is transmitted on the positive imaginary components of the DMT signal which activates all subcarriers of the frame. Therefore, the PAM constellation format can be allocated adaptively at each subcarrier k to maximise the achievable data rate at a target BER. Thus, the VLC channel response and SNR per subcarrier SNR_k are estimated to allocate a suitable PAM constellation size to each subcarrier k based on the Levin-Campello algorithm [140]. This allows for higher modulation formats to be used for the subcarriers with higher SNR while ensuring that, the error probability P_e^T, is kept below the FEC target of 3.8×10^{-3} [79]. In addition, the algorithm allows more power to be allocated to the subcarriers that require additional minimal energy to be elevated into higher constella-

tion size while preserving the P_e^T. The adaptive bit and power loading based on [140], can be formulated to optimise the following problems on each active subcarrier k [28]:

$$\text{maximise} \quad b_k = \log_2 M_k \tag{5.13a}$$

$$\text{subject to} \quad \text{BER}(M_k, \text{SNR}_k) \leq P_e^T \tag{5.13b}$$

$$\sum_{k=1}^{\frac{N}{2}-1} \nu_k^2 = N_{\text{subs}} \tag{5.13c}$$

where b_k is the number of bits per symbol with $b_k > 2$ bits and ν_k^2 is the power loading factor. $\text{BER}(\text{M}_k, \text{SNR}_k)$ is the theoretical BER equation of M_k-PAM at subcarrier k at corresponding SNR_k and can be approximated by the following [120]:

$$\text{BER}(M_k, \text{SNR}_k) \approx \frac{2}{\log_2 M_k} \times \left(1 - \frac{1}{M_k}\right) \times \sum_{l=1}^{\min(2,\sqrt{M_k})} Q\left((2l-1)\sqrt{\frac{6 \times \text{SNR}_k}{M_k^2 - 1}}\right) \tag{5.14}$$

where $Q(\cdot)$ is Gaussian Q-function. The overall data rate, R_b, of the bit and power loaded system can be calculated by [79]:

$$R_b = \frac{\sum_{k=1}^{\frac{N}{2}-1} \log_2 M_k}{(N + N_{\text{CP}})/2B} \tag{5.15}$$

where B is the single-sided modulation bandwidth of the system, and N_{CP} is the CP size. The $N_{\text{CP}} = 5$ is found to be sufficient for ISI mitigation in this experimental study.

5.5.2   End-to-End Link Characterisation and Optimisation

The VLC system transmitter is a blue LED as mentioned in the experimental setup in Section (5.3). The LED driving current point (I_{DC}) is a very important parameter which determines the available signal amplitude range and the distortion caused by the LED non-linearity and system frond-end devices clipping [79]. Hence, measuring the effect of driving current points

of the LED is essential to find and select the optimum point for data transmission. This is accomplished by measuring the optical power of the LED at different bias current points by placing a Photo-diode Power Sensor (S120C) with Optical Power Meter (PM100USB) at the receiver side over a distance of 1 m. The received optical power at current points range [2-150] mA is measured and shown in Fig. 5.5b with the corresponding voltage in Fig. 5.5a. It shows that the highest received optical power appears to be at 130 mA. However, this bias current point is not necessarily to be the optimum point. Therefore, measuring the system data rate at I_{DC} points range is essential process to find the optimum I_{DC} value while ensuring that the P_e^T, is kept below the predefined FEC target of 3.8×10^{-3}. This process is carried out by transmitting an OFDM signal using the system parameters mentioned in Section 5.4, at modulation bandwidth which is chosen to be low by using sampling frequency of 200 MSa/s for the AWG. Note that AWG, (Keysight 81180A) and oscilloscope, (Keysight MSO-X3104T) are used in the optimisation and data transmission of this section. The minimum stable voltage V_{pp} for the AWG is found to be 200 mV. The selection of this parameter is to ensure system's stability and to eliminate any possible distortion caused by other parameters. The highest data rate is achieved at $I_{DC} = 20$ mA as shown in Fig. 5.11. The system shows a satisfying BER level below a predefined BER target of 3.8×10^{-3}. Selecting the driving bias current point I_{DC} of the LED allows for non-linear distortion minimisation and system's SNR maximisation.
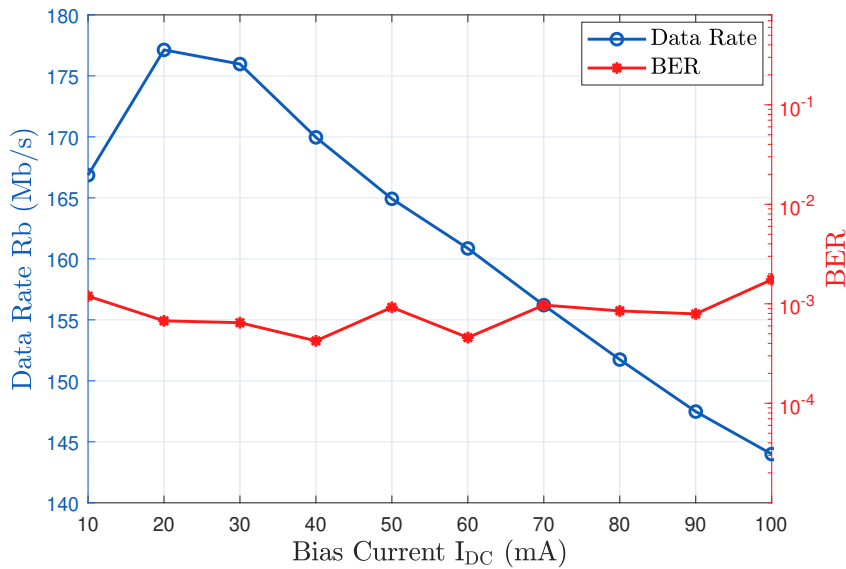
Figure 5.11: *Data rate Rb and BER at LED's Bias current I_{DC} points at 200 mVpp and 200 MHz sampling rate.*

At the optimum I_{DC} point, the transmitted signal can be scaled to fit the linear region of the LED by adjusting its maximum V_{pp} voltage at the AWG prior to the transmission. This performed by fixing the above mentioned parameters including the I_{DC} at its optimum value, then increase the V_{pp} gradually and measure the system data rate and its corresponding BER. This process shows that, the optimum V_{pp} value is found to be 450 mV, where the highest data rate is achieved as shown in Fig. 5.12, while the BER level is below the predefined FEC target.
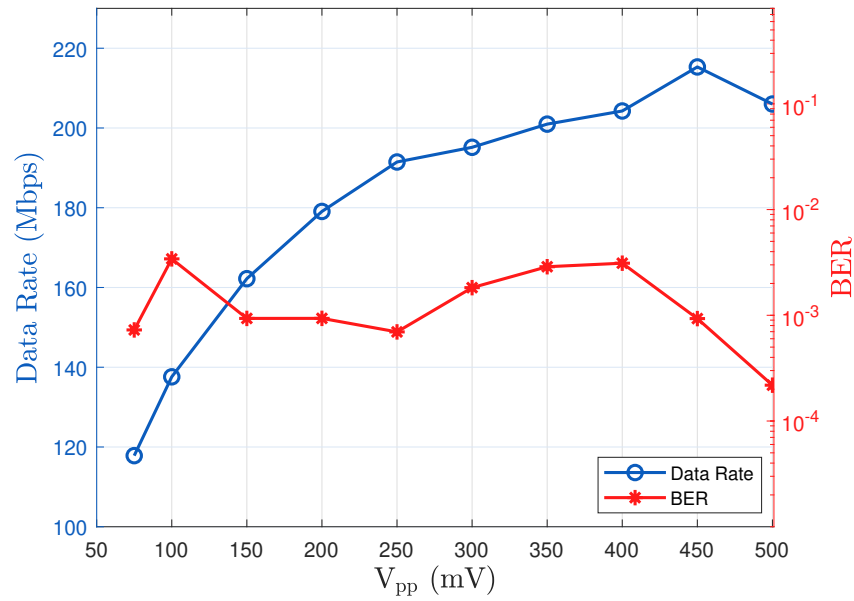
Figure 5.12: *Data rate and BER at V_{pp} values and I_{DC} = 20 mA and sampling rate of 200 MSa/s.*

At the optimum I_{DC} and V_{pp} values the 3 dB bandwidth of the used LED is 11.7 MHz as shown in the LED's frequency response in Fig. 5.13.

5.5.3 Optimised Link Performance

Fig. 5.14 compares the experimental BER of PA PAM-DMT and conventional PAM-DMT at varied transmission rates and the optimisation process detailed in Section 5.5. The PA scheme results in improved system BER. This is due to the PAPR reduction which minimises the clipping noise and distortion level in the system. Consequently, the system SNR is improved and hence enhanced the BER performance. At higher transmission rates, far beyond what the available link bandwidth can support, severe distortion in the system causes error in the PA
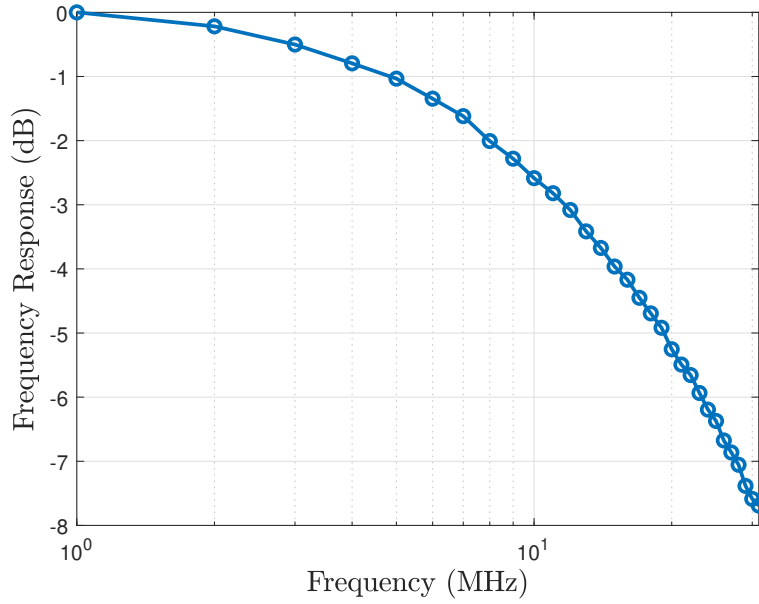
Figure 5.13: *LED frequency response at optimum values of I_{DC} and V_{pp}.*

pilot sequence estimation. This is shown to result in the BER of PA system approaching that of the conventional system with no PAPR reduction. The results demonstrate that the PA PAPR reduction approach can be used to improve the system performance while retaining the high transmission rate capability of the PAM-DMT system.
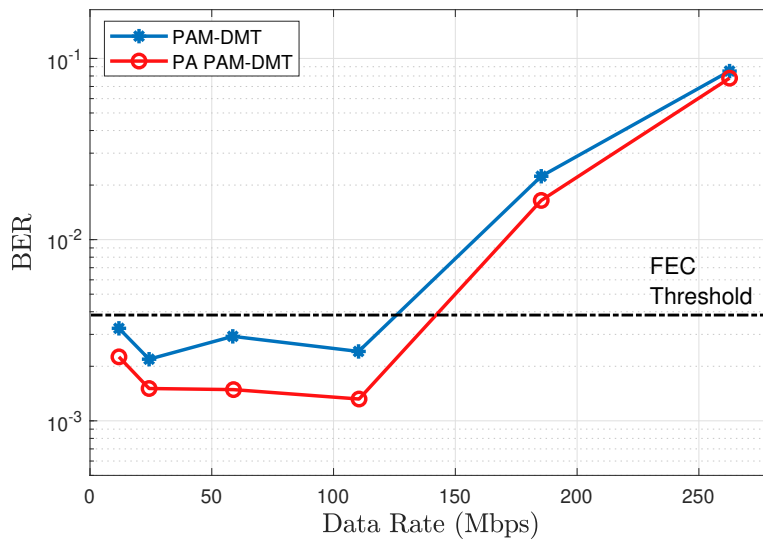
Figure 5.14: *Experimental BER and data rate of PA PAM-DMT and PAM-DMT with bit and power loading.*

5.6   Summary

The high PAPR of the time domain signal of PAM-DMT $x[n]$ is studied and reduced using PA technique in PA PAM-DMT. The number of iterations R can be modified to obtain different levels of PAPR reduction i.e. a gain of 2.75 dB is achieved by $R = 10$ pilot iterations. This PAPR reduction is obtained with BER performance improvement. The SNR of the proposed scheme is higher than that of its counterpart. This is proven in an experimental proof-of-concept study for PA PAM-DMT system and compared with PAM-DMT system over a VLC channel. In addition, PA scheme is used to reduce the PAPR of PAM-DMT in VLC system, improve the error performance without data rate degradation. The achieved BER and SNR enhancement by the PA scheme can be traded for longer range and/or higher data rate transmission compared to the conventional system with no PAPR reduction. Furthermore, the PA scheme has the potential to reduce the transmitted average optical power, resulting in increased reliability and lifetime of the LED.

Chapter 6

PAPR Reduction in O-OFDM based WDM VLC System

6.1 Introduction

In this chapter, the effect of reducing the high PAPR in DCO-OFDM and PAM-DMT based WDM VLC system is studied experimentally in terms of achievable data rate and BER. Experimental demonstration of PA DCO-OFDM and PA PAM-DMT based WDM VLC using three different low-cost off-the-shelf LEDs is investigated and presented. WDM system is utilised to efficiently modulate the three different wavelengths. DCO-OFDM and PAM-DMT are considered in this study and due to their high PAPR peaks and the limited dynamic range of VLC front-end devices, the PA technique is applied to reduce their high PAPR. The reduction of PAPR minimises the signal clipping and nonlinearity distortion caused by the optical source. Furthermore, each wavelength available bandwidth is utilised using adaptive bit and power loading.

MCM techniques such as DMT modulation variants are regarded as convenient modulation candidates for VLC systems. This is due to their advantages such as simplified equalisation process, multi-path propagation resilience, ISI mitigation and robustness against channel frequency selectivity [26–28].

Different DMT modulation variants have been proposed for the VLC systems such as DCO-OFDM, ACO-OFDM and PAM-DMT. DCO-OFDM is a widely used modulation scheme for VLC system due to its high spectral efficiency when compared to other DMT techniques [106]. In addition, the light sources such as LEDs require DC current I_{DC} to turn them on which already exists in DCO-OFDM for unipolar waveform conversion purpose [26]. Moreover, using DCO-OFDM in VLC offers an efficient use of the limited modulation bandwidth of illumination LEDs used in VLC [107]. However, DC bias is required to create the unipolar signal which results in significant energy losses [106]. ACO-OFDM and PAM-DMT systems are proposed in [108] and [33] respectively. In ACO-OFDM and PAM-DMT systems, the properties

of Fourier transformation are used to exploit the frame structures. Therefore, the time domain signal is clipped at the zero level to realise the unipolar signal and the DC bias is required only to turn on the light source which makes them power efficient techniques [27]. However, the spectral efficiency of these schemes is half of the spectral efficiency in DCO-OFDM [109].

Despite MCM techniques advantages, they are affected by high PAPR peaks. Various solutions have been proposed to address the PAPR challenge. PA technique is implemented in this work for PAPR reduction. PA technique is an effective solution for the PAPR reduction in optical OFDM systems which was proposed in [26]. PA technique rotates the data frame phase by a randomly generated pilot in order to avoid coherent addition of the subcarriers as much as possible. The pilot symbol's phase is chosen based on the SLM algorithm while the ML algorithm is used to recover the pilot phase at the receiver side [65]. Implementation details of the PA technique in O-OFDM and its PAPR reduction gain in DCO-OFDM and PAM-DMT based VLC system is presented in this chapter.

Specific contributions of this chapter are as follows:

- Experimental demonstration of a PAPR reduction using PA scheme in PA DCO-OFDM and PA PAM-DMT based VLC system.

- For the first time, the PA technique is applied to a WDM based VLC system to reduce clipping/nonlinear distortion, and maximise achievable data rate while maintaining error performance.

- Evaluation of PA DCO-OFDM system's data rate and BER per wavelength and then compared to that of conventional DCO-OFDM without PAPR reduction.

- Evaluation of PA PAM-DMT system's data rate and BER per wavelength and then compared to that of conventional PAM-DMT without PAPR reduction.

The PA DCO-OFDM and PA PAM-DMT based WDM VLC system have achieved more than 8% data rate higher than that of their conventional counterparts without BER degradation.

6.2   Experimental Test-Bed for WDM System

6.2.1   Optical Pilot-assisted based WDM DMT

Different OFDM modulation variants have been proposed for VLC systems i.e. DCO-OFDM and PAM-DMT. In this chapter, DCO-OFDM and PAM-DMT with PAPR reduction are considered for this study. Conventional OFDM waveform is complex and bipolar. However, the IM/DD requirement can be met by imposing Hermitian symmetry on the DMT subcarriers frame which results in real-valued DMT waveforms, $X[k] = X^*[N-k]$, where N is the DMT frame length, and k is the subcarrier index. In the frequency domain, subcarriers at $X[0]$ and $X[N/2]$ are assigned to zero values. In DCO-OFDM, DC bias is used to convert most of the negative real-valued into positive samples. However, in PAM-DMT the DC bias is required only to turn on the light source.

In DMT system based WDM VLC, the available modulation bandwidth of the light source results in SNR response variation, which restricts the assigned constellation size and leads to spectral efficiency losses. To overcome this, larger constellation format can be assigned on the subcarriers that have higher SNR. Therefore, the spectral efficiency can be maximised by bit and power loading algorithm. This is achieved by estimating the available SNR per subcarrier (SNR_k). To generate the real-valued DMT signal, a random bit sequence generation for each light source of the WDM system is performed off-line in MATLAB as shown in the transmitter's DSP (Tx-DSP) of the system block diagram in Fig. 6.2 in the case of DCO-OFDM, and Fig. 6.3 for the case of PAM-DMT. Primarily, estimation of the VLC channel response and the available SNR_k of each light source (LED) is performed by multiple OFDM frames. This estimation is obtained by the error vector magnitude (EVM) method [141]. Given the estimated SNR_k, QAM constellation size per subcarrier (M_k) is adaptively allocated into subcarrier k with its corresponding relative energy, ν_k^2, based on the Levin-Campello Algorithm [140]. The constellation format and power adaptive allocation are performed based on a predefined error probability target P_e^T. This allows for higher modulation formats to be loaded into the subcarriers with higher SNR while ensuring that, the error probability P_e^T is kept below a FEC target of 3.8×10^{-3} [79]. In addition, the algorithm allows for more power to be loaded into the subcarriers that required additional minimal energy to be elevated to higher constellation format while preserving the P_e^T. The adaptive bit and power allocation can be formulated to optimise the problems on each active subcarrier k as mentioned in (5.13) [28].

$\mathrm{BER}(\mathrm{M}_k,\ \mathrm{SNR}_k)$ is the theoretical BER equation of M_k-QAM at subcarrier k with the available corresponding SNR_k and can be approximated by the following [28]:

$$\mathrm{BER}\left(M_k, \mathrm{SNR}_k\right) \approx \frac{4}{\log_2(M_k)} \times \left(1 - \frac{1}{\sqrt{M_k}}\right) \times \sum_{l=1}^{2} Q\left((2l-1)\sqrt{\frac{3 \times \mathrm{SNR}_k}{M_k - 1}}\right) \quad (6.1)$$

where $Q(\cdot)$ is the Gaussian Q-function. The $\mathrm{BER}(\mathrm{M}_k,\ \mathrm{SNR}_k)$ is the theoretical BER equation of M_k-PAM at subcarrier k at corresponding SNR_k and can be approximated as presented in (5.14) [120]. The overall data rate, R_b, of the bit and power allocation system per wavelength can be calculated as evaluated in (5.15) [79].

The allocated bits and power based on the available SNR_k per light source (LED) are mapped into QAM symbols in DCO-OFDM system case, while mapped in PAM symbols in the case of PAM-DMT system. The QAM symbols are then transformed from serial to parallel to form columns of active subcarriers length N_{subs}. Then the Hermitian symmetry is imposed to the QAM symbols and loaded into orthogonal subcarriers of length N with subcarrier spacing equal to the symbol duration. Due to the high PAPR peaks of the time domain waveform, the PAPR is reduced using PA scheme as detailed in Section (6.2.2), in the frequency domain. The symbols are then multiplexed into a time domain signal by size N IFFT followed by CPs insertion. In the case of PAM-DMT the time domain signal is clipped at zero level for unipolar transformation purpose and transmit the imaginary part only as detailed in 5.2.1. This is followed by up-sampling process then PAPR reduction evaluation and parallel to serial conversion prior to a pilot signal insertion for synchronisation purposes for each wavelength waveform.

At the receiver side, the off-line receiver's (Rx-DSP) part is illustrated in the system block diagram in Fig. 6.2 for the DCO-OFDM system, and Fig. 6.3 for the PAM-DMT system. The received waveforms are processed with synchronisation then down-sampling processes followed by serial to parallel conversion, and CPs removal. A FFT operation is then applied to each waveform which provides the QAM/PAM symbols in the frequency domain. The QAM/PAM symbols carrying data are then extracted from the PA embedded pilots. The phase and amplitude of the embedded PA pilots are estimated based on the ML technique. The estimated pilots phases are used to recover the phase of the corresponding received data QAM/PAM symbols. A prior estimated channel response of each light source is used to equalise the corresponding signal based on the single-tap zero-forcing equalisation process. The equalised signals are QAM/PAM demodulated, followed by BER calculation based on the demodulated binary

streams.

6.2.2   WDM-VLC System with PAPR Reduction

DCO-OFDM and PAM-DMT systems are a spectral efficient and power efficient optical DMT variants respectively. This is results of that, DCO-OFDM requires DC bias to produce an unipolar signal for intensity modulation. While, in PAM-DMT the DC bias is required only to turn on the used LEDs. Furthermore, the spectral efficiency of PAM-DMT is half that of the DCO-OFDM at the same modulation format [7]. However, the DCO-OFDM and PAM-DMT waveforms comprise of the sum of independent subcarriers in the time domain which results in individual subcarriers added up coherently to produce high PAPR [34]. Consequently, high electrical peaks must be clipped at lower and/or upper levels to contain the signal swing inside the dynamic range of the light source [35]. The high electrical PAPR values must be reduced to benefit from the dynamic range of the optical light source in full. Reducing the high PAPR values will help the light source to operate inside its linear dynamic region and hence, reduces the clipping distortion of the transmitted signal caused by the frond-end devices of the system [26].

To address the PAPR problem, the pilot assisted (PA) technique is applied to reduce the high PAPR values of the system. PA rotates the phase of individual subcarriers to avoid the possibility of them added up coherently. The implementation process of PA for DCO-OFDM based VLC WDM system is described in this section while, it is described in Section (5.2.2) for the PA in PAM-DMT system. The electrical PAPR values of the time domain signal is defined in (5.4) [26].

The procedure of PAPR reduction using PA technique in DCO-OFDM is described as follows [26]:

- Group the frequency domain frames of DCO-OFDM into U blocks comprise of active subcarriers N_{subs}; where, $X^u[k]$, $u = 1, 2, \ldots, U$.

- Generate R multiple iterations of pilot sequence candidates with N_{subs} length, X_{p}^r, where $r = 1, 2, \ldots, R$.

- Select the sequence X_{p}^r amplitude $A_{\text{p}}[k]$ to be ± 1 only.

- Randomly set the pilot sequence phase $\theta_{\text{p}}[k]$ to 0 or π values only, where $k = 1, 2, \ldots, N_{\text{subs}}$.

- Rotate the block U phase by $\theta_{\mathrm{p}}[k]$ of every pilot iteration r.

- Calculate the PAPR$_r$ value of iteration X_{p}^r.

- Select the pilot iteration $X_{\mathrm{p}} = X_{\mathrm{p}}^{\tilde{r}}$ with minimum PAPR value for transmission; where [35],

$$\tilde{r} = \operatorname*{argmin}_{1 \leq r \leq R} (\mathrm{PAPR}_r) \tag{6.2}$$

- Embedded the pilot sequence $X_{\mathrm{p}}[k]$ into the corresponding block U of frames for high PAPR reduction, and thus the number of frames per block U will be $\hat{U} = (U + 1)$.

The high PAPR peaks of each LEDs is reduced where the DCO-OFDM number of frames are grouped to form a block U, and $U = 5$ frames per block. This value is selected because the PAPR increases as U increases [26]. The considered number of iterations are selected to $R = 10$ iterations because it shows a good trade off between performance and complexity [135]. CP is not used during the PAPR evaluation as it has negligible impact on the PAPR results. At the receiver, the received PA sequences are extracted from the data blocks, then estimated using ML technique. The ML technique is used in this work as presented in Section (5.2.2) [26]. At the receiver, the received PA sequences are extracted from the data blocks, then its noise corrupted phase $\hat{\theta}_{\mathrm{p}}[k]$ is estimated using ML technique to improve the data recovery. The estimate of the angle is taken between two values, ($\hat{\theta}_i = 0$ and π) that has the minimum Euclidean distance from the received pilot's phase $\tilde{\theta}_{\mathrm{p}}$. The estimate argument is expressed in (5.6) and (5.7). In addition, the pilot's sequence amplitude, $\hat{A}_{\mathrm{p}}[k]$ is maintained to unity using the condition given in (5.7). The estimated PA phase $\hat{\theta}_{\mathrm{p}}[k]$ with recovered amplitude, $\hat{A}_{\mathrm{p}}[k]$, is then used to recover the phase of the corresponding subcarrier k for the corresponding block U of the received data.

The systems' PAPR reduction gain using PA scheme is shown in Fig. 6.1 for PA DCO-OFDM, and in Fig. 5.6 for PA PAM-DMT. This results quantify the PAPR reduction gain compared to the conventional DCO-OFDM and PAM-DMT scheme respectively. For instance, at a CCDF of 10^{-4}, the PA DCO-OFDM yield almost 3.5 dB compared to the DCO-OFDM as illustrated in Fig. 6.1. The PA PAPR reduction gain in PAM-DMT is shown in Fig. 5.6, and discussed in Section (5.4).
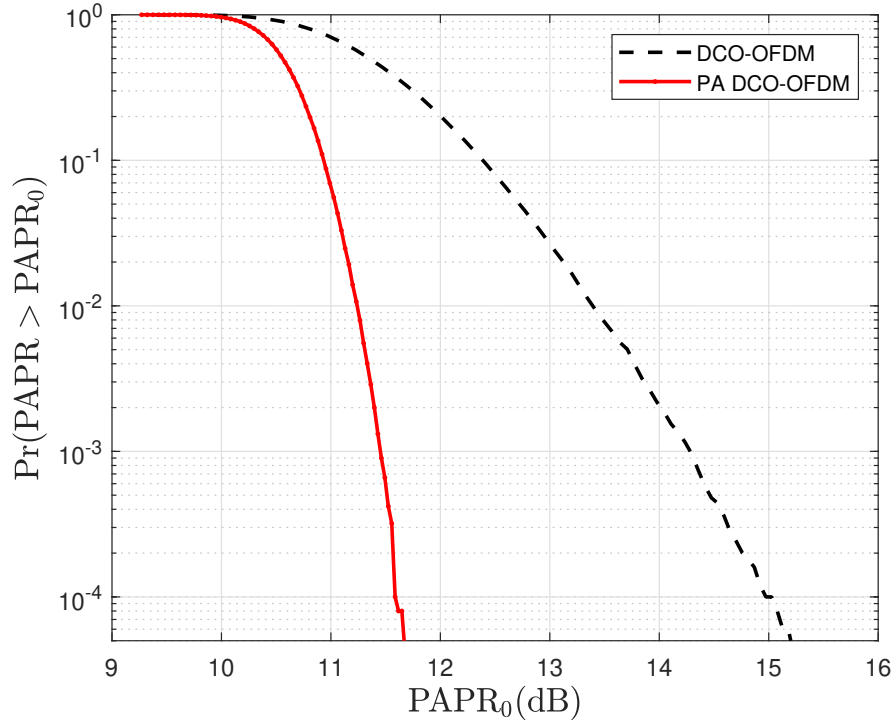
Figure 6.1: *PAPR CCDF plot for PA DCO-OFDM and DCO-OFDM using N_{subs} = 1023 active subcarriers, 16-QAM, up-sampling factor = 16, U = 5 data frames per block and PAPR reduction at R = 10 iterations.*

6.3   Experimental Demonstration of PA in WDM VLC systems

6.3.1   Experimental Setup

The experimental setup details are presented in this section. The WDM system is considered for this work which uses three different single colour LEDs for the PAPR reduced PA DCO-OFDM and PA PAM-DMT transmissions. The WDM light sources are selected from Dialight with three different colours (wavelengths) namely, red (R), green (G) and blue (B). The module numbers of the RGB LEDs are Red: 598-8D10-107F, Green: 598-8081-107F and Blue: 598-8D90-107F with dominant wavelengths of 635 nm, 525 nm and 470 nm respectively [142]. The RGB single colour beams are combined at the transmitter side (Tx) by two Thorlabs dichroic mirrors that are dependent on the incident light wavelength. The light beams are separated at the receiver side (Rx) using two similar dichroic mirrors as an optical bandpass filter as shown in the system block diagram in Fig. 6.2.
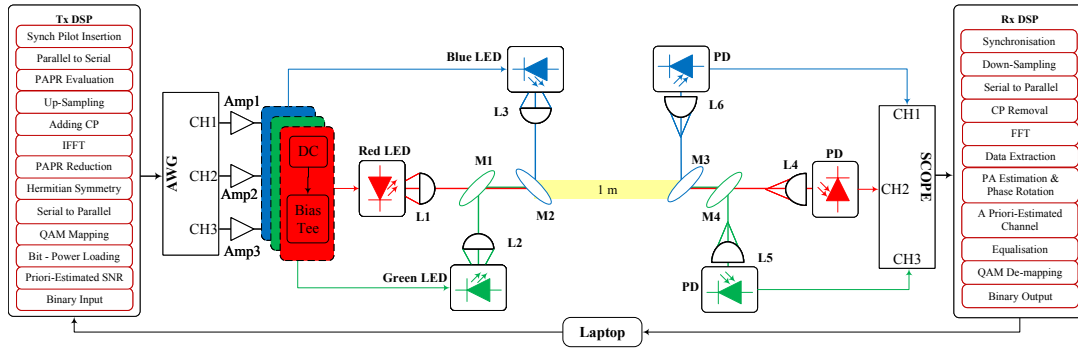
Figure 6.2: *PA DCO-OFDM experimental setup block diagram.*

The experimental setup starts with generation of DMT signals for each wavelength of the WDM system as detailed in section (6.2.1) for DCO-OFDM system and section 5.2.1 for PAM-DMT system. The generated digital signal is then loaded to a AWG (Keysight M8195A) for digital to analogue conversion. The sampling rate of the AWG is set to 16 GSa/s. Each AWG output is amplified by an amplifier (Mini-Circuits ZHL-1A-S+). Each amplified signal is then fed into a bias-tee (Mini-Circuits ZFBT-4R2GW). The amplified bipolar information signal is then superimposed with the DC-bias. Low DC bias values result in large zero-level clipping of the signal which degrades the system performance. High DC bias values cause upper level clipping of the waveform and optical power saturation at the LEDs which results in system performance degradation. As a result, DC bias optimisation is required for each wavelength to avoid system performance deterioration. Therefore, the optimum DC bias point of each LED is evaluated as detailed in Section (6.4). The bias-tees outputs are then connected to the corresponding LEDs for intensity transmission over a free space channel. The half power angles of the selected LEDs are wide (i.e. $70°$), therefore, aspheric condenser lenses (L1-3: Thorlabs ACL50832U-A) are used at the output of each LED to collimate its light into a set of dichroic mirrors (M1 and M2). The dichroic mirror (M1: Thorlabs DMLP567L) has a transmission band of 584-800 nm and cut-off wavelength of 567 nm. This mirror is used to pass the light of the red LED and reflects the output of the green LED into the transmission path. The second dichroic mirror (M2: Thorlabs DMLP490L) has a transmission band of 505-800 nm with cut-off wavelength of 490 nm. M2 is used to pass the red and green LEDs' lights while reflecting the light of the blue LED. The LEDs' lightwaves are combined by the dichroic mirrors into a single beam and transmitted simultaneously over the channel for a distance of $d = 1$ m.

At the receiver, the same setup configuration of the mirrors is used to separate the received light intensity of the three LEDs as shown in the receiver side of the system block diagram in Fig.

6.2. Two different dichroic mirrors are used in the path of the received light beam to direct the light intensity of each LED into the desired wavelength region. The first mirror (M3) is similar to (M2) which reflects the blue LED light to its corresponding receiver while passes the red and green lights through. Similar to (M1), another mirror (M4) is used to pass the red LED light towards its receiver while reflects and directs the green wavelength towards its desired receiver. Each LED wavelength is then focused into the desired receiver detection area by an aspheric condenser lens (L4-L6). The selected receivers are PIN PDs (New Focus 1601 AC) with a 3 dB bandwidth of 1 GHz each. The PDs convert the incoming optical radiations into electrical current signals. Each PD has a built-in TIA with a gain of 10 V/mA, which converts the received current signal into a voltage signal. Then, the received signals are captured by a high speed oscilloscope (OSC: Keysight MSO-X 3104T) and sent back to MATLAB for off-line processing as shown in the off-line receiver's (Rx-DSP) part of the system block diagram in Fig. 6.2 for PA DCO-OFDM, and Fig. 6.3 in the case of PA PAM-DMT. In the receiver DSP domain, each waveform is synchronised and down-sampled. This followed by the CP removal and FFT operation which provides the QAM/PAM signals in the frequency domain. The carrying information subcarriers are extracted and the phase and amplitude of the embedded PA pilots are estimated using ML technique. In the case of PA PAM-DMT system, The imaginary part of the subcarriers is only considered, while the real part is ignored. Moreover, the signal is scaled by a factor of 2 to preserve the overall signal energy due to the energy loss caused by clipping at zero-level at the transmitter side. The pilots estimated phases are used to recover the corresponding received subcarriers phase. This process is followed by the equalisation and QAM/PAM demodulator processes in the DSP domain. The BER of each LED is then evaluated from the QAM/PAM demodulated symbols. Details of each system off-line DSP are presented in Fig. 6.2 for PA DCO-OFDM, and Fig. 6.3 in the case of PA PAM-DMT.

6.3.2 DC Bias Points Optimisation

The experimental data transmission in this work is WDM based VLC system using three single colour LEDs (RGB) in the visible light spectrum. The driving bias current (I_{DC}) of each LED is optimised. The 3-dB of each wavelength is commonly proportional to the input current I_{DC} of each LED as shown in Fig. 6.4. However, this can drive the light source into the nonlinear region of its dynamic range. The I_{DC} of LEDs determine the output optical power and the achievable data rates. Therefore, the optimum I_{DC} points of the used LEDs are found where the amount of nonlinear distortion is minimised and the available SNR is maximised for each
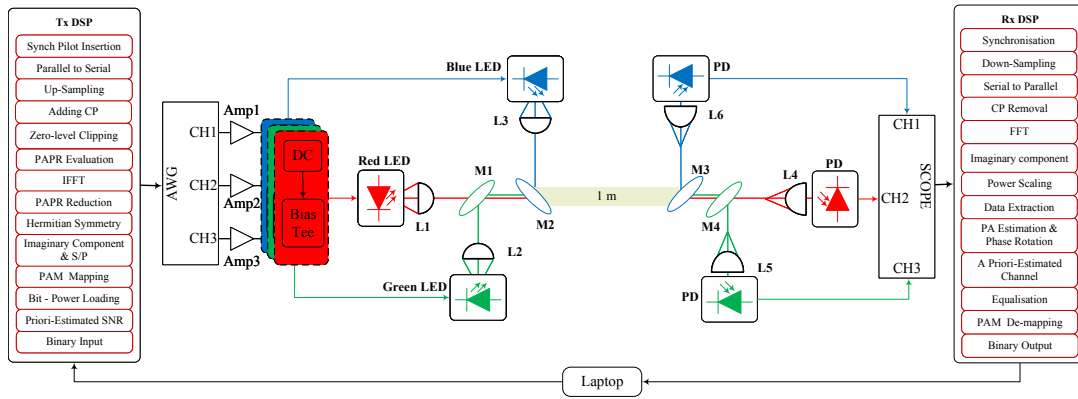
Figure 6.3: *PA PAM-DMT experimental setup block diagram.*
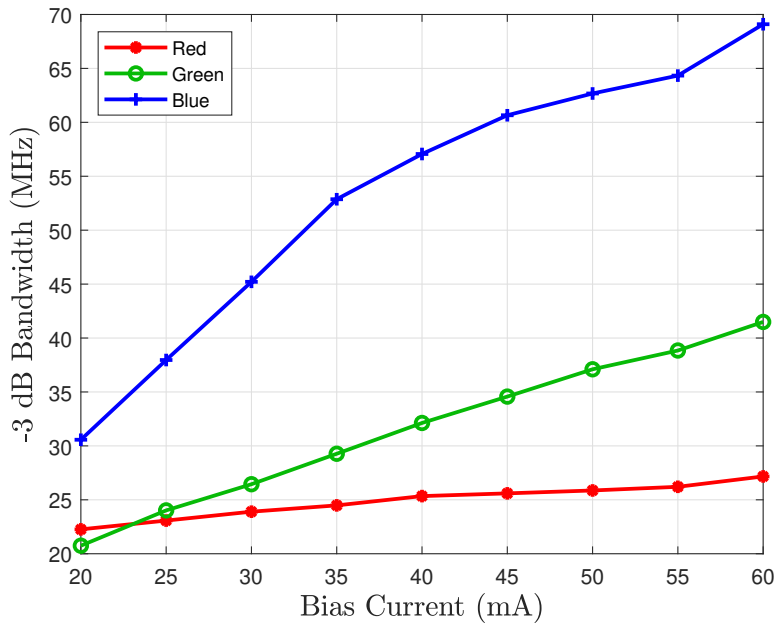
Figure 6.4: *The measured LEDs' 3-dB versus bias current (I_{DC}).*

LED. Selecting the I_{DC} points allows for scaling the transmitted signal to fit the linear dynamic region of each LED. The selected LEDs are assumed to be the main nonlinearity source in the overall system due to their limited dynamic ranges compared to the other system components.

The optimisation process starts with selecting the driving bias current point I_{DC} of each LED using the system experimental setup in section (6.3.1). The available channel bandwidth and SNR at each subcarrier, SNR_k, per wavelength are estimated by transmitting multiple pilot frames of 4-QAM based optical OFDM. The available SNR_k of received pilot frames is esti-
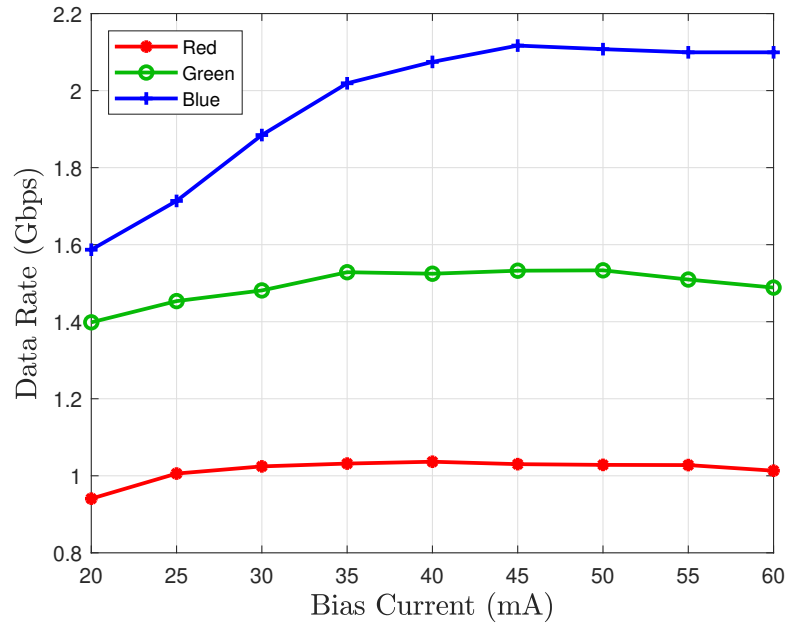
Figure 6.5: *The system measured data rates versus bias current (I_{DC}) for optimisation process.*

mated by EVM method [141]. The I_{DC} per wavelength is selected to minimise LEDs nonlinearity effect and maximise the available SNR_k, and as a result, increase the achievable data rate per wavelength.

The following parameters are used for the system optimisation processes: the data symbol rate R_s is set to 1 GBaud and with oversampling factor L of 16 samples per symbol, the WDM data transmission is performed at a 16 GSa/s sampling rate per wavelength. The number of data carrying subcarriers, N_{subs} is set to 1023. The OFDM frame length, (IFFT/FFT) size, is set to $N = 2048$ subcarriers to utilise the available modulation bandwidth of each light source. The CPs with adequate size is then inserted at the start of each OFDM frame to efficiently eliminate the ISI by single-tap equalizer. A CP size of $N_{CP} = 5$ is found to be sufficient for ISI removal at spectral efficiency loss of less than 0.20%. To optimise the driving bias current point (I_{DC}), the V_{pp} of the AWG is set to its minimum possible value which is found to be 75 mV, to avoid LEDs nonlinearity effect. Next, the I_{DC} is increased gradually, and the data rate of the system is measured for each LED. The optimum I_{DC} values for the red and blue LEDs are found to be 45 mA, while for the green LED is 50 mA as shown in Fig. 6.5.
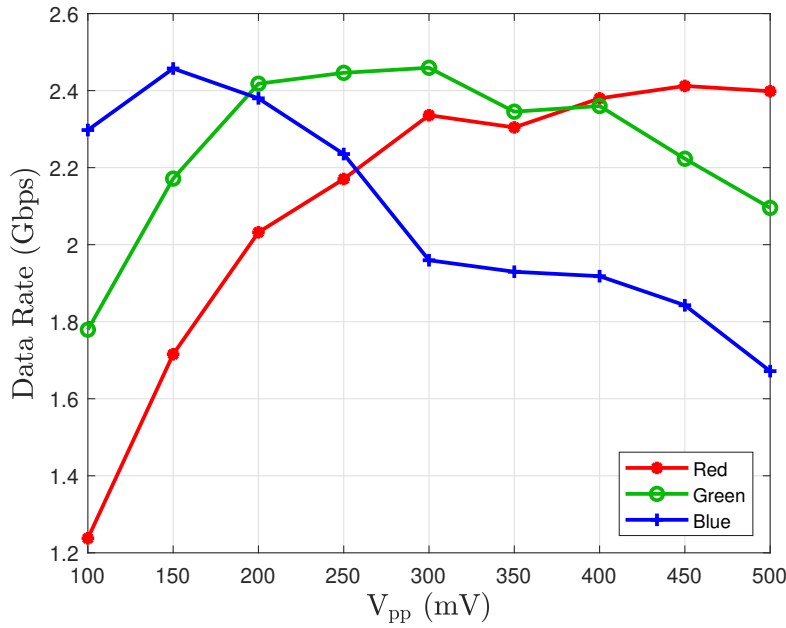
Figure 6.6: *The system measured data rates versus signal depth (V_{pp}) for optimisation process. The optical power dissipation is 72 mW for the Red LED, 102 mW for the Green LED and 70 mW for the Blue LED.*

6.3.3 Signal Depth Levels Optimisation

The measured I_{DC} points are used to find the optimum peak-to-peak voltage V_{pp} values for each selected LED. The modulation signal depth, V_{pp} of each waveform is performed at the AWG output by adjusting the V_{pp} of each LED. The optimum V_{pp} points are found by increasing its value gradually and measuring the data rate for each LED at the found optimum I_{DC} points which are mentioned in Section 6.3.2. The optimum V_{pp} values are found to be as follows: 450 mV for the red LED, 300 mV for the green LED and 150 mV for the blue LED as shown in Fig. 6.6. The optimum I_{DC} points and V_{pp} values for each LED are used to estimate the available SNR_k at subcarrier k based on the channel gain at subcarrier k as shown in Fig. 6.7. The available measured SNR_k determines the QAM/PAM modulation format and corresponding power to be loaded adaptively at the subcarrier k for each LED. In the setup, the I_{DC} and V_{pp} values are optimised for conventional DCO-OFDM and PAM-DMT systems then applied directly to PA DCO-OFDM and PA PAM-DMT for comparison. As a result, the highest possible data rates are achieved per wavelength for the used equipment, setup and parameters.
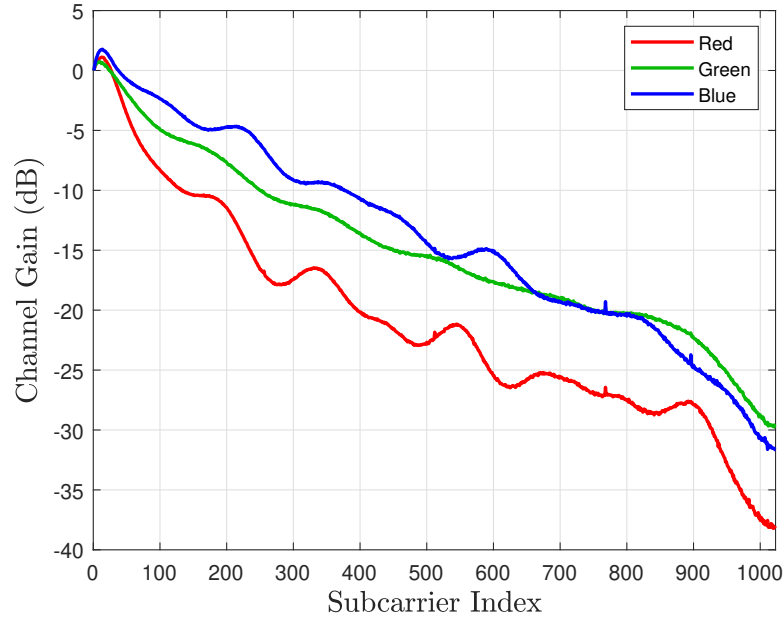
Figure 6.7: *The LEDs' channels gain per subcarriers of the optimisation process.*

6.4 Data Transmission Results and Discussion

6.4.1 Single LED High-speed VLC System

In this section, a single blue LED is used for experimental demonstration of a PAPR reduced DCO-OFDM system with bit and power allocation algorithm. DCO-OFDM is considered for this study including the DCO-OFDM system description with bit and power loading in Section 6.2.1. The real-valued OFDM signal is generated for the intensity modulation transmission using N_{subs}, zero padding factor $L = 4$, data frames per block $U = 5$, PA iterations at $R = 10$ iterations and IFFT length $N = 1024$. The rest of the system parameters are defined in Section (5.4). The QAM modulation formats per subcarrier k of the OFDM frame are selected based on the available estimated SNR_k and the VLC channel response of the used LED. This estimation is performed by multiple of 4-QAM OFDM frames and obtained by EVM algorithm [141]. Given the estimated SNR_k, QAM constellation size per subcarrier (M_k) is adaptively allocated into subcarrier k with its corresponding relative energy, ν_k^2, based on the Levin-Campello Algorithm [140]. The QAM format and power adaptive allocation are obtained based on a pre-defined probability target P_e^T of 3.8×10^{-3} [79]. This process is detailed in Section (6.2.1). Then, the PAPR of the time domain signal of DCO-OFDM is reduced by PA as detailed in Section (6.2.2), and the PAPR reduction gain is illustrated in Fig. 6.8. The system is optimised

for the experimental setup of the single blue LED VLC system shown in Fig. 5.2, using the experimental setup process detailed in Section (5.3). Note that AWG, (Keysight 81180A) and oscilloscope, (Keysight MSO-X3104T) are used in the optimisation and data transmission of this section. The data transmission is carried out at the selected optimum I_{DC} input current of 20 mA, and $V_{pp} = 450\,\mathrm{mV}$ using the system equipments and optimisation process detailed in Section (5.5.2).
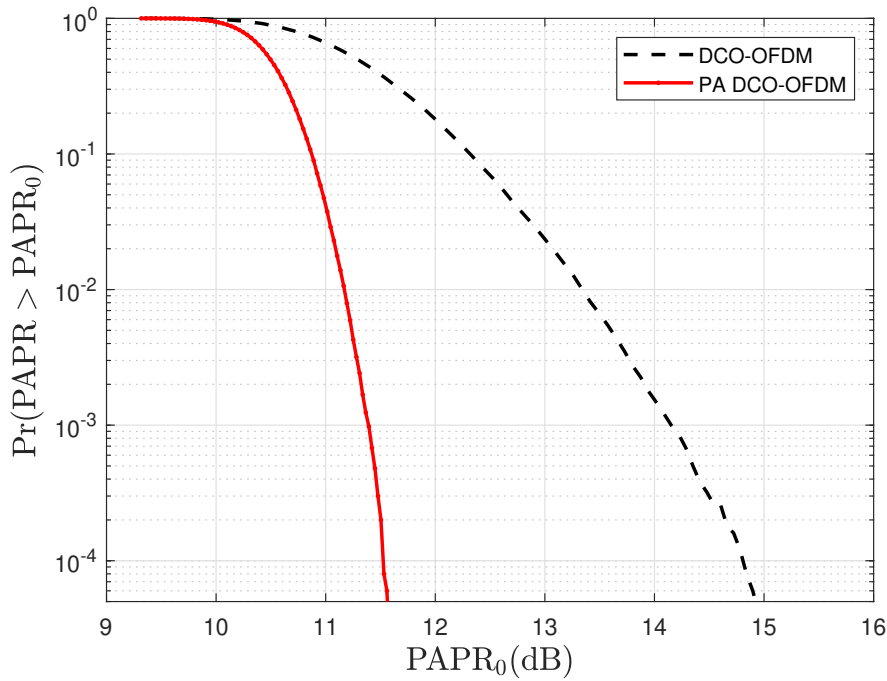
Figure 6.8: *PAPR CCDF plot for PA DCO-OFDM and DCO-OFDM using N_{subs} = 127 active subcarriers, 16-QAM, up-sampling factor = 4, U = 5 data frames per block and PAPR reduction at R = 10 iterations.*

The experimental demonstration of the single blue LED performance for the PAPR reduced PA DCO-OFDM system is illustrated in Fig. 6.9. The BER performance of PA DCO-OFDM and conventional DCO-OFDM at varied transmission rates between (40 - 1000) MSa/s and the optimisation process detailed in Section (5.5). The PA scheme improves the system BER performance without data rate performance degradation. This is due to the PAPR reduction which minimises the clipping noise and distortion level in the system. Consequently, the system SNR is improved and hence, the BER performance is enhanced. At higher transmission rates, far beyond what the available link bandwidth can support, severe distortion in the system causes error in the PA pilot sequence estimation. This is shown to result in the BER of PA system

approaching that of the conventional system with no PAPR reduction. The results demonstrate that the PA PAPR reduction approach can be used to improve the system performance while retaining the high transmission rate capability of the DCO-OFDM system. The system's BER enhancement can be employed for longer distance and/or higher data rate transmissions while keeping the BER below a predefined FEC target.
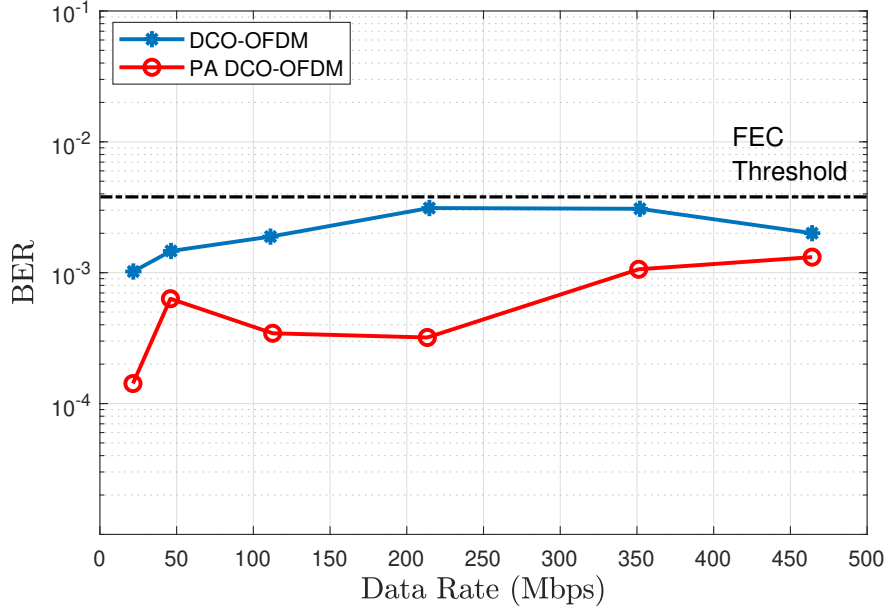
Figure 6.9: *Experimental BER and data rate of PA DCO-FDM and DCO-OFDM using a blue LED.*

6.4.2 WDM Based High-speed VLC System

The WDM system's data transmission and results discussions are presented in this section. The experimental data transmission in this work is a WDM based VLC system using DCO-OFDM and PAM-DMT with PA PAPR reduction technique. The considered WDM system uses three single colour LEDs in the visible light spectrum. The simultaneous data transmission and reception over the three communication channels includes crosstalk between all channels which makes the systems very close to practical applications. Moreover, the modulation bandwidth of each wavelength in the WDM systems is utilised with adaptive bit and power loading for spectral efficiency maximisation. In addition, both systems PAPR is reduced per wavelength by 10 iterations PA to minimise their nonlinearity effect and clipping distortion. The optimised driving bias current (I_{DC}) and peak-to-peak voltage (V_{pp}) of each LED are used for the data

transmission. The I_{DC} of LEDs determine the output optical power and the achievable data rates of the WDM systems.

6.4.2.1 DCO-OFDM Based WDM VLC

(a) *Red LED*

(b) *Green LED*
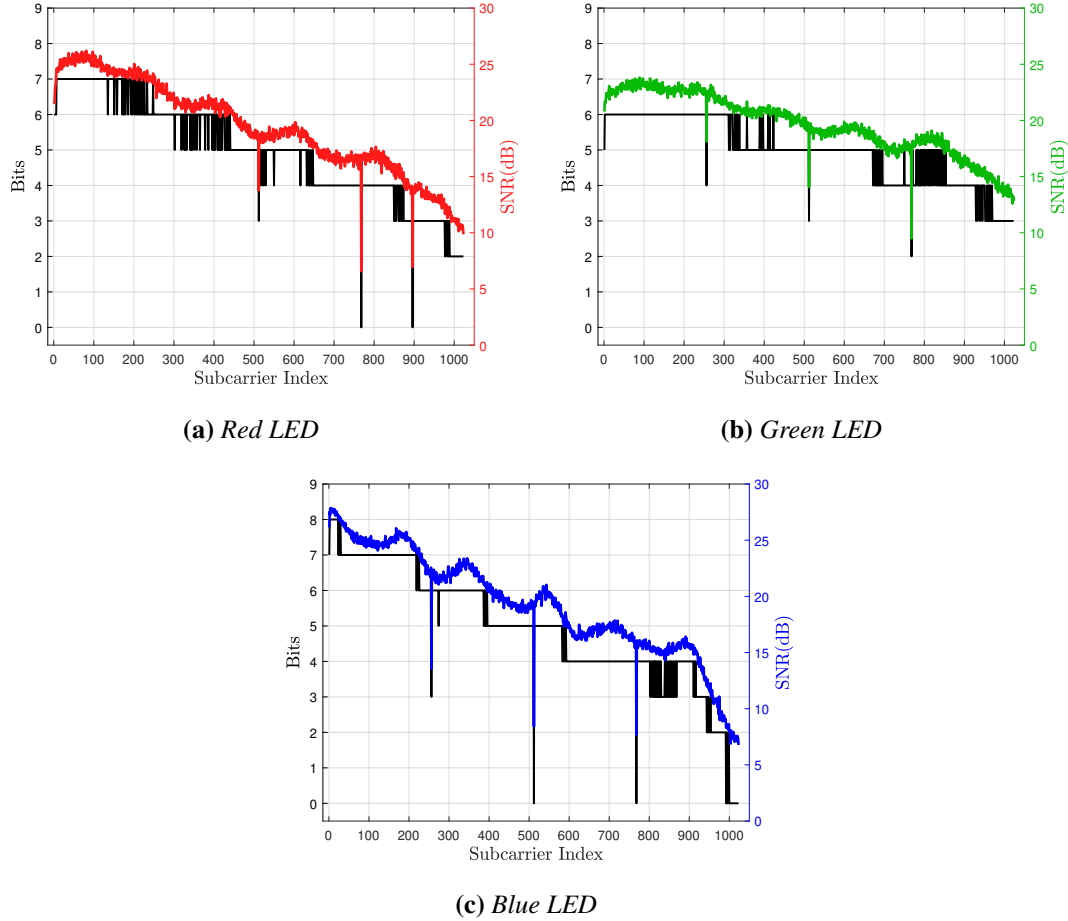
(c) *Blue LED*

Figure 6.10: *DCO-OFDM SNR and bits loaded per subcarrier for each LED.*

The available measured SNR_k determines the QAM modulation format and corresponding power to be loaded adaptively at the subcarrier k for red, green and blue LEDs as shown in Fig. 6.10. The achieved data rate of the PAPR reduced PA DCO-OFDM per wavelength is compared to that of conventional DCO-OFDM without PAPR reduction. Both systems are using the same parameters, experimental equipment, setup and bit and power loading. The achieved data rates and BER results of PA DCO-OFDM compared with DCO-OFDM per LED spectrum are tabulated in Table. 6.1. The aggregate data rate for the PA DCO-OFDM is 7.41 Gb/s for the WDM system, whereas, the conventional DCO-OFDM WDM system achieved 6.92 Gb/s.

This shows that, an increment of more than 8% in data rate without BER degradation when the high PAPR values are reduced by PA DCO-OFDM.

Achieved Data Rate in Gbps and BER				
Scheme	Metric	Red	Green	Blue
DCO-OFDM	Rb	2.37	2.36	2.19
	BER	0.0025	0.0018	0.0014
PA DCO-OFDM	Rb	2.45	2.47	2.49
	BER	0.0024	0.0015	0.0012

Table 6.1: *PA DCO-OFDM and DCO-OFDM performance comparison at optimum values.*

6.4.2.2 PAM-DMT Based WDM VLC

The available measured SNR_k of PAM-DMT determines the PAM modulation size and corresponding power that to be loaded adaptively at the subcarrier k for red, green and blue LEDs as shown in Fig. 6.11. The PAPR reduced PA PAM-DMT data rate per wavelength is compared to that of conventional PAM-DMT without PAPR reduction. Note that both systems are using the same experimental setup and bit and power loading. The PA PAM-DMT data rate and BER results of each LEDs are tabulated in Table. 6.2. The aggregate data rate for the PA PAM-DMT is 3.4885 Gb/s on the WDM system, where, the conventional PAM-DMT based WDM system achieved 3.2339 Gb/s. This shows that, an increment of more than 8% in data rate without BER degradation when the high PAPR values are reduced by PA PAM-DMT.

Achieved Data Rate in Gbps and BER				
Scheme	Metric	Red	Green	Blue
PAM-DMT	Rb	1.0774	1.0917	1.0648
	BER	0.0014	0.0010	0.0002
PA PAM-DMT	Rb	1.1689	1.1734	1.1462
	BER	0.0011	0.0008	0.0001

Table 6.2: *PA PAM-DMT and PAM-DMT performance comparison at optimum values.*

(a) *Red LED*

(b) *Green LED*

(c) *Blue LED*
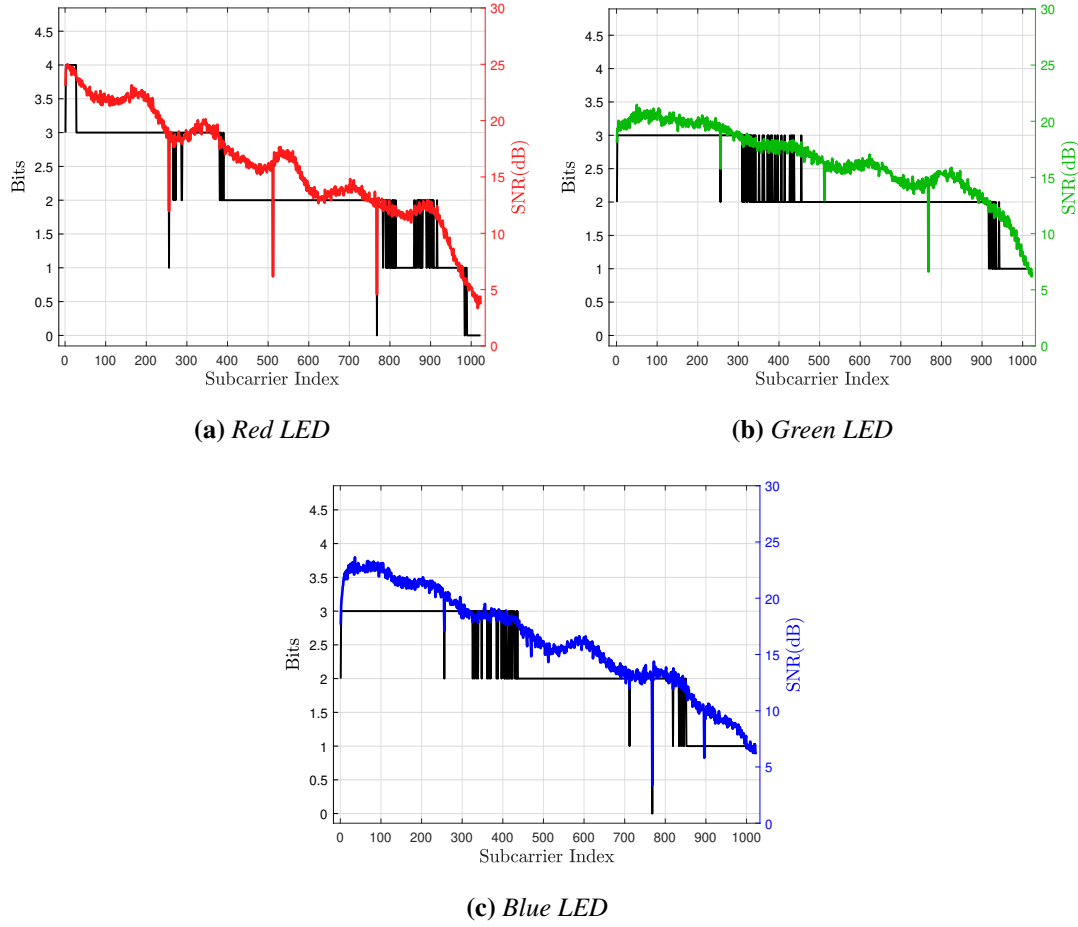
Figure 6.11: *PAM-DMT SNR and bits loaded per subcarrier for each LED.*

6.5   Summary

VLC can achieve high data rate transmission with multicarrier modulation techniques. The common variants are DCO-OFDM and PAM-DMT which offers a spectral and power efficient modulation solutions for VLC respectively. However, similar to other multicarrier modulation schemes, these modulation techniques suffer from high PAPR values. In this chapter, the efficacy of pilot-assisted PA PAPR reduction system in DCO-OFDM and PAM-DMT based VLC is demonstrated experimentally. Single LED and WDM are applied using single and three off-the-shelf LEDs. PA DCO-OFDM and PA PAM-DMT are compared to the conventional DCO-OFDM and PAM-DMT respectively, based on achievable data rate and BER. The available modulation bandwidth of each LED is utilised by adaptive bit and power loading in both systems and their counterparts. The proposed systems reduce the high PAPR values, hence,

reduce the clipping noise and minimise the nonlinearity effect of each wavelength. Thus, the PA systems have achieved more than 8% data rate higher than that of their counterparts with no PAPR reduction. This data rate increment is achieved without BER performance degradation.

The DCO-OFDM with PAPR reduction in PA DCO-OFDM is demonstrated experimentally using a low-cost available blue LED. The BER performance of PA DCO-OFDM is optimised and evaluated and compared to that of conventional DCO-OFDM without PAPR reduction. The optimisation values, parameters and setup are performed for the conventional DCO-OFDM and then applied directly on PA DCO-OFDM for comparison. The PA DCO-OFDM performs better than conventional DCO-OFDM in terms of BER at the same data rate level.

In the WDM system, the DCO-OFDM and PAM-DMT with PAPR reduction are demonstrated experimentally using three different wavelengths using low-cost available LEDs. The system parameters such as the driving bias current points, I_{DC}, and peak-to-peak voltage, V_{pp}, of the LEDs are optimised. In addition, each LEDs' available modulation bandwidth is fully utilised with adaptive bit and power loading. The PAPR of DCO-OFDM and PAM-DMT are reduced by $R = 10$ iterations PA scheme. Therefore, the nonlinearity effect and the clipping distortion of the system caused by the limited dynamic range of the LEDs and high PAPR of the modulation scheme are reduced. As a result, the PA DCO-OFDM and PA PAM-DMT systems result in data rate increment by more than 8% when compared to that of conventional DCO-OFDM and PAM-DMT without PAPR reduction. This summaries that, PA DCO-OFDM increases the system data rate by more than 500 Mb/s, and the PA PAM-DMT system results in more than 250 Mb/s data rate increment in comparison with the conventional counterpart systems. PA DCO-OFDM and PA PAM-DMT increase the system data rate by reducing the clipping noise and maximising the system SNR without BER degradation. The SNR and BER gain of PA DCO-OFDM and PA PAM-DMT systems can be employed for longer distance and/or higher data rate transmissions while keeping the BER below a predefined FEC target. In addition, the PAPR reduction of the system allows for higher input power levels and minimises the nonlinearity effects caused by the LEDs' upper and lower clipping levels. The PA scheme has the potentials to reduce the transmitted average optical power which results in increasing the reliability of the LEDs and hence, the lifetime of the used LEDs. This can be summarised that, the PA technique performs similarly in Gaussian and truncated Gaussian MCM systems by reducing their high PAPR peaks which improves their performance in based VLC systems.

Chapter 7
Conclusion and Future Work

7.1 Conclusions

VLC has the potential to provide high speed transmission for indoor and short-range connectivity links. VLC is a promising technology that can be considered an alternative to the RF-based communication to meet the exponential growth and popularity of smart devices and data-intensive services and applications. The use of low-cost commercially available front-end devices, such as LEDs and PDs further highlights the attraction of VLC technology. However, the limited dynamic ranges of the front-end devices and optical channel impairments limit full exploitation of VLC available modulation bandwidth. To fully benefit from the inherent resources and mitigate these limitations, multicarrier modulation (MCM) techniques such as optical orthogonal frequency division multiplexing (O-OFDM) are adopted. However, these techniques are affected by high peak-to-average power ratio (PAPR) which imposes constraints on the limited dynamic range of the front-end devices and the average radiated optical power. Therefore, the PAPR of the investigated MCM techniques was reduced to eliminate the high PAPR challenge. The main focus throughout this thesis was to reduce the high PAPR of MCM modulation techniques based VLC by implementing PA technique and its performance was investigated through analytical, simulation, and experimentally. An overview of the motivation behind VLC, advancements of its technologies, applications, challenges and solutions for those challenges were introduced in chapter 1 along with the thesis main contributions and the thesis outline. Chapter 2 provided background information of VLC principles, related technologies, challenges and proposed solutions in the literature. Chapter 3 presented overview of the PAPR challenge in MCM modulation techniques based VLC system and the existing proposed PAPR reduction techniques in the literature. In addition, detail description of PA technique is presented including its implementation and performance.

In chapter 4, the high PAPR of PAM-DMT signal $x[n]$ is studied and reduced using PA technique results in PA PAM-DMT with PAPR reduction. The high PAPR peaks of were reduced by $R = 10$ iterations pilot sequences and a gain of 2.75 dB was achieved. This PAPR reduction gain of PA PAM-DMT results in higher SNR of the system, hence, BER performance

improvement in comparison with conventional PAM-DMT. This was proven in an experimental proof-of-concept study for PA PAM-DMT system and compared with PAM-DMT system using a single blue LED over 1 m VLC link. The BER performance of the PA PAM-DMT system was improved without data rate degradation when compared to that of PAM-DMT without PAPR reduction. The achieved BER and SNR enhancement due to the implementation of PA technique can be traded for longer range and/or higher data rate transmission. Furthermore, the PA technique has the potential to reduce the transmitted average optical power which can increase the reliability and lifetime of the LED.

In chapter 5, the nonlinearity of the front-end devices and the limited modulation bandwidth of the light source practically were addressed for a single LED and WDM based VLC system. DCO-OFDM and PAM-DMT were implemented with PA technique as a PAPR reduction solution. Firstly, the efficacy of PA in DCO-OFDM based VLC is demonstrated experimentally using a single blue LED for data transmission over 1 m link. The system parameters were optimised and available modulation bandwidth of the light source was utilised by adaptive bit and power loading. The performance of PA DCO-OFDM and the conventional DCO-OFDM were compared based on the achievable data rate and BER. The proposed system reduces the high PAPR values, hence, reduces the clipping noise and minimises the nonlinearity effect of the front-end devices. Thus, the proposed system has achieved more than 8% data rate higher than that of the conventional DCO-OFDM without PAPR reduction. This data rate increment is achieved without BER performance degradation.

Secondly, DCO-OFDM and PAM-DMT systems with PAPR reduction were demonstrated experimentally for WDM system using three different LEDs. The systems parameters such as the driving bias current points, I_{DC}, and peak-to-peak voltage, V_{pp}, of the LEDs were optimised. In addition, each LEDs' available modulation bandwidth is fully utilised with adaptive bit and power loading. Additionally, the PAPR of DCO-OFDM and PAM-DMT were reduced by $R = 10$ iterations PA technique. Therefore, the nonlinearity effect and the clipping distortion of the system caused by the limited dynamic range of the LEDs and high PAPR of the modulation schemes were reduced. As a result, the PA DCO-OFDM and PA PAM-DMT systems result in data rate increment by more than 8% when compared to that of conventional DCO-OFDM and PAM-DMT without PAPR reduction. This summaries that, PA DCO-OFDM increases the system data rate by more than 500 Mb/s, and the PA PAM-DMT system results in more than 250 Mb/s data rate increment in comparison with the conventional counterpart sys-

tems. PA DCO-OFDM and PA PAM-DMT increase the system data rate by reducing the clipping noise and maximising the system SNR without BER degradation. The SNR and BER gain of PA DCO-OFDM and PA PAM-DMT systems can be employed for longer distance and/or higher data rate transmissions while keeping the BER below a predefined FEC target. In addition, the PAPR reduction of the system allows for higher input power levels and minimises the nonlinearity effects caused by the LEDs' upper and lower clipping levels. The PA techniques has the potentials to reduce the transmitted average optical power which results in increasing the reliability of the LEDs and hence, the lifetime of the used LEDs.

Chapter 6 presented analytical investigation of clipping noise that leads to signal distortion in DCO-OFDM based VLC system due to front-end devices limitations. DCO-OFDM modulation technique was considered for this study with double-sided clipping of its time domain signal. To minimise the clipping noise, high PAPR of the system was reduced by the PA technique. The investigation included the derivation of the attenuation factor and noise variance of the clipping noise of a received waveform in closed-form. Then the SNR of the system was calculated based on the derived attenuation factor and noise variance. The analytical BER performance of the clipped PA DCO-OFDM was studies at different clipping levels then verified through simulation at those clipping levels. The analytical and simulation BER performance were compared to that of the conventional system without PAPR reduction at similar clipping levels. The PA proposed system shows better BER performance at all clipping levels. The high PAPR values reduction of the transmitted signal in PA DCO-OFDM reduces the clipping noise hence, enhances the SNR of the system which results in better BER performance. PAPR reduction has the potential to reduce the transmitted average optical power by reducing the required bias power P_{bias} and minimising the signal distortion. This in turns can increase the reliability of the LED and hence, its lifetime span. The BER gain can be used to increase the transmitted optical power for longer transmission distance and/or higher achievable data rate.

7.2 Limitations and Future Work

The experimental studies presented in this work are carried out under an ideal synchronisation process between the system front-end and this cannot be possible in practical scenarios which results in channel estimation error. In addition, training pilots are included in the data transmission to simplify the channel estimation at the receiver end which results in an overhead frames which limits the system throughput. On the other hand, the system components restricts the

experimental studies due to their physical properties. For instant, the distance of the optical link of each experimental study is limited by the link budget whcih is determined by the light source, optical components and photodetector. Higher PAPR reduction gain of PA is limited by the computational complexity of searching for the optimal phase to reduce the high PAPR of each group of symbols of the O-OFDM frames.

For future work, the phase of data carrying symbols in this work was rotated by a randomly generated pilot sequence phase, $\theta_{\mathrm{p}}[m]$, that is set to 0 or π values only. However, the pilot phase, $\theta_{\mathrm{p}}[m]$, could take any value between 0 and 2π. Therefore, another extension of this research could be investigating the expand of the pilot phase, $\theta_{\mathrm{p}}[m]$, to more values between 0 or 2π, to increase the PAPR reduction gain. This study could include the PAPR reduction gain, BER performance, complexity of searching the optimal phase sequence at the transmitter and recovering the phase at the receiver side. This could be studied through simulation and extended to experimental study. Additionally, the effect of any higher PAPR reduction gain achieved on the average transmitted optical power and the required DC bias to fit the transmitted signal into the linear dynamic range of the frond-end devices.

Real-time implementation of PAPR reduction through PA technique for a VLC system to convey information signal on the radiated optical intensity. This implementation could be using a field programmable gate arrays (FPGA) device to validate the performance of PA. Additionally, numerical and experimental adaptation of PA technique for multiple-input and multiple-output (MIMO) based VLC system.

References

[1] T. Barnett, S. Jain, U. Andra, and T. Khurana, "Cisco visual networking index (vni) complete forecast update, 2017–2022," *Americas/EMEAR Cisco Knowledge Network (CKN) Presentation*, pp. 1–30, 2018.

[2] Cisco, "Cisco Annual Internet Report (2018–2023) White Paper," 2020. `https://www.cisco.com/c/en/us/solutions/collateral/executive-perspectives/annual-internet-report/white-paper-c11-741490.html`, Last accessed on 2022-11-18.

[3] H. Haas, L. Yin, Y. Wang, and C. Chen, "What is LiFi?," *Journal of Lightwave Technology*, vol. 34, no. 6, pp. 1533–1544, 2016.

[4] M. S. Islim, D. Tsonev, and H. Haas, "On the superposition modulation for OFDM-based optical wireless communication," in *2015 IEEE global conference on signal and information processing (GlobalSIP)*, pp. 1022–1026, IEEE, 2015.

[5] M. Figueiredo, L. N. Alves, and C. Ribeiro, "Lighting the Wireless World: The Promise and Challenges of Visible Light Communication," *IEEE Consumer Electronics Magazine*, vol. 6, no. 4, pp. 28–37, 2017.

[6] S.-H. Yu, O. Shih, H.-M. Tsai, N. Wisitpongphan, and R. D. Roberts, "Smart automotive lighting for vehicle safety," *IEEE Communications Magazine*, vol. 51, no. 12, pp. 50–59, 2013.

[7] M. S. Islim and H. Haas, "Modulation Techniques for Li-Fi," *ZTE communications*, vol. 14, no. 2, pp. 29–40, 2019.

[8] C. T. Geldard, E. Guler, A. Hamilton, and W. O. Popoola, "An Empirical Comparison of Modulation Schemes in Turbulent Underwater Optical Wireless Communications," *Journal of Lightwave Technology*, vol. 40, no. 7, pp. 2000–2007, 2022.

[9] G. C. Mandal, R. Mukherjee, B. Das, and A. S. Patra, "A full-duplex WDM hybrid fiber-wired/fiber-wireless/fiber-VLC/fiber-IVLC transmission system based on a self-injection locked quantum dash laser and a RSOA," *Optics Communications*, vol. 427, pp. 202–208, 2018.

[10] IEEE, "IEEE Standard for Local and metropolitan area networks–Part 15.7: Short-Range Optical Wireless Communications," *IEEE Std 802.15.7-2018 (Revision of IEEE Std 802.15.7-2011)*, pp. 1–407, 2019.

[11] L. U. Khan, "Visible light communication: Applications, architecture, standardization and research challenges," *Digital Communications and Networks*, vol. 3, no. 2, pp. 78–88, 2017.

[12] D. Karunatilaka, F. Zafar, V. Kalavally, and R. Parthiban, "LED Based Indoor Visible Light Communications: State of the Art," *IEEE Communications Surveys Tutorials*, vol. 17, pp. 1649–1678, thirdquarter 2015.

[13] M. A. Arfaoui, M. D. Soltani, I. Tavakkolnia, A. Ghrayeb, C. M. Assi, M. Safari, and H. Haas, "Measurements-Based Channel Models for Indoor LiFi Systems," *IEEE Transactions on Wireless Communications*, vol. 20, no. 2, pp. 827–842, 2021.

[14] A. A. Purwita, M. D. Soltani, M. Safari, and H. Haas, "Terminal Orientation in OFDM-Based LiFi Systems," *IEEE Transactions on Wireless Communications*, vol. 18, no. 8, pp. 4003–4016, 2019.

[15] V. H. F. A. Khattat, S. B. A. Anas, and A. Saif, "An Efficient 3D Indoor Positioning System Based on Visible Light Communication," *arXiv preprint arXiv:2209.07158*, 2022.

[16] A. M. Abdalmajeed, M. Mahmoud, A. E.-R. A. El-Fikky, H. A. Fayed, and M. H. Aly, "Improved indoor visible light positioning system using machine learning," *Optical and Quantum Electronics*, vol. 55, no. 3, p. 209, 2023.

[17] C. Cai, M. Fu, X. Meng, C. Jia, and M. Pei, "Indoor high-precision visible light positioning system using Jaya algorithm," *Mathematical Biosciences and Engineering*, vol. 20, no. 6, pp. 10358–10375, 2023.

[18] B. Béchadergue, L. Chassagne, and H. Guan, "Simultaneous Visible Light Communication and Distance Measurement Based on the Automotive Lighting," *IEEE Transactions on Intelligent Vehicles*, vol. 4, no. 4, pp. 532–547, 2019.

[19] E. Zadobrischi, "The Concept regarding Vehicular Communications Based on Visible Light Communication and the IoT," *Electronics*, vol. 12, no. 6, p. 1359, 2023.

[20] M. S. Amjad, C. Tebruegge, A. Memedi, S. Kruse, C. Kress, J. C. Scheytt, and F. Dressler, "Towards an IEEE 802.11 Compliant System for Outdoor Vehicular Visible Light Communications," *IEEE Transactions on Vehicular Technology*, vol. 70, no. 6, pp. 5749–5761, 2021.

[21] C. J. Rapson, B.-C. Seet, P. H. J. Chong, and R. Klette, "Safety Assessment of Radio Frequency and Visible Light Communication for Vehicular Networks," *IEEE Wireless Communications*, vol. 27, no. 1, pp. 186–192, 2020.

[22] H. Zhou, M. Zhang, X. Wang, and X. Ren, "Design and implementation of more than 50m real-time underwater wireless optical communication system," *Journal of Lightwave Technology*, vol. 40, no. 12, pp. 3654–3668, 2022.

[23] Z. Geng, F. N. Khan, X. Guan, and Y. Dong, "Advances in Visible Light Communication Technologies and Applications," *Photonics*, vol. 9, p. 893, Nov 2022.

[24] D. J. F. Barros, S. K. Wilson, and J. M. Kahn, "Comparison of Orthogonal Frequency-Division Multiplexing and Pulse-Amplitude Modulation in Indoor Optical Wireless Links," *IEEE Transactions on Communications*, vol. 60, no. 1, pp. 153–163, 2012.

[25] J. Carruthers and J. Kahn, "Multiple-subcarrier modulation for nondirected wireless infrared communication," *IEEE Journal on Selected Areas in Communications*, vol. 14, no. 3, pp. 538–546, 1996.

[26] W. O. Popoola, Z. Ghassemlooy, and B. G. Stewart, "Pilot-Assisted PAPR Reduction Technique for Optical OFDM Communication Systems," *Journal of Lightwave Technology*, vol. 32, pp. 1374–1382, April 2014.

[27] H. Alrakah, S. Sinanovic, and W. O. Popoola, "Pilot-Assisted PAPR Reduction in PAM-DMT based Visible Light Communication Systems," in *2021 IEEE Latin-American Conference on Communications (LATINCOM)*, pp. 1–6, 2021.

[28] T. Z. Gutema and W. O. Popoola, "Single LED Gbps Visible Light Communication with Probabilistic Shaping," in *2021 IEEE Global Communications Conference (GLOBECOM)*, pp. 1–6, 2021.

[29] J. Armstrong, "OFDM for Optical Communications," *Journal of Lightwave Technology*, vol. 27, pp. 189–204, Feb 2009.

[30] S. K. Wilson and J. Armstrong, "Digital Modulation Techniques for Optical Asymmetrically-Clipped OFDM," in *2008 IEEE Wireless Communications and Networking Conference*, pp. 538–542, 2008.

[31] D. Tsonev, S. Sinanovic, and H. Haas, "Novel Unipolar Orthogonal Frequency Division Multiplexing (U-OFDM) for Optical Wireless," in *2012 IEEE 75th Vehicular Technology Conference (VTC Spring)*, pp. 1–5, 2012.

[32] N. Fernando, Y. Hong, and E. Viterbo, "Flip-OFDM for Optical Wireless Communications," in *2011 IEEE Information Theory Workshop*, pp. 5–9, 2011.

[33] S. C. J. Lee, S. Randel, F. Breyer, and A. M. J. Koonen, "PAM-DMT for Intensity-Modulated and Direct-Detection Optical Communication Systems," *IEEE Photonics Technology Letters*, vol. 21, pp. 1749–1751, Dec 2009.

[34] Seung Hee Han and Jae Hong Lee, "An overview of peak-to-average power ratio reduction techniques for multicarrier transmission," *IEEE Wireless Communications*, vol. 12, pp. 56–65, April 2005.

[35] W. O. Popoola, Z. Ghassemlooy, and B. G. Stewart, "Optimising OFDM based visible light communication for high throughput and reduced PAPR," in *2015 IEEE International Conference on Communication Workshop (ICCW)*, pp. 1322–1326, IEEE, 2015.

[36] S. Dimitrov, S. Sinanovic, and H. Haas, "Clipping Noise in OFDM-Based Optical Wireless Communication Systems," *IEEE Transactions on Communications*, vol. 60, pp. 1072–1081, April 2012.

[37] Y. Rahmatallah and S. Mohan, "Peak-To-Average Power Ratio Reduction in OFDM Systems: A Survey And Taxonomy," *IEEE Communications Surveys and Tutorials*, vol. 15, no. 4, pp. 1567–1592, 2013.

[38] K. Panta and J. Armstrong, "Effects of clipping on the error performance of OFDM in frequency selective fading channels," *IEEE Transactions on Wireless Communications*, vol. 3, no. 2, pp. 668–671, 2004.

[39] L. Cimini and N. Sollenberger, "Peak-to-average power ratio reduction of an OFDM signal using partial transmit sequences," in *1999 IEEE International Conference on Communications (Cat. No. 99CH36311)*, vol. 1, pp. 511–515 vol.1, 1999.

[40] H. Ochiai and H. Imai, "On clipping for peak power reduction of OFDM signals," in *Globecom '00 - IEEE. Global Telecommunications Conference. Conference Record (Cat. No.00CH37137)*, vol. 2, pp. 731–735 vol.2, 2000.

[41] J. Armstrong, "Peak-to-average power reduction for OFDM by repeated clipping and frequency domain filtering," *Electronics letters*, vol. 38, no. 5, p. 1, 2002.

[42] M. Ojima and T. Hattori, "PAPR Reduction Method Using Clipping and Peak-Windowing in CI/OFDM System," in *2007 IEEE 66th Vehicular Technology Conference*, pp. 1356–1360, 2007.

[43] X. Huang, J. Lu, J. Chuang, and J. Zheng, "Companding transform for the reduction of peak-to-average power ratio of OFDM signals," in *IEEE VTS 53rd Vehicular Technology Conference, Spring 2001. Proceedings (Cat. No.01CH37202)*, vol. 2, pp. 835–839 vol.2, 2001.

[44] P. O. Börjesson, H. G. Feichtinger, N. Grip, M. Isaksson, N. Kaiblinger, P. Ödling, and L.-E. Persson, "A low-complexity PAR-reduction method for DMT-VDSL," in *International Symposium on Digital Signal Processing for Communication Systems: 17/02/1999*, pp. 164–169, 1999.

[45] H.-B. Jeon, J.-S. No, and D.-J. Shin, "A New PAPR Reduction Scheme Using Efficient Peak Cancellation for OFDM Systems," *IEEE Transactions on Broadcasting*, vol. 58, no. 4, pp. 619–628, 2012.

[46] R. W. Bauml, R. F. Fischer, and J. B. Huber, "Reducing the peak-to-average power ratio of multicarrier modulation by selected mapping," *Electronics letters*, vol. 32, no. 22, pp. 2056–2057, 1996.

[47] K. Mhatre and U. P. Khot, "Efficient Selective Mapping PAPR Reduction Technique," *Procedia Computer Science*, vol. 45, pp. 620–627, 2015. International Conference on Advanced Computing Technologies and Applications (ICACTA).

[48] K. P. Mhatre and U. P. Khot, "The combined scheme of selective mapping and clipping for PAPR reduction of OFDM," in *2016 3rd International Conference on Computing for Sustainable Global Development (INDIACom)*, pp. 1448–1452, 2016.

[49] H. Breiling, S. Muller-Weinfurtner, and J. Huber, "SLM peak-power reduction without explicit side information," *IEEE Communications Letters*, vol. 5, no. 6, pp. 239–241, 2001.

[50] S. H. Müller and J. B. Huber, "OFDM with reduced peak-to-average power ratio by optimum combination of partial transmit sequences," *IEEE Electronic Letters*, vol. 33, no. 5, pp. 368–369, 1997.

[51] S. Muller and J. Huber, "A novel peak power reduction scheme for OFDM," in *Proceedings of 8th International Symposium on Personal, Indoor and Mobile Radio Communications - PIMRC '97*, vol. 3, pp. 1090–1094 vol.3, 1997.

[52] W. S. Ho, A. Madhukumar, and F. Chin, "Peak-to-average power reduction using partial transmit sequences: a suboptimal approach based on dual layered phase sequencing," *IEEE Transactions on Broadcasting*, vol. 49, no. 2, pp. 225–231, 2003.

[53] A. D. Jayalath and C. Tellambura, "Adaptive PTS approach for reduction of peak-to-average power ratio of OFDM signal," *Electronics Letters*, vol. 36, no. 14, pp. 1226–1228, 2000.

[54] T. Wattanasuwakull and W. Benjapolakul, "PAPR Reduction for OFDM Transmission by using a method of Tone Reservation and Tone Injection," in *2005 5th International Conference on Information Communications and Signal Processing*, pp. 273–277, 2005.

[55] S. Yoo, S. Yoon, S. Y. Kim, and I. Song, "A novel PAPR reduction scheme for OFDM systems: selective mapping of partial tones (SMOPT)," *IEEE Transactions on Consumer Electronics*, vol. 52, no. 1, pp. 40–43, 2006.

[56] D. Jones, "Peak power reduction in OFDM and DMT via active channel modification," in *Conference Record of the Thirty-Third Asilomar Conference on Signals, Systems, and Computers (Cat. No.CH37020)*, vol. 2, pp. 1076–1079 vol.2, 1999.

[57] B. Krongold and D. Jones, "PAR reduction in OFDM via active constellation extension," in *2003 IEEE International Conference on Acoustics, Speech, and Signal Processing, 2003. Proceedings. (ICASSP '03).*, vol. 4, pp. IV–525, 2003.

[58] A. Aggarwal and T. Meng, "Minimizing the Peak-to-Average Power Ratio of OFDM Signals Using Convex Optimization," *IEEE Transactions on Signal Processing*, vol. 54, no. 8, pp. 3099–3110, 2006.

[59] A. E. Jones, T. A. Wilkinson, and S. Barton, "Block coding scheme for reduction of peak to mean envelope power ratio of multicarrier transmission schemes," *Electronics letters*, vol. 30, no. 25, pp. 2098–2099, 1994.

[60] D. Wulich, "Reduction of peak to mean ratio of multicarrier modulation using cyclic coding," *Electronics Letters*, vol. 32, pp. 432–433, 1996.

[61] Y. Zhang, A. Yongacoglu, J.-Y. Chouinard, and L. Zhang, "OFDM peak power reduction by sub-block-coding and its extended versions," in *1999 IEEE 49th Vehicular Technology Conference (VTC)*, vol. 1, pp. 695–699 vol.1, 1999.

[62] M.-C. Lin, K.-C. Chen, and S.-L. Li, "Turbo coded OFDM system with peak power reduction," in *2003 IEEE 58th Vehicular Technology Conference. VTC 2003-Fall (IEEE Cat. No.03CH37484)*, vol. 4, pp. 2282–2286 Vol.4, 2003.

[63] A. Abouda, "PAPR reduction of OFDM signal using turbo coding and selective mapping," in *Proceedings of the 6th Nordic Signal Processing Symposium, 2004. NORSIG 2004.*, pp. 248–251, 2004.

[64] Y.-c. Tsai, S.-k. Deng, K.-c. Chen, and M.-c. Lin, "Turbo Coded OFDM for Reducing PAPR and Error Rates," *IEEE Transactions on Wireless Communications*, vol. 7, no. 1, pp. 84–89, 2008.

[65] K. Miura, "An Introduction to Maximum Likelihood Estimation and Information Geometry," *Interdisciplinary Information Sciences (IIS)*, vol. 17, 11 2011.

[66] S. Selleri, "Claude Chappe and the first telecommunication network (without electricity)," *URSI Radio Science Bulletin*, vol. 2017, no. 360, pp. 96–101, 2017.

[67] A. G. Bell, "The photophone," *Science*, no. 11, pp. 130–134, 1880.

[68] D. Hutt, K. Snell, and P. Belanger, "Alexander Graham Bell's Photophone," *Optics and Photonics News*, vol. 4, no. 6, pp. 20–25, 1993.

[69] F. Gfeller and U. Bapst, "Wireless in-house data communication via diffuse infrared radiation," *Proceedings of the IEEE*, vol. 67, no. 11, pp. 1474–1486, 1979.

[70] M. A. Khalighi and M. Uysal, "Survey on Free Space Optical Communication: A Communication Theory Perspective," *IEEE Communications Surveys and Tutorials*, vol. 16, no. 4, pp. 2231–2258, 2014.

[71] V. W. S. Chan, "Free-Space Optical Communications," *Journal of Lightwave Technology*, vol. 24, no. 12, pp. 4750–4762, 2006.

[72] I. Akasaki, H. Amano, and S. Nakamura, "Blue LEDs–Filling the world with new light," *The Nobel Prize in Physics*, 2014.

[73] Y. Tanaka, T. Komine, S. Haruyama, and M. Nakagawa, "Indoor visible communication utilizing plural white LEDs as lighting," in *12th IEEE International Symposium on Personal, Indoor and Mobile Radio Communications. PIMRC 2001. Proceedings (Cat. No.01TH8598)*, vol. 2, pp. 81–85, 2001.

[74] T. Komine and M. Nakagawa, "Fundamental analysis for visible-light communication system using LED lights," *IEEE Transactions on Consumer Electronics*, vol. 50, no. 1, pp. 100–107, 2004.

[75] H. T. Alrakah, T. Z. Gutema, S. Sinanovic, and W. O. Popoola, "PAPR Reduction in DCO-OFDM Based WDM VLC," *Journal of Lightwave Technology*, vol. 40, no. 19, pp. 6359–6365, 2022.

[76] G. Pang, T. Kwan, C.-H. Chan, and H. Liu, "LED traffic light as a communications device," in *Proceedings 199 IEEE/IEEJ/JSAI International Conference on Intelligent Transportation Systems (Cat. No.99TH8383)*, pp. 788–793, 1999.

[77] Y. Tanaka, S. Haruyama, and M. Nakagawa, "Wireless optical transmissions with white colored LED for wireless home links," in *11th IEEE International Symposium on Personal Indoor and Mobile Radio Communications. PIMRC 2000. Proceedings (Cat. No.00TH8525)*, vol. 2, pp. 1325–1329 vol.2, 2000.

[78] J. Söderberg, "Free space optics in the czech wireless community: Shedding some light on the role of normativity for user-initiated innovations," *Science, Technology, Human Values*, vol. 36, no. 4, pp. 423–450, 2011.

[79] R. Bian, I. Tavakkolnia, and H. Haas, "15.73 Gb/s Visible Light Communication With Off-the-Shelf LEDs," *Journal of Lightwave Technology*, vol. 37, no. 10, pp. 2418–2424, 2019.

[80] H. Haas, J. Elmirghani, and I. White, "Optical wireless communication," *Philosophical Transactions of the Royal Society A*, vol. 378, no. 2169, p. 20200051, 2020.

[81] Z. Ghassemlooy, W. Popoola, and S. Rajbhandari, *Optical Wireless Communications: System and Channel Modelling with Matlab®*. CRC press, 2019.

[82] F. Yam and Z. Hassan, "Innovative advances in LED technology," *Microelectronics Journal*, vol. 36, no. 2, pp. 129–137, 2005.

[83] J. Kahn and J. Barry, "Wireless infrared communications," *Proceedings of the IEEE*, vol. 85, no. 2, pp. 265–298, 1997.

[84] Vishay, "Ultrabright 0402 ChipLED," 2023. `https://www.vishay.com/docs/82554/vlmo1500.pdf`, Last accessed on 2023-04-30.

[85] F. Zafar, M. Bakaul, and R. Parthiban, "Laser-Diode-Based Visible Light Communication: Toward Gigabit Class Communication," *IEEE Communications Magazine*, vol. 55, no. 2, pp. 144–151, 2017.

[86] R. Hui, "Photodetectors," in *Introduction to Fiber-Optic Communications*, pp. 125–154, Academic Press, 2020.

[87] M. P. Sheehan, J. Tachella, and M. E. Davies, "A Sketching Framework for Reduced Data Transfer in Photon Counting Lidar," *IEEE Transactions on Computational Imaging*, vol. 7, pp. 989–1004, 2021.

[88] Y. Li, S. Videv, M. M. Abdallah, K. A. Qaraqe, M. Uysal, and H. Haas, "Single Photon Avalanche Diode (SPAD) VLC System and Application to Downhole Monitoring," *2014 IEEE Global Communications Conference*, pp. 2108–2113, 2014.

[89] T. Z. Gutema, H. Haas, and W. O. Popoola, "Bias point optimisation in LiFi for capacity enhancement," *Journal of Lightwave Technology*, vol. 39, no. 15, pp. 5021–5027, 2021.

[90] J. R. Barry, J. M. Kahn, W. J. Krause, E. A. Lee, and D. G. Messerschmitt, "Simulation of Multipath Impulse Response for Indoor Wireless Optical Channels," *IEEE journal on selected areas in communications*, vol. 11, no. 3, pp. 367–379, 1993.

[91] A. M. Khalid, G. Cossu, R. Corsini, P. Choudhury, and E. Ciaramella, "1-Gb/s Transmission Over a Phosphorescent White LED by Using Rate-Adaptive Discrete Multitone Modulation," *IEEE Photonics Journal*, vol. 4, no. 5, pp. 1465–1473, 2012.

[92] H. L. Minh, D. O'Brien, G. Faulkner, L. Zeng, K. Lee, D. Jung, and Y. Oh, "80 Mbit/s Visible Light Communications using pre-equalized white LED," in *2008 34th European Conference on Optical Communication*, pp. 1–2, 2008.

[93] H. Le Minh, D. O'Brien, G. Faulkner, L. Zeng, K. Lee, D. Jung, and Y. Oh, "High-speed visible light communications using multiple-resonant equalization," *IEEE Photonics Technology Letters*, vol. 20, no. 14, pp. 1243–1245, 2008.

[94] R. Kisacik, M. Y. Yagan, M. Uysal, A. E. Pusane, and A. D. Yalcinkaya, "A New LED Response Model and its Application to Pre-Equalization in VLC Systems," *IEEE Photonics Technology Letters*, vol. 33, no. 17, pp. 955–958, 2021.

[95] L. Zeng, H. L. Minh, D. O'Brien, G. Faulkner, K. Lee, D. Jung, and Y. Oh, "Equalisation for high-speed Visible Light Communications using white-LEDs," in *2008 6th International Symposium on Communication Systems, Networks and Digital Signal Processing*, pp. 170–173, 2008.

[96] W. G. Jeon, K. H. Chang, and Y. S. Cho, "An equalization technique for orthogonal frequency-division multiplexing systems in time-variant multipath channels," *IEEE Transactions on Communications*, vol. 47, no. 1, pp. 27–32, 1999.

[97] Y. Jiang, M. K. Varanasi, and J. Li, "Performance Analysis of ZF and MMSE Equalizers for MIMO Systems: An In-Depth Study of the High SNR Regime," *IEEE Transactions on Information Theory*, vol. 57, no. 4, pp. 2008–2026, 2011.

[98] X. Li, N. Bamiedakis, X. Guo, J. J. D. McKendry, E. Xie, R. Ferreira, E. Gu, M. D. Dawson, R. V. Penty, and I. H. White, "Wireless Visible Light Communications Employing Feed-Forward Pre-Equalization and PAM-4 Modulation," *Journal of Lightwave Technology*, vol. 34, no. 8, pp. 2049–2055, 2016.

[99] S. Dimitrov and H. Haas, *Principles of LED Light Communications: Towards Networked Li-Fi*. Cambridge University Press, 2015.

[100] H. Elgala, R. Mesleh, and H. Haas, "Predistortion in Optical Wireless Transmission Using OFDM," in *2009 Ninth International Conference on Hybrid Intelligent Systems*, vol. 2, pp. 184–189, 2009.

[101] H. Qian, S. J. Yao, S. Z. Cai, and T. Zhou, "Adaptive Postdistortion for Nonlinear LEDs in Visible Light Communications," *IEEE Photonics Journal*, vol. 6, no. 4, pp. 1–8, 2014.

[102] D. Tsonev, S. Sinanovic, and H. Haas, "Complete Modeling of Nonlinear Distortion in OFDM-Based Optical Wireless Communication," *Journal of Lightwave Technology*, vol. 31, pp. 3064–3076, Sep. 2013.

[103] H. G. Myung, J. Lim, and D. J. Goodman, "Single carrier FDMA for uplink wireless transmission," *IEEE vehicular technology magazine*, vol. 1, no. 3, pp. 30–38, 2006.

[104] J. Zhou, Q. Wang, Q. Cheng, M. Guo, Y. Lu, A. Yang, and Y. Qiao, "Low-PAPR Layered/Enhanced ACO-SCFDM for Optical-Wireless Communications," *IEEE Photonics Technology Letters*, vol. 30, no. 2, pp. 165–168, 2018.

[105] J. Zhou and Y. Qiao, "Low-peak-to-average power ratio and low-complexity asymmetrically clipped optical orthogonal frequency-division multiplexing uplink transmission scheme for long-reach passive optical network," *Opt. Lett.*, vol. 40, pp. 4034–4037, Sep 2015.

[106] S. D. Dissanayake and J. Armstrong, "Comparison of ACO-OFDM, DCO-OFDM and ADO-OFDM in IM/DD Systems," *Journal of Lightwave Technology*, vol. 31, pp. 1063–1072, April 2013.

[107] A. Khalid, G. Cossu, R. Corsini, M. Presi, and E. Ciaramella, "Hybrid radio over fiber and visible light (RoF-VLC) communication system," in *European Conference and Exposition on Optical Communications*, pp. We–7, Optica Publishing Group, 2011.

[108] J. Armstrong and A. J. Lowery, "Power efficient optical OFDM," *Electronics Letters*, vol. 42, pp. 370–372, March 2006.

[109] J. Armstrong, B. J. C. Schmidt, D. Kalra, H. A. Suraweera, and A. J. Lowery, "SPC07-4: Performance of Asymmetrically Clipped Optical OFDM in AWGN for an Intensity Modulated Direct Detection System," in *IEEE Globecom 2006*, pp. 1–5, 2006.

[110] S. Randel, F. Breyer, S. C. J. Lee, and J. W. Walewski, "Advanced modulation schemes for short-range optical communications," *IEEE Journal of Selected Topics in Quantum Electronics*, vol. 16, no. 5, pp. 1280–1289, 2010.

[111] J. Lian, M. Noshad, and M. Brandt-Pearce, "Comparison of optical ofdm and m-pam for led-based communication systems," *IEEE Communications Letters*, vol. 23, no. 3, pp. 430–433, 2019.

[112] A. Pradana, N. Ahmadi, T. Adiono, W. A. Cahyadi, and Y.-H. Chung, "Vlc physical layer design based on pulse position modulation (ppm) for stable illumination," in *2015 International Symposium on Intelligent Signal Processing and Communication Systems (ISPACS)*, pp. 368–373, 2015.

[113] H.-J. Jang, J.-H. Choi, Z. Ghassemlooy, and C. G. Lee, "PWM-based PPM format for dimming control in visible light communication system," in *2012 8th International Symposium on Communication Systems, Networks and Digital Signal Processing (CSNDSP)*, pp. 1–5, 2012.

[114] M. Zhang and Z. Zhang, "An Optimum DC-Biasing for DCO-OFDM System," *IEEE Communications Letters*, vol. 18, pp. 1351–1354, Aug 2014.

[115] S. Dimitrov and H. Haas, "Information Rate of OFDM-Based Optical Wireless Communication Systems With Nonlinear Distortion," *Journal of Lightwave Technology*, vol. 31, pp. 918–929, March 2013.

[116] J. Armstrong and B. J. Schmidt, "Comparison of asymmetrically clipped optical OFDM and DC-biased optical OFDM in AWGN," *IEEE Communications Letters*, vol. 12, no. 5, pp. 343–345, 2008.

[117] S. Viola, M. S. Islim, S. Watson, S. Videv, H. Haas, and A. E. Kelly, "15 Gb/s OFDM-based VLC using direct modulation of 450 GaN laser diode," in *Advanced Free-Space Optical Communication Techniques and Applications III* (H. J. White and F. Moll, eds.), vol. 10437, pp. 101 – 107, International Society for Optics and Photonics, SPIE, 2017.

[118] D. Tsonev, M. S. Islim, and H. Haas, *OFDM-Based Visible Light Communications*, pp. 255–298. Cham: Springer International Publishing, 2016.

[119] D. Tsonev and H. Haas, "Avoiding spectral efficiency loss in unipolar ofdm for optical wireless communication," in *2014 IEEE International Conference on Communications (ICC)*, pp. 3336–3341, 2014.

[120] M. S. Islim, D. Tsonev, and H. Haas, "Spectrally enhanced PAM-DMT for IM/DD optical wireless communications," in *2015 IEEE 26th Annual International Symposium on Personal, Indoor, and Mobile Radio Communications (PIMRC)*, pp. 877–882, 2015.

[121] M. S. Islim and H. Haas, "Augmenting the spectral efficiency of enhanced PAM-DMT-based optical wireless communications," *Opt. Express*, vol. 24, pp. 11932–11949, May 2016.

[122] S. D. Dissanayake, K. Panta, and J. Armstrong, "A novel technique to simultaneously transmit ACO-OFDM and DCO-OFDM in IM/DD systems," in *2011 IEEE GLOBE-COM Workshops (GC Wkshps)*, pp. 782–786, 2011.

[123] B. Ranjha and M. Kavehrad, "Hybrid asymmetrically clipped ofdm-based im/dd optical wireless system," *Journal of Optical Communications and Networking*, vol. 6, no. 4, pp. 387–396, 2014.

[124] H. Elgala and T. D. C. Little, "See-ofdm: Spectral and energy efficient ofdm for optical im/dd systems," in *2014 IEEE 25th Annual International Symposium on Personal, Indoor, and Mobile Radio Communication (PIMRC)*, pp. 851–855, 2014.

[125] Q. Wang, C. Qian, X. Guo, Z. Wang, D. G. Cunningham, and I. H. White, "Layered aco-ofdm for intensity-modulated direct-detection optical wireless transmission," *Optics Express*, vol. 23, no. 9, pp. 12382–12393, 2015.

[126] J. A. Rice, *Mathematical Statistics and Data Analysis*. Cengage Learning, 2006.

[127] J. G. Doblado, A. C. O. Oria, V. Baena-Lecuyer, P. Lopez, and D. Perez-Calderon, "Cubic Metric Reduction for DCO-OFDM Visible Light Communication Systems," *Journal of Lightwave Technology*, vol. 33, no. 10, pp. 1971–1978, 2015.

[128] P. Bento, J. Nunes, M. Gomes, R. Dinis, and V. Silva, "Measuring the Magnitude of Envelope Fluctuations: Should We Use the PAPR?," in *2014 IEEE 80th Vehicular Technology Conference (VTC2014-Fall)*, pp. 1–5, 2014.

[129] S. Litsyn, *Peak power control in multicarrier communications*. Cambridge University Press, 2007.

[130] Y. S. Cho, J. Kim, W. Y. Yang, and C. G. Kang, *MIMO-OFDM wireless communications with MATLAB*. John Wiley & Sons, 2010.

[131] W. Shieh and I. B. Djordjevic, *OFDM for Optical Communications*. Academic press, 2010.

[132] J. Zhou, J. He, X. Lu, G. Wang, Y. Bo, G. Liu, Y. Huang, L. Li, H. Wang, W. Mo, *et al.*, "First 100 Gb/s Fine-Granularity Flexible-Rate PON Based on Discrete Multi-Tone and PAPR Optimization," in *Optical Fiber Communication Conference*, pp. Th2A–23, Optica Publishing Group, 2022.

[133] S. Y. Le Goff, B. K. Khoo, C. C. Tsimenidis, and B. S. Sharif, "A novel selected mapping technique for PAPR reduction in OFDM systems," *IEEE Transactions on Communications*, vol. 56, no. 11, pp. 1775–1779, 2008.

[134] Y. A. Jawhar, L. Audah, M. A. Taher, K. N. Ramli, N. S. M. Shah, M. Musa, and M. S. Ahmed, "A Review of Partial Transmit Sequence for PAPR Reduction in the OFDM Systems," *IEEE Access*, vol. 7, pp. 18021–18041, 2019.

[135] F. B. Offiong, S. Sinanović, and W. O. Popoola, "On PAPR Reduction in Pilot-Assisted Optical OFDM Communication Systems," *IEEE Access*, vol. 5, pp. 8916–8929, 2017.

[136] J. Bussgang, "Cross-correlation Functions of Amplitude-distorted Gaussian Signals," *Tech. Rep. 216, Research Lab. Electron*, 1952.

[137] M. S. Islim, R. X. Ferreira, X. He, E. Xie, S. Videv, S. Viola, S. Watson, N. Bamiedakis, R. V. Penty, I. H. White, A. E. Kelly, E. Gu, H. Haas, and M. D. Dawson, "Towards 10 Gb/s orthogonal frequency division multiplexing-based visible light communication using a GaN violet micro-LED," *Photon. Res.*, vol. 5, pp. A35–A43, Apr 2017.

[138] T. Zhang, Y. Zou, J. Sun, and S. Qiao, "Design of PAM-DMT-based hybrid optical OFDM for visible light communications," *IEEE Wireless Communications Letters*, vol. 8, no. 1, pp. 265–268, 2018.

[139] D. Tsonev, S. Videv, and H. Haas, "Unlocking Spectral Efficiency in Intensity Modulation and Direct Detection Systems," *IEEE Journal on Selected Areas in Communications*, vol. 33, no. 9, pp. 1758–1770, 2015.

[140] H. Levin, "A complete and optimal data allocation method for practical discrete multitone systems," in *GLOBECOM'01. IEEE Global Telecommunications Conference (Cat. No.01CH37270)*, vol. 1, pp. 369–374 vol.1, 2001.

[141] R. A. Shafik, M. S. Rahman, and A. R. Islam, "On the Extended Relationships Among EVM, BER and SNR as Performance Metrics," in *2006 International Conference on Electrical and Computer Engineering*, pp. 408–411, 2006.

[142] dialight, "Micro LED, Surface Mount LED Selector Guide," 2022. `https://www.dialight.com/wp-content/uploads/2021/07/DIA_Selector_Guide_SMD_042321.pdf`, Last accessed on 2022-02-25.